

UC Santa Barbara

UC Santa Barbara Electronic Theses and Dissertations

Title

Elucidating the Driving Forces from Tau Molecules to Droplet

Permalink

<https://escholarship.org/uc/item/6w92c3mw>

Author

Lin, Yanxian

Publication Date

2020

Peer reviewed|Thesis/dissertation

UNIVERSITY OF CALIFORNIA

Santa Barbara

Elucidating the Driving Forces from Tau Molecules to Droplet

A dissertation submitted in partial satisfaction of the
requirements for the degree Doctor of Philosophy
in Biochemistry and Molecular Biology

by

Yanxian Lin

Committee in charge:

Professor Songi Han, co-chair

Professor Joan-Emma Shea, co-chair

Professor Kenneth S. Kosik

Professor Omar A. Saleh

September 2020

The dissertation of Yanxian Lin is approved.

Kenneth S. Kosik

Omar A. Saleh

Joan-Emma Shea, Committee Co-chair

Songi Han, Committee Co-chair

August 2020

Elucidating the Driving Forces from Tau Molecules to Droplet

Copyright © 2020

by

Yanxian Lin

Acknowledgements

I would like to thank my PhD advisor Prof. Songi Han, for her solid training on my scientific skills and strong support on my career development. She has been actively involved in the whole life cycle of each of my PhD research projects, including hypothesis, experiment designs, execution, data analysis and conclusion. The sharpness of her eyes and the clarity of her thoughts have required that the phenomena I observed should be well thought-through and deeply understood. The depth of understanding is aimed to a degree that I can visually see the molecules and their interactions, as if they are floating in front of me. Such ability to draw simplified picture from complicated data has become one of the most valuable assets I have gained. During my time as a graduate student, Songi has been strongly supporting my exploration of career and search of role fit beyond academia. Her active referral and recommendation have endorsed my profile and introduced me to meaningful and fruitful internship experiences, where I demonstrated the applications of my scientific skills learned from research to tackling the challenges in the industry.

The research work presented here results from collective efforts. For that I would like to thank the rest of the members in my committee, Prof. Joan-Emma Shea, Prof. Kenneth S. Kosik and Prof. Omar A. Saleh, whom I have had weekly meetings and numerous discussions with during my PhD years. I have to thank researchers who contributed directly or indirectly, including Dr. Yann Fichou, Dr. Neil A. Eschmann, Dr. Xuemei Zhang, Dr. Jennifer Rauch, Dr. James McCarty, Dr. Saeed Najafi, Prof. Dongsoo Hwang, Dr. Andrew Longhini, Dr. Ryan

Barnes, Dr. Thomas Casey, Michael Vigers, Kate Zeng, and many other members as well as alumni from the Han Lab. I also have to thank undergraduate researchers who I have enjoyed working with and have contributed their talents and efforts to the work presented here, including Nicole Y. Hu, Pengyi Yin and Athena Quddus among others. I would also like to thank others in UC Santa Barbara who have been supporting my role as a graduate researcher throughout the years, including my lab rotation leaders Prof. Kevin W. Plaxco, Prof. Sumita Pennathur as well as my department program manager Stella Hahn among others.

Last but not least, I would like to thank my families including Xiuling Chen, Yingjin Lin and Zhiwei Chen among others who have continuously supported my pursue of research overseas. I would like to thank my friends including Dr. He Ma, Dr. Weidong Xu, Dr. Yuanyi Zhang from whom I have learned many from, as well as my supervisors and colleagues during Internships, including Dr. Yi-Qiao Song, Dr. Ray Tang and Dr. Thorsten Maly among others who have shared with me their expertise.

VITA of Yanxian Lin

Education

Ph.D. in Biochemistry and Molecular Biology September 2015 - present

University of California, Santa Barbara, CA

- American Physical Society Shirley Chan Travel Award (2019)

B.S. in Chemical Biology 2011 - 2015

Tsinghua University, Beijing, China

- Academic Excellence Award (2013)
- Tsinghua Xue Tang Talents Fellowship (2013-2015)

Research Experience

Graduate Student Researcher

Prof Songi Han, UC Santa Barbara, CA

April 2016 – present

- Illustrated structure and dynamics of liquid phase separation of Alzheimer-related protein tau, mapped its phase diagram, and unraveled its relationship to tau amyloid aggregation.
- Conceived and executed experiments using magnetic resonance spectroscopies (cwEPR, DEER, ODNP, ESEEM), microscopies (TEM, bright field, Confocal) and biochemical assays (CD, Fluorescence, UV, DLS, ITC).
- Automated data processing, modeling and visualization, implementing statistical analysis, nonlinear regression and optimization, using MATLAB, Python and R.

Prof. Sumita Pennathur, UC Santa Barbara, CA

January - March 2016

- Developed protocol applying electrophoresis, micro/nanofluidics and fluorescent microscopy in studying DNA hybridization.

Prof. Kevin Plaxco, UC Santa Barbara, CA

October - December 2015

- Improved protein purification protocol. Developed R program to enable real-time data processing for an *in vivo* biochemical sensor.

Undergraduate Student Researcher

Prof. Xu Ke, UC Berkeley, CA

July – August 2014

- Demonstrated and developed protocol integrating microfluidic chips with STORM-microscopy for studying immune cell chemotaxis, revealing sub-micron structures of actin and microtubule in chemotactic dendritic cell and macrophage.

Prof. Xinrong Zhang, Tsinghua University, China

August 2013 – July 2014

- Studied selectivity of probe electrospray ionization (probe-ESI) mass spectrometry by functionalizing probe tip to realize solid-phase micro extraction

Prof. Jinming Lin, Tsinghua University, China

February 2013 – July 2013

- Studied the effects of particle pollutant PM2.5 in air on cell viability by achieving direct contact between cultured cells and polluted air on microfluidic chips.

Publications and Patent

1. **Lin, Yanxian***, Yann Fichou*, Andrew P. Longhini, Luana C. Llanes, Yinson Yin, Guillermo C. Bazan, Kenneth S. Kosik, and Songi Han. "Liquid-Liquid Phase Separation of Tau Driven by Hydrophobic Interaction Facilitates Fibrillization of Tau." *BioRxiv*, 2020.
2. **Lin, Yanxian**, Yann Fichou, Jennifer N Rauch, Xuemei Zhang, Kenneth S Kosik, and Songi Han. "Phase diagram of tau-RNA LLPS under live cell coculturing conditions." *Methods in Molecular Biology* 2020, *in press*.
3. **Lin, Yanxian**, Yann Fichou, Zhikai Zeng, Nicole Y Hu, and Songi Han. "Complex Coacervation and Amyloid Aggregation of Tau Are Independent Processes with Overlapping Conditions." *ACS Chem. Neurosci.*, 2020.
4. Park, Sohee, Ryan Barnes, **Yanxian Lin**, Byoung-jin Jeon, Saeed Najafi, Kris T. Delaney, Glenn H. Fredrickson, Joan-Emma Shea, Dong Soo Hwang, and Songi Han. "Dehydration entropy drives liquid-liquid phase separation by molecular crowding." *Communications Chemistry* 2020.
5. **Lin, Yanxian***, James McCarty*, Jennifer N Rauch, Kris T Delaney, Kenneth S Kosik, Glenn H Fredrickson, Joan-Emma Shea, and Songi Han. "Narrow Equilibrium Window for Complex Coacervation of Tau and RNA under Cellular Conditions." *eLife*, 2019 (**Highlighted on eLife Digest**)
6. Tang, Yiqiao, **Yanxian Lin**, Yi-Qiao Song, and Martin Hürlimann. "Elastic Regression-Tree Learning in a Heterogeneous Computing Environment." *IEEE Internet of Things Journal*, 2019.
7. Fichou, Yann*, **Yanxian Lin***, Jennifer N Rauch, Michael Vigers, Zhikai Zeng, Madhur Srivastava, Timothy J Keller, Jack H Freed, Kenneth S Kosik, and Songi Han. "Cofactors Are Essential Constituents of Stable and Seeding-Active Tau Fibrils." *Proceedings of the National Academy of Sciences*, 2018.
8. Zhang, Xuemei, **Yanxian Lin**, Neil A Eschmann, Hongjun Zhou, Jennifer N Rauch, Israel Hernandez, Elmer Guzman, Kenneth S Kosik, and Songi Han. "RNA Stores Tau Reversibly in Complex Coacervates." *PLoS Biology*, 2017. (**Collected as Top 10% Most Cited of the year**)
9. Jho, YongSeok, Hee Young Yoo, **Yanxian Lin**, Songi Han, and Dong Soo Hwang. "Molecular and Structural Basis of Low Interfacial Energy of Complex Coacervates in Water." *Advances in Colloid and Interface Science* 239, 2017.
10. Tang, Yiqiao, Yi-Qiao Song, Martin Hürlimann, **Yanxian Lin**. "Elastic Adaptive Downhole Acquisition System." (PCT/US2019/053552), 2019

Conference Presentations

1. **Lin, Yanxian**, Kate Zeng, Yann Fichou, Yuge Hu, and Songi Han. "Impact of Complex Coacervation on Tau Amyloid Aggregation." In *American Physical Society Meeting Abstracts*, 2019.
2. **Lin, Yanxian**, Yuge Hu, and Songi Han. "Liquid-Liquid Phase Separation by Tau-Polyanion Complex Coacervation and Its Relationship to Amyloid Fibrillization." In *American Physical Society Meeting Abstracts*, 2018.
3. C. McCallum, **Y. Lin**, J. Rutte, I. Chen, S. Pennathur. MicroTAS 2016 Conference. Poster.

Abstract

Elucidating the Driving Forces from Tau Molecules to Droplet

by

Yanxian Lin

Tau protein binds and stabilizes microtubules in the neurons of human brain. Its aggregation into amyloid fibrils is a hallmark of Alzheimer's disease and associated with many other neurodegenerative diseases. Revealing its aggregation mechanism is key to understanding the disease progress and developing therapies. Tau is recently found by us and others to form droplet, a condense, fluidic and dynamic structure resulting from liquid-liquid phase separation of proteins, RNA and other molecules. Droplet has been shown to promote amyloid aggregation of several other neurodegenerative disease-associated proteins including FUS and hnRNPA1. In the case of tau droplet, however, its principles and its relationship with tau aggregation are still unclear. This dissertation will guide you through a tour to build physical models that explain the driving forces of tau forming droplets, and to use these models to inform our new understandings of tau aggregation.

Table of Contents

Acknowledgements	iv
VITA of Yanxian Lin.....	vi
Abstract	viii
Table of Figures	xi
Chapter 0. Introduction.....	1
Tau protein	6
<i>Functional roles of tau protein</i>	6
<i>The chemistry of tau protein</i>	7
<i>Current understandings of tau aggregation mechanisms</i>	8
Liquid liquid phase separation of protein.....	9
Occurrence, biological functions, pathological connections.....	9
<i>Molecular elements that drive protein LLPS</i>	11
<i>LLPS of tau protein</i>	11
<i>Complex coacervation</i>	12
Chapter 1. Cofactors are Essential Constituents of Stable Tau Fibrils.....	15
Introduction.....	16
Fibrils assemble when cofactors are present	17
Fibrils depolymerize when cofactors are digested	18
Bound cofactors are required to stabilize tau fibrils.....	21
Discussion	23
Figure SI	26
Chapter 2. Tau-RNA Complex Coacervation.....	30
Introduction.....	31
Tau-RNA complex coacervate is reversible and a dynamic liquid phase.	35
Tau-RNA complex coacervate phase diagram.....	40
Flory-Huggins-Voorn-Overbeek Fit to Experimental Phase Diagram.....	42
Application to cell-complex coacervate co-culture.....	46
Discussion	49
Conclusion	54
Figure SI	56
Chapter 3. Electrostatically Driven Complex Coacervation and Aggregation.....	64
Introduction.....	65
Tau amyloid aggregation colocalizes with the dense phase of LLPS-CC.....	66
The extent of amyloid aggregation is independent of LLPS-CC	68
Half time and monomer dependence of amyloid aggregation are independent of LLPS-CC ...	72
Aggregation-signature conformation is independent of LLPS-CC	76
Amyloid aggregation can be modulated independently of LLPS-CC	80
Different types of tau LLPS exist and possess different properties	83
Discussion	85
Conclusion	90
Figure SI and Tables	91
Chapter 4. Hydrophobic vs Electrostatic Interactions in Coacervation and Aggregation.....	99
Introduction.....	100
Tau undergoes LLPS at high salt concentration.....	103
LLPS-HS undergoes irreversible maturation.	107

LLPS-HS triggers canonical tau amyloid aggregation	109
Dehydration facilitates hydrophobically driven LLPS-HS	112
Dehydration reduce tau dynamics and trigger oligomer formation	115
P301L promotes hydrophobic interactions	118
Discussion	120
Figure SI and Tables	126
Conclusion and Outlook	136
Reference	139
Materials and Methods	160
Protein expression and purification	160
Preparation of tau-polyanion droplets and microscope imaging.	161
Spin labeling and cw EPR	162
Cw EPR spectra analysis	163
Double Electron Electron Resonance (DEER)	164
Overhauser Dynamic Nuclear Polarization	165
Turbidimetry and brightfield microscopy	166
ThT assays	167
Determining tau-RNA CC composition	168
Flory-Huggins based Voorn-Overbeek (FH-VO) modeling	169
Determining phase separation temperature	171
Calculation of non-ionic entropy and enthalpy of coacervation	173

Table of Figures

Figure 0-1 Human tau isoform, charge and hydrophobicity.....	8
Figure 1-1. Fibrils depolymerize upon cofactor digestion.....	20
Figure 1-2 Cofactors are bound to fibrils and partially digested.	23
Figure 2-1. Steady tau dynamics and reversible droplet formation of tau-RNA complex coacervates.....	39
Figure 2-2 FH-VO modeling of tau-RNA CC.	43
Figure 2-3 Tuning experimental conditions to catch tau-RNA complex coacervates in presence of living cells.....	48
Figure 3-1. Bright field and confocal microscope images of tau-polyanion LLPS and amyloid aggregation.....	68
Figure 3-2. LLPS and amyloid aggregation of tau-heparin at varying [NaCl] and [heparin].	71
Figure 3-3. Effects of LLPS on tau-heparin aggregation half time and monomer dependence.	75
Figure 3-4. LLPS dependence of tau aggregation-signature conformation.....	79
Figure 3-5. Dependence of LLPS on modulating amyloid aggregation.	82
Figure 3-6. LLPS and amyloid aggregation of LLPS-CC vs LLPS-high salt.	85
Figure 4-1. Tau undergoes LLPS at high salt concentration.	106
Figure 4-2. FLIM fits of tau-RNA LLPS-CC and tau LLPS-high salt.	109
Figure 4-3. Correlation of LLPS-high salt and amyloid aggregation.	111
Figure 4-4. LLPS high salt undergoes dehydration.	115
Figure 4-5. Site specific dynamics of tau187 upon LLPS-high salt.	118
Figure 4-6. Effects of P301L mutation on LLPS and amyloid aggregation of tau at high salt concentration.....	120
Figure 4-7. Schematic diagram of dehydration-driven droplet-to-fibril transition.....	125

Chapter 0.

Introduction

A part of the material presented in this chapter is reproduced from Jho, YongSeok, Hee Young Yoo, Yanxian Lin, Songi Han, and Dong Soo Hwang. “Molecular and Structural Basis of Low Interfacial Energy of Complex Coacervates in Water.” *Advances in Colloid and Interface Science*. Accessed September 14, 2016. The author of this dissertation, among coauthors of the reprinted article, retains rights to include the reproduced materials in this dissertation with no requirement of permission from the publisher.

For details, please visit <https://www.elsevier.com/about/policies/copyright#Author-rights>

Tau is a protein mainly found in neurons in central nervous system that is known to help stabilize microtubules. In healthy conditions, tau is highly hydrophilic and soluble in aqueous environment under wide ranges of pH, temperature and ionic strength. However, under pathological conditions, tau forms irreversible, insoluble and cross- β -rich aggregates – a process called amyloid aggregation. Amyloid aggregation of tau into specific fibril strain is a hallmark of Alzheimer's disease (AD) [1]–[3], and has been observed under several other neurodegenerative diseases including progressive supranuclear palsy, frontotemporal dementia, Pick's disease and chronic traumatic encephalopathy [4], [5]. Despite the pathological significance of amyloid aggregation of tau, the pathways from soluble tau to insoluble amyloid aggregates have still not been identified nor replicated in any non-human system, neither *in vitro* nor *in vivo*. Finding the pathologically relevant amyloid aggregation pathway, as manifested in the generation of disease phenotypic fibril structures [6]–[9] is critical for understanding the underlying disease pathogenesis and for developing therapies.

Besides soluble state and solid-like aggregates, proteins have been observed to undergo liquid liquid phase separation (LLPS) *in vivo* and *in vitro*. LLPS yields a protein-dilute phase separated from a protein-rich phase, which is often observed in the form of liquid droplets. Some droplets have been observed as membraneless organelles *in vivo* that facilitates essential biological functions [10]–[12], while others are reported to initiate and/or promote amyloid aggregates, with many examples thus far focusing on ALS-related proteins, including FUS [11], [13], [14], [15, p. 201], hnRNPA2B1 and hnRNPA1 [16], TDP-43 [16], [17], C9ORF72 [18]–[20] and Ddx4 [21]. At the same time during the development of the work in this

dissertation, we and others found tau undergo LLPS to form droplets *in vitro* and *in vivo*. Despite the functional and pathological significance of protein droplets, our understandings of tau droplets, in terms of their physical nature and their connections with tau biological function and pathologic aggregation, are just in the infant stage. This dissertation is set to explore two key questions: 1) what kinds of physical models can explain tau droplets and 2) can these models inform our understanding of tau amyloid aggregation?

In early 2017 at the beginning of the work in this dissertation, our group and collaborators found tau binds RNA *in vivo* and forms droplets *in vitro* through electrostatically driven complex coacervation (LLPS-CC)[22]. Soon later, we found tau is also able to undergo LLPS-CC with heparin[23]. Before these observations, both heparin and RNA have been used as cofactors to induce tau aggregation[24], [25]. However, whether the cofactors serve as reactants that incorporate into the product fibrils or act as catalyst that can be removed without breaking the fibrils has not been resolved. This is a basic question to which the answer dictates our interpretation of aggregation pathways in the droplets of tau-heparin, tau-RNA or any other tau-cofactor droplets. Chapter 1 of this dissertation therefore begins with *in vitro* tau amyloid aggregation with droplet-forming cofactors, RNA and heparin, resolving whether cofactors act as reactants or catalysts, and eventually determining whether these cofactors participate in the interactions that are responsible for the fibril stability. The outcomes of this chapter found that cofactors, specifically heparin and RNA, bind to tau proteins, and incorporate into tau fibrils in certain stoichiometry, and that the bound cofactors are essential for stable and seeding-competent tau fibrils. RNA, heparin-like heparan sulfates and other cofactors have been shown

to bind tau *in vivo* [22], [26], [27]. The results of this chapter therefore imply that in neurons under pathologic conditions, tau aggregation could be facilitated by interactions with polyanionic cofactors.

With the roles of cofactors on tau fibrils established, we set foot to study the physical nature of tau droplets, in particular those formed by cofactor-induced tau LLPS-CC. Chapter 2 aims at understanding tau-RNA droplets, measuring its reversibility, determining whether it is a kinetically transient state or a thermodynamic equilibrium state, mapping its phase diagram, and finally demonstrating using phase diagram to guide selection of temperature, concentration, ionic strength to tune the on and off of tau-RNA droplets. Outcomes of this chapter found tau-RNA droplets are a reversible and equilibrated phase, with a narrow equilibrium window near cellular conditions. Its phase diagram can be captured quantitatively using both Flory Huggins-based theory and state-of-the-art field theoretic simulation. Both theory and simulation show that although electrostatic interactions are key to complex coacervation, factors that contribute to entropy gain are critical to driving tau-RNA LLPS. The knowledge gained from Chapter 2 provides a powerful tool to design experiments that perturb the tau concentration, ionic strength and temperature *in vivo*, to tune the tau droplets to reversibly form or dissolve. This knowledge can also be used to predict or understand biological mechanisms that may be favorable towards LLPS

The equilibrium nature of tau-RNA LLPS-CC is achieved at healthy conditions. What would happen under pathological aggregation-prone conditions? Chapter 3 is set to characterize aggregation-prone tau-cofactor droplets, as represented by tau-heparin droplets,

in order to understand the impacts of LLPS-CC on cofactor-induced tau aggregation, in terms of tau conformation, aggregating kinetics and fibril quantity. Results of Chapter 3 showed that none of these properties are influenced directly by LLPS-CC, and that LLPS-CC and cofactor-induced aggregation of tau merely occur under overlapping conditions of enhanced intermolecular interactions and localization, but are two independent processes.

The equilibrium nature of tau-RNA droplets and the aggregation-independence of tau-heparin droplets together imply that electrostatically interactions may not be the most relevant forces that droplets can steer to interfere fibril formation. Chapter 4 introduces a novel kind of tau LLPS under very high salt concentration (LLPS-HS). By excessive salt, LLPS-HS diminishes electrostatic interactions, such as charge-charge and dipole-dipole interactions that are ionic strength sensitive and likely dominant in tau-polyanion LLPS-CC. The outcomes show LLPS-HS is driven by dehydration facilitating hydrophobic interactions, that can be promoted by pathological mutation. In contrast to LLPS-CC, the LLPS-HS itself directly drives amyloid aggregation of tau, therefore can serve as a model LLPS system to study the manifest of hydrophobic interactions on amyloid aggregation. The contrast dependence of tau aggregation between LLPS-CC and LLPS-HS imply that tau is capable of LLPS through both electrostatic and hydrophobic interactions, and that the nature of the interaction driving tau condensation is the differentiating factor between aggregation-prone and aggregation-independent LLPS.

Tau protein

Functional roles of tau protein

Neuron cells are fundamental units in human brain. Neurons establish their spatial connections by extending their cytoplasm through axons and dendrites, resulting in dramatic change of morphology [28]. Those extensions are thought to be the consequence of the stabilization of microtubules along certain direction [28], [29]. Among proteins that can regulate microtubule stabilization are microtubule associated proteins (MAPs). One of the MAPs is tau.

Tau protein was found almost simultaneously in United States and Europe in 1970s [30]. In human brain, tau protein is segregated in the axon-neuropil domains of neurons, and mostly abundant in the central nervous system and less abundant in the spinal cord and peripheral nervous system [31]. Tau is mainly found in the cytoplasm, where tau interacts with many proteins, of which the most studied are tubulins. Tau was first discovered as a protein that stabilizes microtubule polymerization. Its depletion and weaken microtubule binding as a result of hyperphosphorylation, certain mutations and abnormal 3R/4R ratios, will inhibit growth of microtubule and consequently interrupt development and normal functions of neurons [29], [32]. Besides microtubule, tau also interacts with many stress granule related proteins[33], as well as the membrane [34] and is also found in nucleus and plays a role in neuronal DNA and RNA protection [35], [36] [37].

The chemistry of tau protein

Tau has six isoforms in adult human brain. They are results of alternative splicing of mRNA from tau gene in Chromosome 17, and differ in the number of insertions on the N terminal, referred to as 0N, 1N or 2N, as well as with/without the third repeat domain, referred to as 4R/3R, respectively (Figure 0-1). 0N3R, 0N4R, 1N3R and 1N4R are major isoforms of tau in adult human brain, contributing to approximately 20~25% each [38].

Tau is one of the canonical intrinsically disordered proteins (IDP) that lacks dominant conformation or stable secondary structure, with only transient secondary structure reported [39]. In healthy conditions, tau is highly hydrophilic and soluble in aqueous environment under wide ranges of pH, temperature and ionic strength. Its six isoforms contain ~35% of charged amino acids, ~20% of hydrophilic amino acids and less than 5% of aromatic residues. Its charge and estimated hydrophobicity distribution are shown as (Figure 0-1). *In vivo* tau undergoes various post translational modifications (PTMs), including phosphorylation[2], glycosylation, glycation, acetylation, deamidation, etc, which further change its charge/hydrophobicity in a dramatic and complicated way [5], [40].

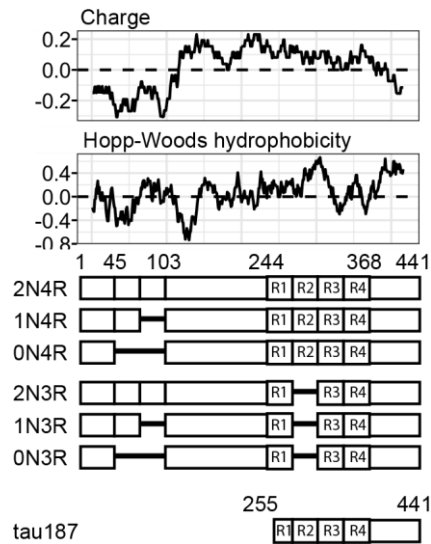


Figure 0-1 Human tau isoform, charge and hydrophobicity.

Charge and Hopp-Woods hydrophobicity plot are averaged by 25 consecutive residues.

Current understandings of tau aggregation mechanisms

The mechanism of tau aggregation *in vivo* is unclear and debated. Abnormal hyperphosphorylation has been shown to trigger tau conformational change and subsequent aggregation [41], [42]. However, the phosphorylation of tau on certain sites can inhibit tau aggregation [43]. Meanwhile, certain mutations have been associated to tau aggregation in frontotemporal dementia [34], [44], [45], and abnormal ratio of 3R/4R was shown to result in increased tau phosphorylation and misregulated tau-microtubule binding [46]. While the influence of tau hyperphosphorylation, mutations and abnormal isoform ratios on the functions of tau beyond microtubule binding remains to be elucidated, it is clear that all of these are detrimental to neurons and may collectively contribute to the neuronal dysfunction or death.

In vitro tau aggregation has been studied since 1980s [5]. Almost all studies rely on additional compound to trigger fibrillization. The most frequently used compounds include RNA [25] and sulfoglycosaminoglycans (sGAGs), represented by heparin [24]. Prevalent models of tau aggregation involve two processes, tau solution state to intermediate state, and intermediate state to fibrils. While the molecular identity of tau intermediate state is not entirely clear, studies have shown such intermediate state can be oligomeric [47], resembling fibril conformation [48]–[50], and can seed aggregation both *in vitro* [51] and *in vivo* [52]. Most recent cryo-EM studies showed the aggregation of tau in different diseases results in fibrils with different configurations [53]–[56], suggesting that tau undergoes different pathways in brains with different neurodegenerative diseases, and consequently tau may have different intermediate states leading to different fibril strains.

Liquid liquid phase separation of protein

Occurrence, biological functions, pathological connections

Besides monomeric solution state and solid-like aggregates, proteins are able to be condensed while remain fluidic. This is saying proteins can form a network of diverse interactions with each other, while retain certain degree of translational mobility. This results in a structure that has clear and smooth boundary, and can merge/split simultaneously, referred to as **droplet**.

Fluid phase compartmentalization with striking resemblance to droplets has also been observed in eukaryotic cells [21], many of which are referred to as RNA granules [57], and/or

membraneless organelles [58], in which co-localization of proteins [22] and/or RNA has been reported [23-25] and links to transcriptional regulation and signal transduction suggested [26, 27]. The liquid nature of these compartments has not been emphasized until the most recent decade. Brangwynne et al in 2009 found that germline P granules are liquid droplets [10]. P granules localize by controlled dissolution/condensation, and the key that enables this is the dynamic and reversible nature of droplets. Later many traditional cellular compartments were identified as liquid droplets including nucleoli [59], nuclear bodies and stress granules [60] among others. The list of proteins found undergoing LLPS *in vivo* grows rapidly.

In many cases LLPS bear essential functions *in vivo*. However, in some other cases, LLPS associates with, and/or triggers amyloid fibril formation. A canonical example is FUS protein, a prion-like protein containing intrinsically disordered domains of which the aggregation is associated with neurodegenerative disease ALS. Patel *et al.* in 2015 [15] reported that FUS undergoes LLPS and forms liquid droplets both in cells and *in vitro*. Upon incubation, liquid droplets of FUS convert from fluid to aggregates, and this conversion is accelerated with aggregation-prone mutations. Molliex *et al.* in 2015 [11] reported another ALS-related IDP hnRNPA1 undergo LLPS and form droplets both *in vivo* and *in vitro*, and protein aggregation is enhanced in droplets. Subsequently, TDP-43 [16], [17], [61], C9ORF72 [18]–[20], Htt-94Q [62] and many other proteins have been reported to undergo LLPS-mediated amyloid aggregation. Therefore, it is hypothesized that liquid droplets in cells are trade-off between functionality and the risk of pathological aggregation [63].

Molecular elements that drive protein LLPS

The abundance of IDPs in protein LLPS makes it relevant to apply the physical principles drawn from studies of polymers. In an aqueous solvent, LLPS of proteins like FUS containing low-complexity domains (LCD), i.e., long stretch of low diversity of amino acids, can be driven by dipolar interactions contributed by the polypeptide backbone and polar side chains like glutamine (Q), asparagine (N) and serine (S) [64], [65]. Consistently, dipolar interactions between backbone and solvent have been shown to encourage compact conformation of IDP [66]. Proteins that contain enriched charged amino acids can be driven by charge-charge interactions. Examples include LAF-1 [67], DDX4 [21] and tau [68] among others. In these and other systems, the charge-charge interactions can result from proteins with/without RNA or other polyanions. Other interactions including multivalent (cooperative) interactions [69], pi-effects [70] and metal ion-specific interactions [71] can also contribute to driving forces of LLPS of IDPs. Despite many examples of successful modeling, applying the concepts from polymeric phase separation is challenging due to the heteropolymer nature of proteins and the potential non-equilibrium and/or path-dependent behaviors of protein droplets. Therefore, a case-by-case examination is still needed.

LLPS of tau protein

Tau is overall hydrophilic and highly charged IDP, with ~20% polar amino acids and 30~40% charged amino acids. Tau can interact with RNA and other polyanions *in vivo*, which makes polyelectrolyte complex coacervation (CC), among other kinds of polymeric phase

separation, relevant to the studies of tau LLPS. Complex coacervation is usually defined as a process of LLPS when mixing a polyelectrolyte in aqueous solution with a second compound bearing sufficient charges of the opposite. CC has been observed in between oppositely charged synthetic and natural polymers including polyelectrolytes, polypeptides, polysaccharides, folded/unfolded proteins, DNA/RNA, as well as colloids and nanoparticles [72]–[79].

Recently, the term ‘protein droplets’ was coined to refer to a broad range of phenomena in which charged proteins, often of intrinsically disordered nature, associate with RNA species and undergo μm -scale phase separation to form protein droplets [28, 29]. While it appears that in many cases these are likely to be complex coacervate systems, the literature on this is confusing because systematic physical characterization of these complexes are lacking. In fact, most of these reports focused on the binding behavior between specific biopolymer constituents [23, 24, 30], with only few recent studies unraveling the physical properties of these protein droplets [31, 32] and even fewer on discussing the molecular [33] or structural [34] basis of this fascinating phenomenon.

Complex coacervation

Complex coacervate is considered to be first discovered in 1911 [80]. Its definitive features come from its driving force of charge-charge attraction. CC can happen between polyelectrolyte (PE) and colloid, resulting in two types of CC: PE-PE and PE-colloid. The latter can occur between PE and globular proteins or micelles [79]. For relevance to IDP tau,

we only discuss PE-PE CC here. For symmetric polycation-polyanion CC, the maximal droplet volume fraction is achieved when the number of positive charge and negative charge match. Relying on the electrostatic attraction, CC is sensitive to charge screening by electrolytes in aqueous solution.

In the dense phase of CC, the polycations and polyanions strongly overlap with each other to form a network with a mesh size that is much smaller than the gyration radius, similar to that of a semidilute polymer solution [81]. Such resemblance has also been seen in network structure of complex coacervates formed by biopolymer DNA, hyaluronic acid, and polyaspartic acid, regardless of their distinct charge moiety and backbone chemistry [82]. The density of the dense phase of CC is heterogeneous, varying in domains of 0.1~10 μm size, which is larger than the correlation length of the polyelectrolyte [81] [83] and dependent on polycation/polyanion ratio [84] and ionic strength [84] [85]. Both the network mesh size and the dense domains are constantly fluctuating [81] and rearranging with time [86] [87], resulting in a dynamic and heterogeneous internal structure.

In PE-PE CC dense phase, polycations and polyanions move independently with reduced diffusivity [86]. The water diffusion coefficient inside the complex coacervate phase, was found to be at a similar order of magnitude as bulk-water, apparently higher than bound-water [87] [88]. A layer of intermolecular hydrogen bonds was assumed to exist between polycations and polyanions [89], and consistently, the level of non-freezing-water is higher due to the coacervation [90]. The fluctuating and heterogeneous internal structure plus the bulk-like

diffusivity of water, is well represented by biphasic structure [91] and bicontinuous structure [92] found in certain cases.

Despite the concentrated state and presence of long range interactions, the polyelectrolytes in the dense phase of CC have a conformation that is very close to the ideal Gaussian conformation [81] and insensitive to ionic strength or polyanion-polycation ratio [93]. Such conformation preserving feature of CC has been shown to explain solution-like conformation of biomolecules in CC [94]. However, its manifest in the protein interactions or aggregation has not yet been revealed.

Chapter 1.

Cofactors are Essential Constituents of Stable Tau Fibrils

Material presented in this chapter is reproduced from Fichou, Yann, Yanxian Lin, Jennifer N. Rauch, Michael Vigers, Zhikai Zeng, Madhur Srivastava, Timothy J. Keller, Jack H. Freed, Kenneth S. Kosik, and Songi Han. “Cofactors Are Essential Constituents of Stable and Seeding-Active Tau Fibrils.” *Proceedings of the National Academy of Sciences* 115, no. 52 (December 26, 2018): 13234–39. The author of this dissertation, among coauthors of the reprinted article, retains copyright of the reproduced material, and needs not obtain permission to reproduce it in this dissertation.

For details, please visit <https://www.pnas.org/page/about/rights-permissions>.

Introduction

Aggregation mechanisms of tau are most often studied with recombinant tau proteins or fragments. *In vitro* fibrillation of tau is typically triggered with the help of cofactors, most commonly heparin [95], but also other cofactors such as RNA [25] or arachidonic acid [96]. In the last few years, seeding tau aggregation has been shown to be possible by adding pre-made fibrils (seeds) to fresh monomers, but the seeding process is still improved by the presence of cofactors (RNA or heparin) in solution [51], [97]. It has been shown that heparin is a limiting factor in fibril formation [98], [99], but the exact nature of association of heparin with the mature fibrils remains unclear with conflicting reports on whether heparin is part of [100] or not part of mature fibrils [99], [101]. As a result, the roles of heparin in tuning fibril formation, structure and stability is unknown. For instance, heparin-induced fibrils were shown to be more stable than AD fibrils using chemical denaturation [49], [50], but whether heparin contributes to this stability was not addressed. In this study we assess whether cofactors are crucial constituents of mature fibrils and contribute to their stability, or whether they only catalyze aggregation toward a self-sustained protein assembly.

Tau aggregates have been shown to propagate from neuron to neuron, and to be able to seed aggregation [49], [102], i.e. convert naïve tau monomers into aggregates. This led to the hypothesis that, *in vivo*, monomeric tau can spontaneously polymerize into amyloid filaments when an appropriate seed template is provided. For that reason, pathological origins of tau aggregation have mostly been searched in the properties of tau itself, such as hyperphosphorylation, cleavage, high local concentrations, alternative splicing, but marginally

in abnormal interactions with other cofactors. Paradoxically, cofactors are always used for *in vitro* aggregation of tau, and even assumed to be biologically relevant. Therefore, gaining an understanding about the influence of cofactors on mature fibril properties will (i) provide key insight into the role of cofactors in fibrils stability and conformation *in vitro*, and (ii) guide the search for cofactors that assist in seeding and spreading of tau aggregation *in vivo*. In this study, we used a set of biochemical tools together with electron paramagnetic resonance (EPR) to characterize the consequences of cofactor removal after fibril formation.

Fibrils assemble when cofactors are present

We used a truncated version of the longest human tau isoform 2N4R that contains the four repeat domains (R1-R4), as well as the entire C-terminal region (residues 255-441, named here as tau187), from which one of the two cysteines was mutated (C291S) in order to perform site-directed spin labeling for EPR [103], [104]. The construct, with the addition of the aggregation-promoting disease mutation P301L [105] is referred to as tau throughout the manuscript (Fig. S1A). Polydisperse heparin (average MW 15 kDa) and polyU (RNA, average MW 900 kDa) were incubated with tau to induce fibrillation. The addition of heparin or RNA to tau resulted in amyloid fibril formation as verified by significant increase of Thioflavin T (ThT) fluorescence intensity (Fig. S2) and the presence of fibrillar structures captured by transmission electron microscopy (TEM, Fig. S1B, C). We referred to the heparin-induced and RNA-induced tau amyloid fibrils as heparin fibrils and RNA fibrils, respectively.

Fibrils depolymerize when cofactors are digested

We tested whether these cofactors act as catalysts that assist fibril formation and subsequently dissociate from the product, or whether they are reactants that are part of the fibril scaffold and are necessary to ensure the stability of mature fibrils. To address this question, we investigated the amyloid fibril quantity by preparing heparin fibrils and RNA fibrils, and then degrading the cofactors via enzymatic digestion.

Heparin and RNA are cofactors that can be digested using heparinase and RNase, respectively (see **Materials and Methods**). In their digested form, both cofactors are incapable of triggering fibril formation (Fig. S3). ThT fluorescence, which provides an *in situ* measure of cross- β sheet structure abundance, was used to quantify the amyloid fibrils present in the sample. Heparinase and RNase were added to heparin fibrils and RNA fibrils after maximal ThT fluorescence was reached, and the samples incubated for over 7-8 hours, resulting in a 20-30% and 70-80% decrease of ThT fluorescence, respectively (Figure 1-1A). Similar results were obtained when performing digestion on pelleted fibrils upon ultracentrifugation, showing that the decrease in ThT upon enzyme addition is not due to degradation of ThT-active soluble oligomers or fibrils (Fig. S4). Control experiments with buffer added to heparin and RNA fibrils in the absence of enzymes showed a ThT fluorescence decrease of ~10% and ~30%, respectively (Figure 1-1A), which are attributed to result from dilution and potential traces of RNase.

The digestion of tau amyloid fibrils was independently investigated by continuous wave EPR (cw-EPR). cw-EPR of paramagnetic spins tethered to tau has been previously used to

assess the packing and mobility of tau fibrils [103]. The cw-EPR spectra of spin-labeled amyloid fibrils can be decomposed into 3 components, a mobile component corresponding to soluble low molecular weight (MW) species, an immobile component corresponding to high MW species (oligomers, aggregates, etc), and a spin-exchange component resulting from spin labels that are within 5 Å proximity due to parallel, in register, amyloid cross-β stacking of tau [103]. Here we spin-labeled the native cysteine 322, prepared tau fibrils with heparin and acquired cw-EPR spectra before and after heparinase treatment. The spectra were fitted using an established simulation protocol [103] into populations of mobile, immobile and spin exchange components (Figure 1-1B). Fitting results implied that $93 \pm 1\%$ of the spin-labeled tau in heparin fibrils are in in-register amyloid cross-β stacking, which decreases to $84 \pm 2\%$ after digestion. This loss was mostly compensated by increase of low MW species ($2 \pm 0.3\%$ before and $13 \pm 2\%$ after digestion), while the high MW species remains similar ($4 \pm 1\%$ before and $3 \pm 1\%$ after digestion) (Figure 1-1C).

The increase of low MW species interpreted from cw-EPR after digestion was further tested for both heparin and RNA fibrils using blue native polyacrylamide gel electrophoresis (BNPAGE, Figure 1-1D). The results showed that tau fibrils after digestion release a significant amount of solubilized monomer and dimer, in contrast to tau fibrils before digestion where no corresponding band could be discerned. Note that the ratio of monomer/dimer remained unchanged for sample before aggregation (“soluble” lane) and after digestion. These results are direct evidences confirming that the decrease of ThT fluorescence observed in Figure 1-1A results from a depolymerization of tau fibrils.

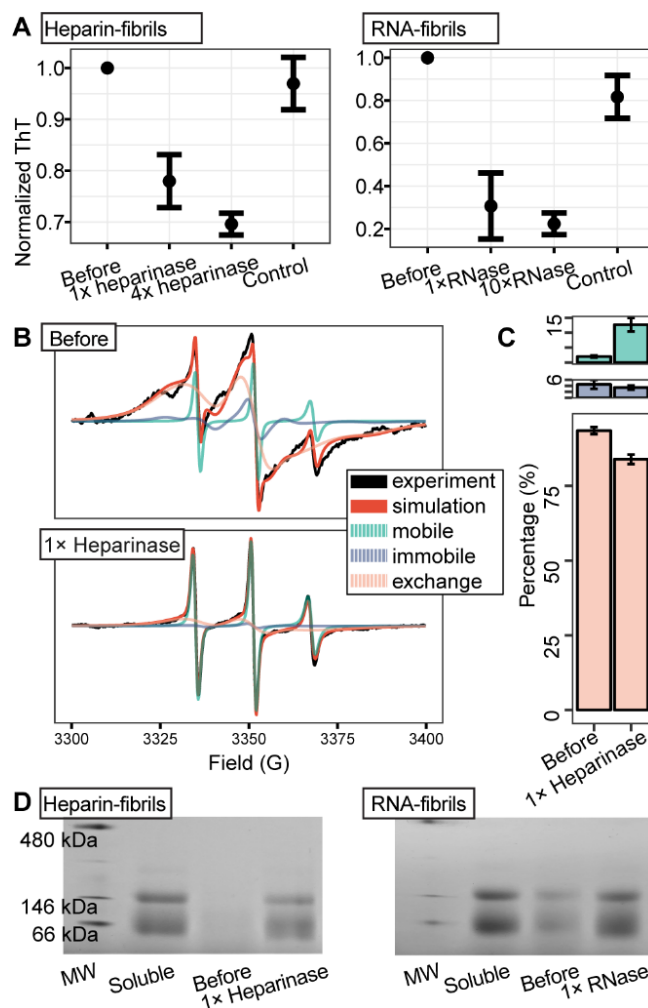


Figure 1-1. Fibrils depolymerize upon cofactor digestion

A. ThT fluorescence of heparin-induced tau fibrils and RNA-induced tau fibrils before and after incubation with different concentration of heparinase/RNase. ThT fluorescence value measured before enzyme addition was used as the normalization values. **B.** CW-EPR spectra (black) of tau heparin fibrils spin labelled at site 322, before and after incubation with heparinase. The simulation spectra (red) is composed of mobile (green), immobile (purple) and spin exchange component (orange). **C.** Population of each component extracted from cw-EPR spectra analysis. **D.** BN-PAGE of heparin and RNA fibrils before and after incubation. Freshly prepared tau monomers were loaded as reference (soluble). In all panels, 1× heparinase: 1 Unit of enzyme per 1 µg of heparin; 1× RNase: 2.5 µg/mL; Error bars show standard deviation (n≥3).

Bound cofactors are required to stabilize tau fibrils

We learned that digesting cofactors depolymerized tau fibrils. However, extending the digestion for longer times or increasing heparinase and RNase concentration by 4 times and 10 times respectively did not significantly decrease the remaining ThT fluorescence (Figure 1-1A), which suggest that the maximal digestion had been reached and the remaining ThT fluorescence came from species that are not sensitive to heparinase/RNase digestion. These species can originate from either (i) fibril populations that are stable without cofactor, or (ii) fibril populations stabilized by cofactors that are undigestable due to steric hindrance. To answer this question, we quantified the amount of undigested cofactor by separating the soluble cofactors from fibrils.

Mature RNA fibrils were pelleted, washed and incubated with or without RNase, referred to as digested and non-digested RNA fibrils, respectively. Digested and non-digested RNA fibrils were subject to dialysis and the percentage of equilibrated RNA that flowed through the dialysis membrane was measured by UV absorption and regarded as effectively digested RNA. Digested and non-digested RNA (without tau) were used as controls. Results presented in Fig. 2B revealed a degree of RNA digestion of $81 \pm 2\%$ and $36 \pm 3\%$ for digested and non-digested RNA fibrils respectively. These results confirm that the majority of the RNA in RNA fibril was digested upon RNase treatment, while the small but significant difference between digested fibril ($81 \pm 2\%$) and digested RNA alone ($90 \pm 4\%$) reveals that a fraction of RNA in the fibril is protected against digestion. The remaining amount of $10 \pm 2.5\%$ undigested RNA is in qualitative agreement with the remaining ThT fluorescence ($8 \pm 2\%$) observed after

digestion of pelleted fibrils (Fig. S4). Note the $36 \pm 3\%$ of RNA flowed through in the non-digested fibrils is close to the non-digested RNA control ($28 \pm 5\%$), suggesting it originates mostly from RNase contamination inside the dialysis tube that digests RNA over the dialysis time of 24 h.

Heparin fibrils were prepared using spin labelled heparin (heparin-SL), detectible by cw-EPR. The double integral of a cw-EPR spectrum is directly proportional to the quantity of spin-label, and hence yields the heparin concentration. We first confirmed using a ThT assay that heparin-SL triggers tau fibrillation. Digested and non-digested heparin-SL fibrils were subject to filtration ($0.2\ \mu\text{m}$) that allowed the soluble heparin to flow through, while retaining the large fibrils and associated heparin (Figure 1-2A). The concentration of heparin in the filtrate was determined by cw-EPR and compared to the concentration before filtration to calculate the percentage of soluble heparin (Figure 1-2B). Both digested and non-digested samples retained a significant amount of heparin ($42 \pm 8\%$ and $39 \pm 2\%$ flowed through, respectively), while the control with only heparin-SL (no tau fibrils) flowed entirely through ($108 \pm 6\%$). The observation that even after digestion a large portion of heparin is bound to fibrils is in qualitative agreement with the ThT fluorescence that retain 80% of its intensity after digestion (Figure 1-1A). We, however, could not detect a significant difference between digested and undigested samples, in part due to the large variation in the measurement of spin concentration ($\pm 8\%$ for the digested sample).

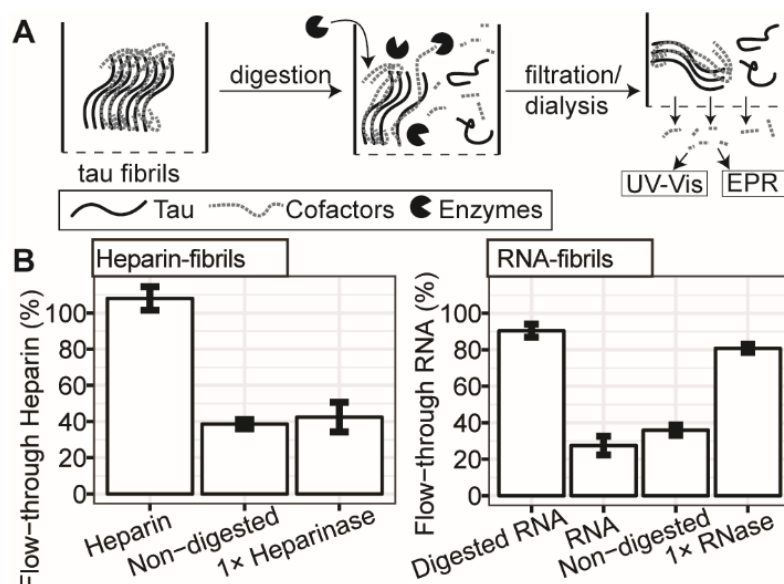


Figure 1-2 Cofactors are bound to fibrils and partially digested.

A. Schematic diagram of experiment procedures. Digested soluble cofactors were separated from tau fibrils via dialysis (RNA fibrils) or filtration (heparin fibrils), before measuring their concentration in the flow-through by cw-EPR (heparin) or UV absorbance (RNA). **B.** (left) The concentration of spin labelled heparin in the flow-through of a 0.2 μ m filter for heparin, heparin fibril before and after digestion. The concentration is given in percentage of the concentration before filtration. (right) RNA concentration outside a dialysis bag (12 kDa MWCO) at equilibrium was measured and the percentage of RNA that flowed through is given as Y axis. Errors bars show standard deviation of 3 independent repeats.

Discussion

We have demonstrated that mature recombinant tau fibrils require cofactors to be sustainably stable. Upon cleavage of cofactors by enzymatic digestion, the fibrils depolymerize, releasing soluble monomeric tau. The incomplete digestion of the cofactor molecules (heparin or RNA) is likely due to allosteric hindrance that prevents the enzymes to access and cleave their targets. The finding that in both RNA and heparin fibrils, only a defined

and reproducible amount of cofactor can be digested suggests that the fibrils are polymorphic, where in some types of aggregates the cofactors are protected from digestion, while in others they are accessible to the enzyme. The significant difference seen in Figure 1-1A between the maximum digestible RNA (60-70%) and heparin (~20%) could be explained by different molecular arrangements of the fibrils and/or by the nature of the enzymes, where RNase A (14 kDa) may be less sensitive to steric hindrance than heparinase I (43 kDa) to process its target.

Our work suggests that the high stability of heparin-induced fibrils previously observed [49], [50] is largely due to tau-cofactor interactions, and not due to superior tau fibril packing and stability. This highlights the need to further understand the role of cofactors in tuning the properties of tau fibrils of structure and stability.

The finding that a polyelectrolyte cofactor is essential for the stability of fibrils prepared *in vitro* has two major potential implications with respect to *in vivo* aggregates. (i) Polyanion-induced recombinant tau fibrils make limited models (of *in vivo* aggregates) that overestimate the role of cofactor, and (ii) there are unknown cofactor(s) in the fibrils formed in neurons, whose roles have been underestimated to date. While we cannot rule out (i), the data presented here make a strong case for (ii).

There is a large variety of bioelectrolytes that could interact with tau *in vivo*, including DNA, RNA, GAG, and ATP. Although tau is mostly present in axons [106], it is also found in neuronal nuclei [107] and is suspected to traffic in the extracellular matrix [108]. The complexity of the cellular environment and trafficking makes it very hard to unambiguously assess *in situ* the roles of a given cofactor in tau aggregation and the pathogenicity. GAG, in

particular heparan sulfate (HS), have been the most studied interaction partner to tau (see for instance recent review [109]), likely because (i) it was found co-localized with tau neurofibrillary tangles (NFTs) in AD brain [95], (ii) heparin is a very efficient cofactor in promoting aggregation *in vitro* [95] and (iii) HS has been shown to play an important role in tau internalization [110]. Although it is unclear when and how HS interacts with tau, as the former is exclusively present on the extracellular cell surface while the latter is mainly found in the cytoplasm, the fact that the NFTs co-localize with HS [95] suggests that HS might be incorporated into *in vivo* tau fibrils. Similarly, RNA has also been found to specifically associate with tau in neurons [111], to be sequestered in tau pathological assemblies, not only in AD brains, but also in Pick bodies [112], suggesting that RNA might also be part of the final tau fibrils. Recent advances in cryo-EM has allowed the identification of two very different fibril structures in AD brains [113] and Pick's disease [114], showing that different strains have very distinct atomistic fibril structures. If polyelectrolyte cofactors were present in the mature tau aggregates, they would not necessarily be visible on cryo-EM electron density map (their high flexibility would likely compromise their resolution), while their interactions with tau could in fact modulate the differentiation toward a given strain.

Figure S1

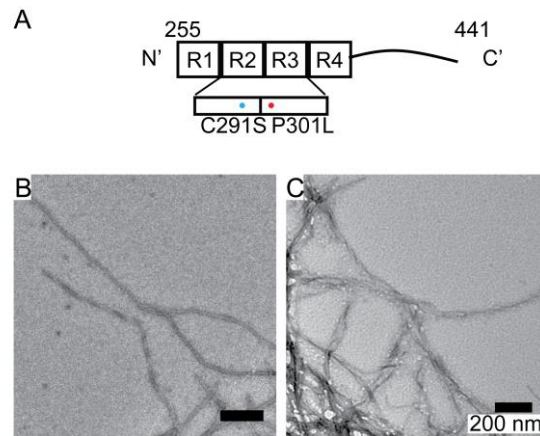


Fig. S1. Assembly of tau fibrils with cofactors. **A.** Schematic representation of the tau construct used in this work (2N4R 255-441) that include the four repeat domains (R1-R4) as well as the C terminal region; **B.** Representative TEM image of heparin-induced tau fibrils and **C.** RNA-induced tau fibrils.

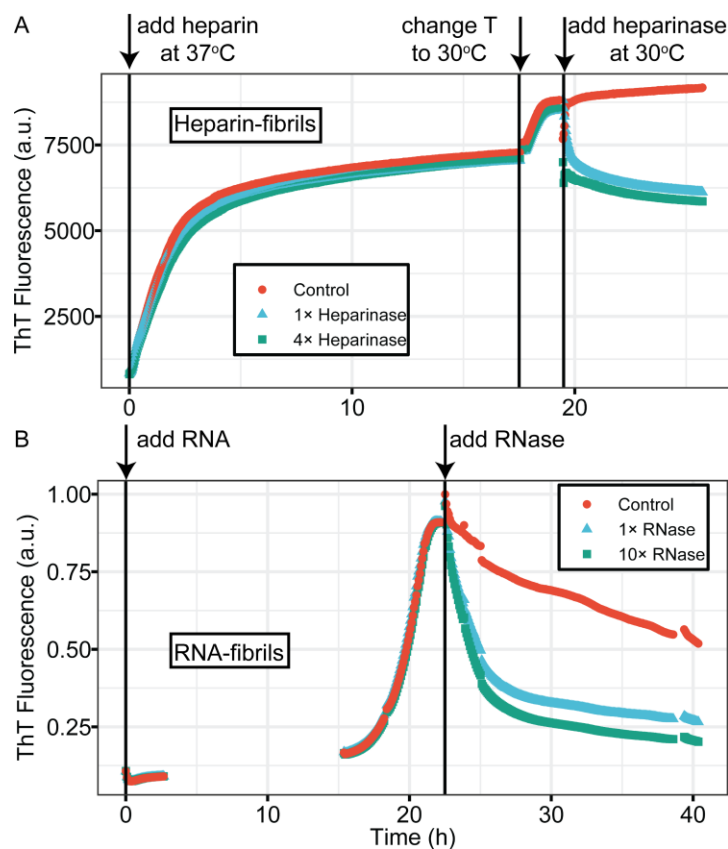


Fig. S2. ThT fluorescence trace of heparin-/RNA-induced tau fibrillation followed by cofactor enzymatic digestion. A. Heparin-induced samples were incubated at 37°C until heparinase treatment where temperature was decreased to, and stabilized at, 30°C. **B.** RNA-induced fibrillation and RNase treatment were performed at room temperature. In the control samples buffer was added instead of enzymes.

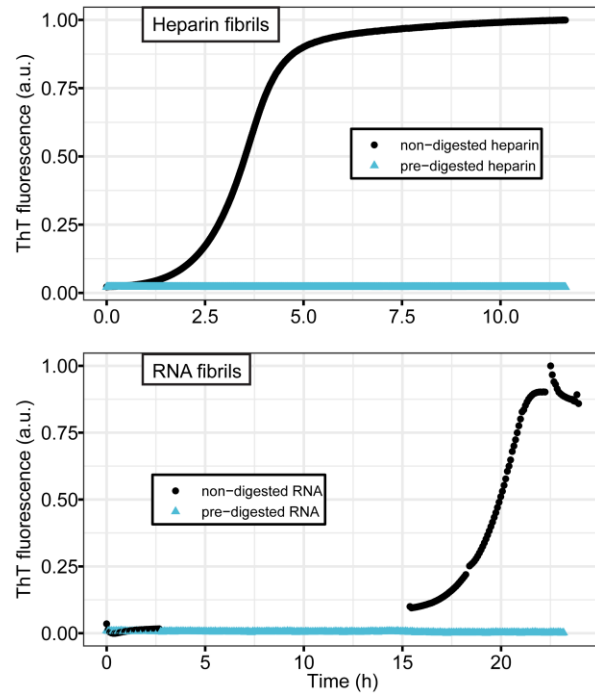


Fig. S3. ThT fluorescence of pre-digested heparin/RNA inducing tau fibrillization. Heparin-/RNA-inducing tau fibrillization were performed with pre-digested heparin/RNA at the same experimental conditions as described in Methods and Materials. Pre-digested heparin/RNA was prepared respectively using heparin pre-incubated with 1× heparinase overnight at 30°C or RNA pre-incubated with 200× RNase overnight to ensure full digestion.

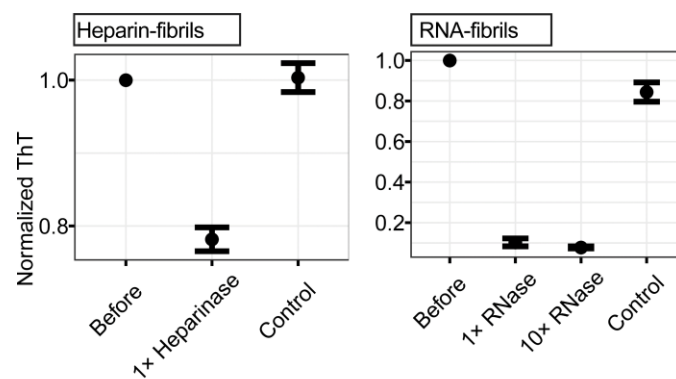


Fig. S4. Digestion of pelleted fibrils. The same experiments as in Fig. 1A were carried out, on fibrils that were first pelleted at 53,000 rpm (TLA-100.3) for 1h and resuspended in working buffer. Results are overall similar than without centrifugation (Fig. 1A), although a pelleted RNA fibril sample seems to be more susceptible to digestion (~90%) than non-pelleted fibril sample (70-80%).

Chapter 2.

Tau-RNA Complex Coacervation

Material presented in this chapter is reproduced from Lin, Yanxian, James McCarty, Jennifer N Rauch, Kris T Delaney, Kenneth S Kosik, Glenn H Fredrickson, Joan-Emma Shea, and Songi Han. “Narrow Equilibrium Window for Complex Coacervation of Tau and RNA under Cellular Conditions.” Edited by Yibing Shan, Naama Barkai, and Carlos Castaneda. *ELife* 8 (April 5, 2019): e42571. © 2019, Lin et al.

This article is distributed under the terms of the [Creative Commons Attribution License](#), which permits unrestricted use and redistribution provided that the original author and source are credited.

Introduction

Protein liquid-liquid phase separation (LLPS) is a process in which proteins assemble and partition into a protein-dense phase and a protein-dilute phase. The proteins in the dense phase form droplets, and retain liquid-like mobility, as shown by NMR measurements [94], [115]. The process of LLPS *in vitro* has been observed for decades [10], [57], [116]–[119], but the field has recently been invigorated by the realization that LLPS also occurs *in vivo*, suggesting a possible physiological role for these assemblies [10]–[12]. The overwhelming majority of proteins observed to undergo LLPS are intrinsically disordered proteins (IDPs) [120], and much of the research thus far has focused on ALS-related IDPs [11], [13], [14], [15, p. 201][16], [17] [18]–[20][21]. Recently, we and others discovered that another amyloid forming IDP, the microtubule binding protein tau, also undergoes LLPS [22], [121]–[124]. Interestingly, many of the LLPS forming IDPs have been observed to form amyloid fibrils in cell-free systems [14], [16], leading to a number of hypotheses regarding the physiological role of LLPS in regulating aggregation. In particular, a compelling idea is that protein LLPS may be an intermediate regulatory state, which could redissolve into a soluble state or transition to irreversible aggregation/amyloid fibrils [14]–[16], [22], [121].

In a healthy neuron, tau is bound to microtubules. When tau falls off the microtubule under adverse conditions to the cell, tau is solubilized in the intracellular space as an IDP. Under certain conditions, tau forms intracellular fibrillary tangles, a process linked to neurodegenerative tauopathies that include Alzheimer's disease. In recent work, we showed that tau in neurons strongly (nanomolar dissociation constant) and selectively associates with

smaller RNA species, most notably tRNA [22]. We also found tau and RNA, under charge matching conditions, to undergo LLPS [22] in a process determined to be complex coacervation (CC) [125]. We found that tau-RNA LLPS is reversible, and persisted for > 15 hours without subsequent fibrilization of tau, and hypothesized that LLPS is potentially a physiological and regulatory state of tau.

In this work, we characterize the phase diagram of tau-RNA LLPS using a combination of experiment and simulation, and thereby specify the conditions that drive the system towards a homogeneous phase or an LLPS state. We study a N-terminus truncated version of the longest isoform of human 4R tau *in vitro*, and first demonstrate that tau-RNA complexation is reversible, and that tau remains dynamic and without a persistent structure within the dense phase. The phase coexistence curve separating a supernatant phase from a condensate phase is determined by the system's free energy, which in turn is state dependent, *i.e.* dependent on concentration, temperature, salt, and the nature of the interaction strength between the various solution constituents, including the solvent. We construct the phase diagram from cloud-point measurements of the onset of complex coacervation under varying conditions of temperature, salt, and polymer concentrations. These experiments establish the features and phase coexistence boundaries of the phase diagram, which we then model using theory and simulation to rationalize and understand the physical mechanisms that drive and stabilize LLPS.

A number of theoretical models can be used to model LLPS, each with their own advantages and disadvantages. Ideally, one would turn to simulations at atomic resolution in

explicit solvent; however, such models are computationally prohibitive given the multiple orders of magnitude in time and length scales involved in LLPS. Turning to the polymer physics literature, theoretical treatments of simplified coarse-grained models are much more computationally tractable, and offer useful insight. Although approximate, analytical theories can be formulated, providing an extremely efficient platform for describing the thermodynamics of polyelectrolyte mixtures [126]. These include the Flory-Huggins model [127], the Voorn-Overbeek model [117], [128]–[133], the random-phase approximation [134]–[136], the Poisson-Boltzmann cell model [137], [138], as well as other more sophisticated approaches [139]–[141], which have been applied to synthetic polymers with low sequence heterogeneity [128], [142]–[145], and to proteins with single composition [21], [115], [146], [147]. While such models have been successful in describing simpler polyelectrolytes, it is less apparent that these models are suitable to describe the complex coacervation of the more complicated tau-RNA system. The simplest approach that one can use is the Flory-Huggins (FH) model, augmented by the Voorn and Overbeek (VO) correction to describe electrostatic correlations. This model is widely used to model LLPS; however, while experimental data can be fit to the model [21], [115], ultimately the FH-VO model has serious inadequacies. The original Flory-Huggins model is a mean-field theory, which means that fluctuations in polymer densities away from their average value in each phase are neglected. Augmenting the FH model with a VO treatment of electrostatics approximately accounts for charge correlations, but it entirely neglects chain-connectivity [148]. Thus, the FH-VO model is unable to model the spatially varying charge distribution along the polymer backbone. Ideally, one would like to

introduce chain connectivity, charge correlation, and uneven charge distribution into a more realistic polymer physics model; however, a full treatment of polymer density fluctuations is analytically intractable. One possible approach is to pursue a Gaussian approximation to field fluctuations, also known as the random phase approximation (RPA) [149]–[151]. The RPA model can be viewed as a lowest-order correction to the mean field approximation, and was recently introduced to describe the charge pattern and sequence-dependent LLPS of IDPs [152], [153]. The advantage of the RPA model, over the mean-field FH-VO model, is that charge correlations are introduced in a formally consistent manner. Nonetheless, it has been recently demonstrated that the RPA model fails to quantitatively predict polymer concentrations in the dilute phase, given that higher-order fluctuations are important in this regime [154], [155].

Of all the models described above, fitting experimental data with the FH or FH-VO theory is currently the preferred methodology in the LLPS community to describe and analyze phase diagrams. We demonstrate that this model can be fit to describe our experimental data, but the learning outcome from this modeling is limited. Thus, we take a different approach by computing the exact phase diagram of an off-lattice coarse-grained polyelectrolyte model using field theoretic simulations (FTS). FTS is a numerical approach that allows one to fully account for fluctuations, and thus to compute equilibrium properties from a suitably chosen coarse-grained representation of the true system without the need for analytical approximation. The ability to perform field theoretic simulations enables us to include the important physics of polymer sequence-specificity that cannot be captured by FH-VO, including charge distribution

and chain connectivity. Results from FTS are compared to those obtained from the FH-VO model.

The model substantiates the experimental phase diagram that the equilibrium window for the complex coacervation of tau and RNA under cellular conditions is narrow. Guided by the phase diagram, empirically obtained from *in vitro* experiments and validated by simulation, we finally show that LLPS of tau-RNA can be established and rationalized under cellular co-culturing conditions in the presence of live cells.

Tau-RNA complex coacervate is reversible and a dynamic liquid phase.

Truncated versions of the longest isoform of human 4R tau, residues 255-441 [156] and residues 255-368 were used to study tau-RNA complex coacervation (CC). A C291S mutation was introduced to either tau variant, resulting in single-cysteine constructs. Thioflavin T assays and TEM imaging were performed showing these variants retain the capability to form fibrils with morphology similar to full length tau. Unless otherwise specified, we refer to these two single-cysteine tau constructs as tau187 and tau114 (tau114 is close to K18, 244-372 [157]), respectively, while tau refers collectively to any of these variants (see **Materials and Methods** for experimental details). Importantly, experiments were performed with freshly eluted tau within 30 minutes upon purification to minimize the effects of possible disulfide bond formation. This minimizes the influence of the cysteine mutations on the LLPS behavior of tau-RNA CC. The single-cysteine containing tau187 can be singly spin labeled at site 322, referred to as tau187-SL (see **Materials and Methods**). Full length tau, tau187 and tau114

are overall positively charged with an estimated +3, +11 and +11 charge per molecule at neutral pH, respectively, based on their primary sequences. The charged residues of tau are more concentrated in the four repeat domains (Figure 2-1A). PolyU RNA (800~1000 kDa), which is a polyanion carrying 1 negative charge per uracil nucleotide, was used in this study and henceforth referred to as RNA (Figure 2-1A). Under ambient conditions, both tau and RNA are soluble and stable in solution. By mixing tau and RNA under certain conditions, a turbid and milky suspension was obtained within seconds, where tau and RNA formed polymer-rich droplets (dense phase) separated from polymer-depleted supernatants (dilute phase) (Figure 2-1B). These polymer-rich droplets are tau-RNA CCs. We began by determining the concentration of the dense and dilute phases. After mixing and centrifuging 60 μ L tau187-RNA droplet suspension, we separated a polymer-rich phase of volume <1 μ L with a clear boundary against the dilute supernatant phase. Applying UV-Vis spectroscopy (see **Materials and Methods**), we determined the concentration of tau and RNA inside the droplets as >76 mg/mL and >17 mg/mL with partitioning factors of >15 and >700 respectively. This is consistent with our previously findings that tau is virtually exclusively partitioned within the dense phase [22]. High protein concentrations are typically correlated with higher propensity for irreversible protein aggregations. In order to verify that there was indeed no fibril formation, tau187-RNA CCs were prepared by mixing tau187-SL and RNA (see **Materials and Methods**) and monitored by continuous wave electron paramagnetic resonance spectroscopy (For details of cw-EPR experiments see **Materials and Methods**). The cw-EPR spectra shows no broadening (Figure 2-1C), and the cw-EPR spectra analysis reveals an

unchanged rotational correlation time for the spin label of tau187-SL, τ , of 437 ± 37 ps as a function of time after > 96 hours of incubation at room temperature (Figure 2-1D, turquoise) (**Materials and Methods**). For comparison, cw-EPR spectra and τ were recorded of tau187-SL alone in buffer, and of tau187-SL in the presence of heparin under fibril forming conditions. Tau187-SL alone in buffer showed cw-EPR spectra overlapping with those of tau187-RNA CC, and rotational correlation time τ , 425 ± 16 ps, nearly identical to the τ of tau187-SL CCs (Figure 2-1D, red). In contrast, tau187-SL with heparin shows a significantly broadened cw-EPR spectrum and an increasing τ to 2.3 ± 0.7 ns (Figure 2-1C, D, green). Note that a hundreds of ps range of τ corresponds to rapid tumbling of the spin label, whose rotational degree of freedom is minimally hindered by molecular associations, while a several ns range of τ corresponds to slow tumbling and molecular hindering by association or confinement. The Thioflavin T (ThT) fluorescence curves of the same sample system as a function of time confirms the absence of amyloid aggregate formation in tau187-RNA CCs (Figure S1). These results together suggest that tau187-RNA CCs are in an equilibrium state, in which tau retains its solution-like dynamics.

Next, we investigated the reversibility of tau187-RNA complex coacervation. Tau187-RNA CCs were prepared again and incubated by cyclically ramping the temperatures (1 °C/min) upwards and downwards, while the absorbance at $\lambda = 500$ nm was monitored, referred to as turbidity hereafter. Ramping rates of 0.5 °C/min and 1 °C/min were tested, but the results shown to be indistinguishable. Microscopy images were concurrently acquired at low and high turbidity, confirming the appearance and abundance of CC droplets correlating with turbidity

increase, and *vice versa* (Figure 2-1E). The turbidity-temperature curves show that at high temperature, samples became turbid with $\text{Abs}_{500} \sim 1.5$ and abundance of CCs, while at low temperature, samples became transparent with $\text{Abs}_{500} \sim 0$ and absence of CCs. This demonstrates tau187-RNA CC formation is favored at higher temperature, following clearly a lower critical solution temperature behavior (LCST) (Figure 2-1E) [158]. By cycling the temperature, we robustly and reversibly changed the tau187-RNA mixture between a turbid state to a completely transparent state (Figure 2-1E). The transition temperatures at which the turbidity emerged during heating and vanished during cooling stay invariant with repeated heating-cooling cycles. The method of extracting a cloud point for the LCST transition temperature from such data will be described in detail in the next section. Importantly, the history of temperature change does not affect the resulting state. Hence the formation and dissolution of tau187-RNA CCs are reversible and consistent with a path-independent equilibrium process. We point out that the maximum turbidity value successively decreases with each heating cycle (Figure 2-1E), even though the transition temperatures remain invariant. This can be attributed to slow degradation of RNA with time, (as demonstrated in Figure S2) by verifying an altered turbidity change in the presence of RNase or RNase inhibitor.

It is understood that upon gradual heating of the solution phase, the mechanism of LLPS proceeds via a nucleation process [159], and hence there is a kinetic barrier evidenced by the observed hysteresis in Figure 2-1E. Nonetheless, we conclude that the final tau-RNA CC state

reached upon heating is a true thermodynamic state, and thus can be modeled by an equilibrium theory of phase separation.

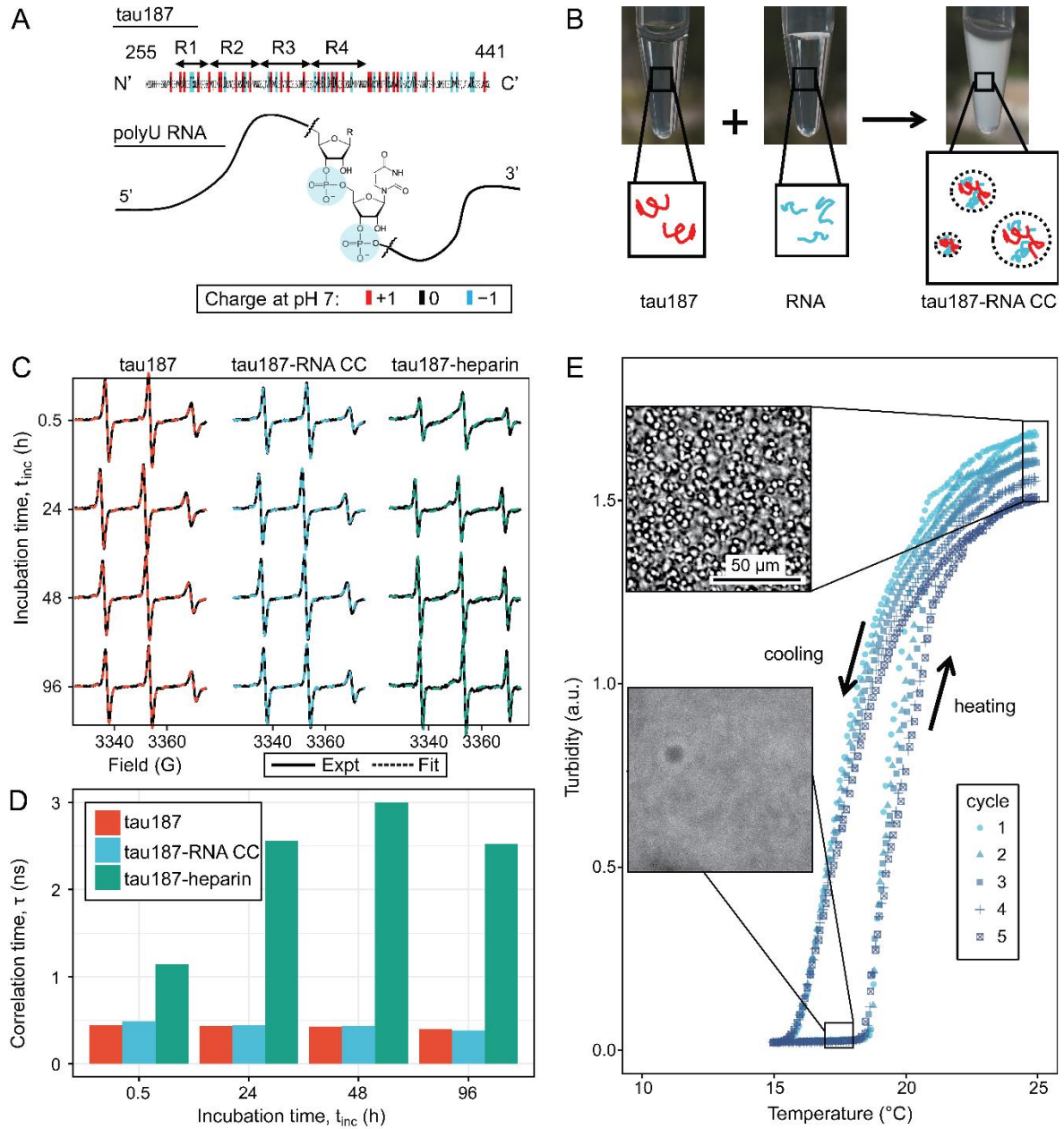


Figure 2-1. Steady tau dynamics and reversible droplet formation of tau-RNA complex coacervates.

A. Diagram of tau187 (tau) and polyU RNA (RNA). Tau187 is a truncated version of full-length human tau (2N4R 255-441) containing repeat domains and C terminal. At neutral pH experimental conditions, tau187 is overall positively charged; while RNA consists of a phosphate backbone and is negatively charged. **B.** Scheme of tau-RNA CC preparation. Mixing clear tau187 and RNA solutions at proper conditions results in a turbid solution containing liquid droplets. **C.** X-band cw-EPR spectra (solid line) of tau187 solution (tau187, red), tau187-RNA CC (blue) and tau187-heparin (green) at room temperature with different incubation time, t_{inc} . Samples contains 500 μ M tau with 20% spin-labelled. EPR simulation were performed (SI Method) and the fitted spectra is shown as a dashed line. **D.** Rotational correlation time, τ_R extracted from EPR simulation shown in (b1) (SI Method). **E.** Turbidity of tau187-RNA suspension in consecutive heating-cooling cycles. Confocal images represented samples at 19 °C and 25 °C. Temperatures were ramped at 1 °C/min.

Tau-RNA complex coacervate phase diagram

To understand the principles and governing interactions driving tau-RNA CC formation, we constructed a phase diagram for tau187-RNA CC by measuring the transition temperature – to be described in greater detail below – as a function of protein concentration and salt concentration. We first recorded tau187-RNA turbidity at various [tau], [RNA] and [NaCl] values, ranging from 2-240 μ M, 6-720 μ g/mL and 30-120 mM, respectively. Titrating RNA to tau187, the turbidity was found to be peaked when [RNA]:[tau] reached charge matching condition at which the charge ratio between net positive and negative charges was 1:1 (which for tau187 and RNA used in this study corresponded to [tau187]:[RNA] = 1 μ M : 3 μ g/mL), validating once more that LLPS is driven by complex coacervation (CC) (Figure S3). Henceforth, all phase diagram data are acquired at a charge matching condition between RNA and tau. Titrating NaCl to tau187-RNA, CC formation showed a steady decrease of turbidity (Figure S3). Combined, these demonstrate that tau187-RNA CC favors the condition of charge balance and low ionic strength, which is consistent with known properties of CC and previous findings [22].

We next investigated the phase separation temperatures under various sample compositions. Tau187-RNA CCs were prepared with a fixed [tau]:[RNA] ratio corresponding to the condition of net charge balance. Therefore, the composition of tau187-RNA CC can be determined by [tau] and [NaCl]. Samples were heated at 1 °C/min between $T = 15\text{-}25\text{ }^{\circ}\text{C}$, while the turbidity was monitored. The turbidity-temperature data of the heating curves were then fit to a sigmoidal function, so that the cloud point temperature, T_{cp} , could be extracted as shown in Figure 2-2A (T_{cp} was determined from heating curves out of practical utility; T_{cp} from cooling curves is possibly closer to thermodynamic transitions). The experimental cloud-point temperature T_{cp} for CC formation as a function of [tau] and [NaCl] are shown (as points) in Figure 2-2B and Figure 2-2C. The experimental data points show that increasing [tau] lowers T_{cp} , favoring CC formation, while increasing [NaCl] raises T_{cp} , disfavoring CC formation. Such trends were observed at two [NaCl] and two [tau] values, respectively (Figure 2-2B, C). Experimentally, T_{cp} was determined for a range of [tau] and [NaCl] conditions (see Figure S4). We point out that there is certain level of variability in the observed T_{cp} , which can result from pH fluctuation of the ammonium acetate buffer upon tau-RNA addition, as well as RNA degradation as demonstrated in Figure S2.

The features of the Tau-RNA CC phase diagram were also investigated by comparing tau187 and tau114. Tau187-RNA CC and tau114-RNA CC were prepared with 20 μM tau187 and 28 μM tau114, so that the total concentration of polymer, i.e. tau and RNA, reaches 0.5 mg/mL. Turbidity was recorded at varying [NaCl]. Similar to the observation with tau187-RNA CC, tau114-RNA CC showed decreasing turbidity at increasing [NaCl] (Figure S5). The

[NaCl] values where turbidity reaches 0 were estimated as 131 mM and 150 mM for tau187 and tau114, respectively, implying CC formation is more favorable with tau114 that hence can sustain higher [NaCl]. Based on this, 20 μ M of tau187, 131 mM of NaCl and room temperature, 20 °C, were used as the phase separation conditions ([tau], [NaCl] and T_{cp}) for tau187, and 28 μ M, 150 mM and 20 °C for tau114. These two experimental conditions were used in the next section for comparing the two constructs of tau.

Flory-Huggins-Voorn-Overbeek Fit to Experimental Phase Diagram

We next used the FH-VO model to fit the experimental data for the tau187-RNA CC system, as is commonly done in LLPS studies. Despite its theoretical deficiencies the FH-VO model is commonly used for its simplicity and ease of implementation. Our system consists of five species: tau187, RNA, monovalent cation (Na^+), anion (Cl^-) and water. For simplicity, we explicitly consider only the effect of excess salt, and do not include polymer counterions. The FH-VO model maps these five species onto a three-dimensional lattice (Figure 2-2D). Each polymer is treated as a uniform chain with degree of polymerization N and average charge per monomer σ . N was taken as the average chain length of the species (1 for monovalent ions). The charge density σ of RNA, monovalent ions and water were set to 1, 1 and 0 respectively. The values for σ of tau187 or tau114 were calculated from the net charge at neutral pH divided by the chain length. The composition of the species is expressed in terms of the volume fraction ϕ of the occupied lattice sites, which are proportional to the molar concentrations (see **Materials and Methods** for details). As in experiments, tau187-RNA CCs were prepared at fixed [tau]:[RNA] and $[\text{Na}^+]:[\text{Cl}^-]$ ratios. Under these two constraints, the volume fraction of

all five species in tau187-RNA CC listed above can be determined with two variables, $[\text{tau}]$ and $[\text{NaCl}]$, which are experimentally measurable.

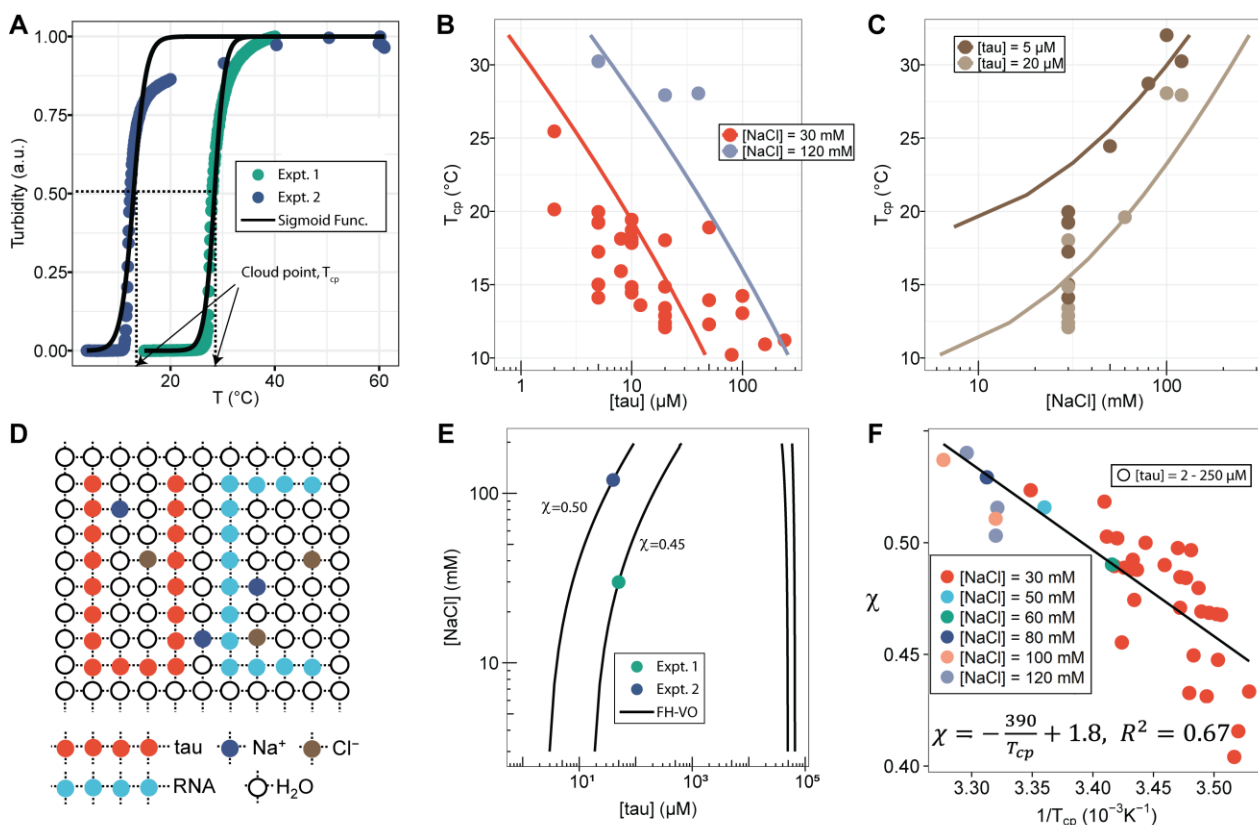


Figure 2-2 FH-VO modeling of tau-RNA CC.

A. Turbidity of tau187-RNA CC upon heating (Expt.1 ($[\text{tau}]$, $[\text{NaCl}]$) = (50 μM, 120 mM), green dots; Expt.2 ($[\text{tau}]$, $[\text{NaCl}]$) = (40 μM, 30 mM), purple dots). Absorbance at $\lambda = 500$ nm were normalized and used as turbidity value. Turbidity-temperature data of the heating curves were fitted with a sigmoidal function (solid line) as described in (SI Method), and the temperature at which normalized turbidity reaches 0.5 was assigned to cloud point, T_{cp} . **B-C.** Experimental phase diagram (points) showing $[\text{tau}]$ vs. T_{cp} and $[\text{NaCl}]$ vs. T_{cp} along with the binodal curve generated from fitting the data to the FH-VO model with $\chi = \chi(T_{cp})$ (solid line) **D.** Diagram of Flory Huggins lattice. Tau and RNA are represented by consecutively occupied lattice sites. **E.** Each experimental condition in (A) was independently fit to the FH-VO model (solid lines) to obtain an empirical χ value. **E** shows two representative curves. These empirically determined values of χ are shown as points in **F**. The solid line in **F** is a linear regression, generating $\chi = \chi(T_{cp})$, which is then used to generate the binodal lines in **B** and **C**.

Given N , σ , $[\text{tau}]$, $[\text{NaCl}]$ and T_{cp} , the task is to find $\phi_{\text{tau}}^{\text{I}}$ and $\phi_{\text{tau}}^{\text{II}}$, the volume fractions of tau in the dilute and dense, coacervate, phase at equilibrium, i.e. the binodal coexistence points. The model and procedure is described in detail in **Materials and Methods**. For each experimental observation of T_{cp} determined for a given $[\text{tau}]$ and $[\text{NaCl}]$ (Figure S4), the FH-VO expression has one unknown parameter, the Flory-Huggins χ term. The Flory-Huggins χ parameter is introduced as an energetic cost to having an adjacent lattice site to a polymer segment occupied by a solvent molecule [65]. Here we take χ to be an adjustable parameter, such that given a suitable expression for χ , the complete binodal curve can be modeled with the FH-VO theory. Consequently, we first solved for χ at each given experimental condition, so that the theoretical binodal curve intersects the experimental data point. Figure 2-2E shows two representative examples of a theoretical binodal curve (solid line) intersecting a single experimental data point at the given $[\text{NaCl}]$ and $[\text{tau}]$. This procedure gives an empirical χ parameter for each experimental data point, as collated in Figure 2-2F as a function of $1/T_{\text{cp}}$. We then performed to this set of experimental data a least-squares fit of the empirical χ parameter to the form $A + B/T$ (Figure 2-2F), yielding an expression of the temperature dependence of χ of

$$\chi(T) = 1.8 - \frac{390}{T}, R^2 = 0.67. \quad (\text{Equation 1})$$

A temperature dependence of χ in the form of Equation 1 (consistent with the observed LCST), can originate from hydrophobic interactions between non-polar groups, whose

interaction strength tends to increase with temperature [160], [161]. This explanation has also been used to describe cold denaturation of proteins [162].

Finally, from this expression for $\chi(T)$, we computed the binodal curves that establishes the phase coexistence as a function of T_{cp} , $[\tau]$ and $[\text{NaCl}]$, shown as solid lines, only for the dilute phase coexistence for T_{cp} vs $[\tau]$ (Figure 2B) and T_{cp} vs $[\text{NaCl}]$ (Figure 2-2C). For the full phase diagram showing both dilute and dense binodal curves see Figure S6. The experimental data (shown as points) and computed binodal curves both exhibited a decreasing T_{cp} with increasing $[\tau]$ and an increasing T_{cp} with increasing $[\text{NaCl}]$. This simply establishes that tau-RNA CC favors higher tau concentrations in the 1-240 μM range and lower ionic strength in the 30-120 mM range tested here.

Binodal curves for tau114-RNA CC were also computed, and are compared with tau187-RNA CC, along with experimental data (Figure S5). Comparison of the two constructs shows that tau114-RNA CC has a lower T_{cp} than tau187-RNA CC, suggesting it is more favorable to phase separation. This qualitatively agrees with experimental observations. Notice that the shorter tau114 has a slightly higher propensity to form CC as compared to the longer tau187 fragment, an observation that is opposite of what one would expect from purely entropic considerations based on the mixing of homopolymers or simple coacervation. One possible explanation could be the increased charge density of tau114 with respect to tau187, indicating the importance of both charge sequence and charge density for the phase diagram. Additional short-ranged sequence-specific interactions between tau114 and RNA that are not present in tau187 is another possibility that is not considered in the present model.

Application to cell-complex coacervate co-culture

Looking at the experimental and calculated phase diagrams (Figure 2-2B, C), it is seen that under physiological conditions ($T_{cp} \sim 37^\circ\text{C}$, $[\text{NaCl}] \sim 100\text{ mM}$) it is principally feasible for cells to tune the formation of tau-RNA CCs. This has important implications for studying the physiological roles of tau-RNA CCs, and thus we asked if tau-RNA CCs could indeed exist in a biologically relevant media in the presence of living cells. Both the FH-VO theory and FTS predict that the conditions of high protein concentration, low ionic strength, high temperature and high crowding reagents (leading to solution conditions with a lower effective excluded volume parameter to model the poorer solvent environment in an implicit solvent model [163]) would independently favor tau-RNA CC formation. Using these tuning parameters as a guide, we designed several experiments to test the ability for tau-RNA CCs to form in a co-culture with H4 neuroglioma cells. We incubated H4 cells with tau187/tau114-RNA under CC conditions at varying temperatures, polymer concentrations and crowding reagent concentrations. At low polymer concentrations ($10\text{ }\mu\text{M}$ tau, $30\text{ }\mu\text{g/ml}$ RNA) no LLPS was observed in the cellular media (Figure 2-3, first column), where increasing the temperature to 37°C did not apparently influence the solution phase (Figure 2-3, first column, first and third row). However, when tau and RNA concentrations were increased ($100\text{ }\mu\text{M}$ tau, $300\text{ }\mu\text{g/ml}$ RNA) LLPS could be observed (Figure 2-3, second column). Further, LLPS could also be achieved by adding an additional crowding reagent (here PEG) to low concentration samples of tau and RNA (Figure 2-3, third column). As predicted, LLPS of tau-RNA CC was modulated by (i) temperature, (ii) tau and RNA concentration and/or (iii) the presence of crowding reagent

PEG (Figure 2-3). Lowering the temperature to 18°C significantly reduced the number and size of fluorescent droplets, demonstrating that tau-RNA LLPS is indeed tunable by temperature, and demonstrate the biological consequence of the LCST behavior (Figure 2-3, first and third row). These results were consistently found for both tau187 and tau114 systems. The successful application of FTS for tuning and predicting tau-RNA CCs in cellular media is a first step towards understanding the physiological condition under which tau-RNA LLPS, which follows the CC mechanism, can occur. Notice that our truncated tau construct has been demonstrated to undergo LLPS at similar conditions ([tau], [RNA], [NaCl] and temperature) compared with full length tau, 2N4R, *in vitro* [22]. The conditions described for LLPS here suggests that conditions exist *in vivo* under which LLPS by complex coacervation may be achieved by biological regulation mechanisms, and under conditions where tau and the LLPS forming constituents are available in the cytoplasm.

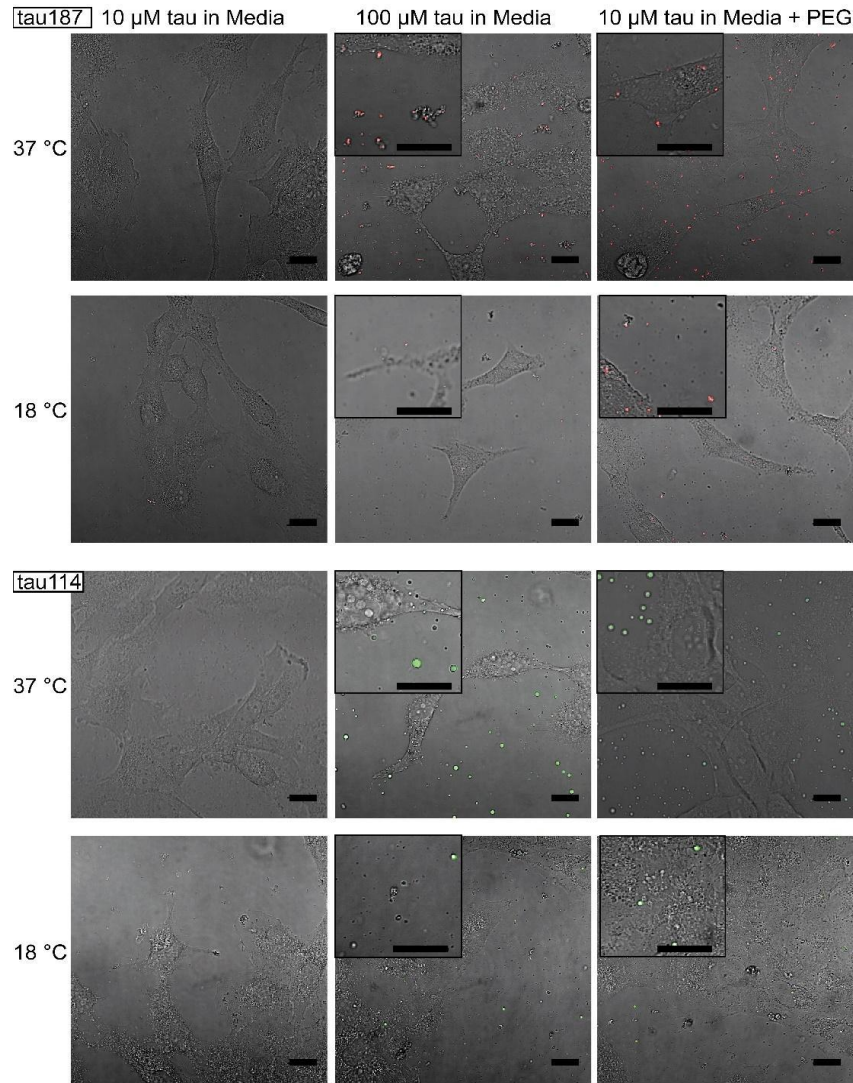


Figure 2-3 Tuning experimental conditions to catch tau-RNA complex coacervates in presence of living cells.

Bright field images and superimposing fluorescence images of tau-RNA CC coculturing with H4 cells, with 10 μM tau (left), 100 μM tau (middle) and 10 μM tau with 10% v.v. PEG (right). Samples at 37 $^{\circ}\text{C}$ (first row) and 18 $^{\circ}\text{C}$ (second row) were images with representative images showing the co-presence of living cells and tau-RNA CCs. Tau187 (Top) and tau114 (Bottom) was used showing tau114 with higher propensity at CC formation. Alexa Fluor 488 was used to prepare fluorescent labeled tau. 3 $\mu\text{g}/\text{mL}$ polyU RNA per 1 μM tau was used to prepared samples. Scale bar is 20 μm .

Discussion

The ability of tau to undergo LLPS via a mechanism of complex coacervation has been recognized in a number of recent publications [121], [124] [22]. However, to date, the criteria and physical parameters (specifically, polymer concentration, ionic strength, temperature and crowding reagents) that drive tau-RNA CC has not been rationalized. In this paper, we mapped out the experimental phase diagram for tau-RNA CC, and used theory and simulation to describe the parameter space for LLPS. In what follows, we discuss the relevance of our findings in the context of the physical mechanism of LLPS *in vivo*.

Although the FH-VO model cannot model spatially varying charges along the peptide backbone, we were able to fit the experimental data by treating the Flory-Huggins χ parameter as an empirical, temperature-dependent, adjustable parameter. This result highlights the fact that the FH-VO model is adaptable to experimental data.

Consider that we can partition the driving forces of CC as

$$\Delta G^{CC} = \underbrace{\Delta H^{tau/RNA}}_{(-)} - \underbrace{T\Delta S^{comb}}_{(-)} + \underbrace{\Delta H^{ex} - T\Delta S^{noncomb}}_{\text{excluded volume or } \chi}$$

where the first two terms are the negative (favorable) enthalpic contribution from tau/RNA interactions and the ideal entropy of mixing term (which is negative because we are considering CC formation). These first two terms are approximately accounted for in the original VO model, and by themselves predict UCST behavior (see SI). The last two terms introduce a non-ionic excess enthalpic contribution and a nonideal, noncombinatoric entropy that are introduced into the FH-VO model through the Flory-Huggins χ parameter, or within FTS through the temperature dependent excluded volume. Given the experimental observation

of LCST phase behavior, these terms must be important and we now estimate their value from our model.

Modeling the LCST experimental tau-RNA CC phase diagram using the FH-VO model by invoking an entropic term in the Flory-Huggins χ parameter, or by FTS using a temperature dependent excluded volume, both provide an estimate of the entropic contribution that drives CC formation. The temperature-dependent excluded volume v used to describe LCST phase behavior within FTS can be formally related to the Flory-Huggins χ parameter to second order in the polymer volume fractions $v = b^3(1 - 2\chi)$ [164]. Substituting our empirical excluded volume, we obtain from FTS an interaction parameter χ of the form $\chi = \epsilon_s + \epsilon_H/T$, with ϵ_s being a non-combinatoric entropic term and ϵ_H an enthalpic term. Introducing conventional units (see **Materials and Methods** for details) gives an unfavorable non-electrostatic enthalpy of phase separation of $\Delta H^{\text{ex}} = 0.23 \text{ kJ} \cdot \text{mol}^{-1}$ of monomer, and a favorable noncombinatoric entropy of phase separation of $T\Delta S^{\text{noncomb}} = 1.1 \text{ kJ} \cdot \text{mol}^{-1}$ of monomer at $T = 300 \text{ K}$. For comparison, the empirical χ from fitting the experimental data with the FH-VO model gives $\Delta H^{\text{ex}} = 2.3 \text{ kJ} \cdot \text{mol}^{-1}$ of monomer and $T\Delta S^{\text{noncomb}} = 3.24 \text{ kJ} \cdot \text{mol}^{-1}$ of monomer.

Notably, ΔH^{ex} is small and positive. We hypothesize that the positive, i.e. nonionic, enthalpy value for forming a coacervate phase is due to the requirement of breaking favorable interactions between hydrophilic residues and water that stabilizes the solution phase of tau ($\Delta H^{\text{ex}} = -\Delta H^{\text{tau/water}}$). For comparison, the enthalpy of forming a hydrogen bond ΔH_{HB} at room temperature is $\sim -8 \text{ kJ} \cdot \text{mol}^{-1}$ [165] while the enthalpy of hydration for a polar amino acid ΔH_{hyd} is $\sim -60 \text{ kJ} \cdot \text{mol}^{-1}$ [166], [167]. Given that $\Delta H^{\text{tau/RNA}}$ for tau-RNA association is

negative and tau remains hydrated in the CC state (i.e. tau-water interface is not dehydrated), there has to be a source of penalty in the form of a positive ΔH^{ex} value; the unfavorable ΔH^{ex} associated with tau-RNA CC might come from the loss of hydrogen bonds in the hydration shell from overlapping and sharing of the tau hydration shells in the dense CC phase.

The $T\Delta S^{\text{noncomb}}$ value is also small, positive and of comparable magnitude as ΔH^{ex} , making temperature increase a facile modulator favoring tau-RNA CC. Given the positive value of ΔH^{ex} for tau-RNA CC, the entropy gain upon phase separation is contributing to the driving force of tau-RNA CC formation (besides the electrostatic correlation energy between the polycationic and polyanionic polymer segments that is the major driving force). Looking to potential origins for positive $T\Delta S^{\text{noncomb}}$, we consider the entropy gain of breaking a hydrogen bond of $T\Delta S_{\text{HB}} \sim 6 \text{ kJ} \cdot \text{mol}^{-1}$ [165] and the entropy gain associated with the release of a single water molecule from a hydrated surface of $\sim 7.5 \text{ kJ} \cdot \text{mol}^{-1}$ [168]. Given that our FTS study only considered excess ions, but no counterions, while fully capturing the LCST behavior through the excluded volume, v , our results are consistent with the hypothesis that competing hydrophilic/hydrophobic interactions are responsible for the LCST behavior [169]–[171]. At low temperatures, the attractive interaction between water and hydrophilic residues of the biopolymer stabilize the homogenous phase, but above a critical temperature hydrophobic interactions become dominant, in that it becomes more favorable for water to be released from the polymer surface and hydration shell, and for tau and RNA to associate. In this scenario, the entropy gain comes from the release of bound water into the bulk [70] due to overlapping of the hydration shell of tau upon CC. In the literature, the entropy gain of counter ion release

[172]–[175] or compressibility effects [176], [177] have been proposed as origins for the LCST behavior, and as prevalent driving forces for CC [178]. While this study cannot entirely delineate between these possible contributions that are all subsumed into the Flory-Huggins χ parameter or the excluded volume parameter in FTS, we demonstrate that it is not necessary to invoke a specific mechanism, such as counter ion release—the most popular hypothesis, to rationalize LCST driven CC formation. In fact, we performed FTS studies with (and without) explicit excess ions observing LCST behavior simply by means of excluded volume and electrostatic considerations and not invoking any counter ion release mechanism to capture the phase diagram of the entropy driven tau-RNA CC. Instead, many factors that globally modulate the excluded volume effects in the biological system of interest and that inevitably modulate the hydration water population, including the hydrophobic effect and crowding, may be considered.

We demonstrated here that tau-RNA CC can be modeled as a coarse-grained polyelectrolyte mixture using equilibrium theory, and revealed the associated driving factors and the different thermodynamic contributions to the phase diagram. However, this finding does not contradict the possibility that tau-RNA complex coacervation is followed by, or even can facilitate, amyloid fibrillization of tau. Comparing our study to previous reports in the literature [22], [48], [121], [122], [124], [179], it is clear that tau in fibrils possess dramatically different properties than tau in CCs. In contrast to fibrils, tau-RNA CCs are reversible and tau remains conformationally dynamic – this is because CCs are formed with a stable tau variant, such as the WT derived tau studied here. However, once aggregation-promoting factors are

introduced, not only can the thermodynamically stable phase of tau-RNA CC be driven out of equilibrium, but the dense CC phase harboring high tau and RNA concentration may also lower the activation barrier for, and thus facilitate, tau aggregation. Still, tau complex coacervation is a distinct state and fibrilization is a distinct process, where the equilibrium of one does not contradict with its kinetic transformation into the other. Recently, the possibility of the transformation of tau CCs into tau fibrils has been demonstrated [121]. We have independently investigated these questions and find that irreversible transformation can be triggered by doping tau-RNA CC with highly sulfated polysaccharide heparin (Figure S6). Tau is first driven towards an equilibrium complex coacervate state, from which tau can either re-dissolve into solution state reversibly, or form amyloid fibrils when aggregation driving force is present. However, the mechanism by which the CC state of tau influences the rate of aggregation and/or alters the aggregation propensity of tau is not understood, and will and should be the subject of future studies.

The physiological role of tau-RNA CC as a possible regulatory mechanism or as an intermediate toward fibrilization is an ongoing topic of research. In either case, for tau-RNA CC to be relevant for cellular function LLPS would have to be possible near (certain) physiological conditions. Our *in vitro* experiments found the tau-RNA CC phase diagram boundary to lie near physiological conditions. This suggests that tau-RNA CC can occur *in vivo* upon modulation of parameters, such as the local temperature, electrostatic balance, including local pH, and osmotic pressure. We demonstrate that indeed tau-RNA CC can be achieved in co-culture with living cells. While the coexistence of tau and RNA at low (10 μ M)

polymer concentrations is not sufficient to drive CC in cellular media, the addition of a molecular crowding reagent is, under physiological conditions (Figure 2-3). While in this study crowding has been simulated with PEG, many cellular proteins can act as molecular crowding reagents. This data encourages us to speculate that mechanisms that increase the already high concentrations of free proteins and other macromolecular constituents, *not* participating in CC, beyond the normal level within the cell (estimates of 50-200 mg/mL [180]) could be sufficient to promote tau-RNA CC by exerting crowding pressure. Thus, biological mechanisms that increase the concentration of intrinsically disordered and charged proteins and nucleic acids may be potent factors that drive liquid-liquid phase separation in the cellular context. Specifically for the context of this study, high concentrations of tau-RNA are by themselves sufficient to drive CC formation (Figure 2-3). Given that tau is known to bind and localize to microtubules in the axons of neurons, it is not a stretch to envision a scenario where the local concentration of tau would be highly elevated under certain stress conditions, around regions like the axon initial segment. We proposed at these places in neuron, tau-RNA CCs have a higher probability to be observed. However, even though our calculations and experimental data support a model where tau-RNA CC *in vivo* is possible, whether this actually occurs within the cell depends on many other factors, among them the strength of tau-microtubule binding that compete with tau-RNA CC.

Conclusion

We report here the first detailed picture of the thermodynamics of tau-RNA complex coacervation. The observation of an LCST phase diagram implies that although electrostatic

interactions are key to CC formation, factors that contribute to solvation entropy gain are key to driving liquid-liquid phase separation. We have computed the first approximation-free theoretical phase diagram for tau-RNA complex coacervation from FTS, where we introduced a temperature-dependent excluded volume term. Simulations show a competition between electrostatic strength (parameterized by the salt concentration) and excluded volume (parameterized by the solvent quality). This knowledge can be used to design experiments that perturb this parameter space *in vivo*, as well as predict or understand biological mechanisms that may be favorable towards liquid-liquid phase separation. As a proof of this concept we have shown that by deliberately changing salt concentration, temperature, and solvent quality (by the addition of PEG), we can make tau-RNA LLPS appear or disappear in cellular medium with *live* cells. Interestingly, we find that without any adjustable parameters our simulations predict that tau-RNA is positioned near the binodal phase boundary around physiological conditions. This suggests that small and subtle changes within the cellular environment may be sufficient to induce LLPS in otherwise healthy neurons. Even if the conditions that induce LLPS in the cell is transient, the LLPS state can facilitate irreversible protein aggregation if aggregation-promoting factors are already available, giving credence to the idea that LLPS may play a role in neurodegenerative diseases. However, we speculate that LLPS is reversible in the majority of biological events that drive LLPS, making it hard to observe this state within the cellular context.

Figure S1

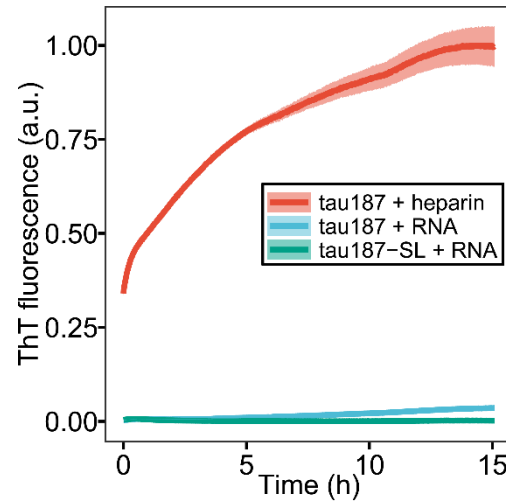


Figure S1 ThT fluorescence of tau-RNA CC. 100 μ M of tau187 and tau187-SL was mixed with 300 μ g/mL polyU RNA (RNA) at room temperature. 100 μ M tau187 with 25 μ M heparin was prepared as reference. Ribbon shows the standard deviation of 3 replicates.

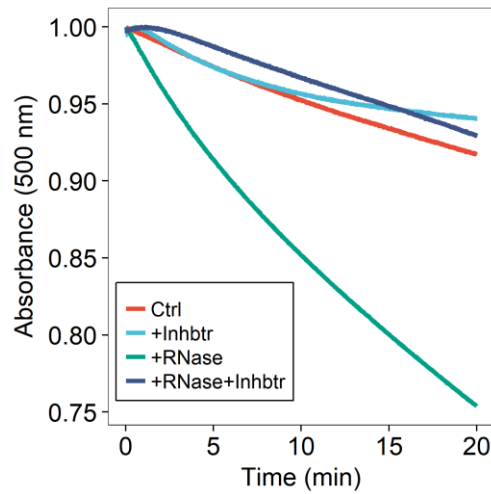


Figure S2. RNase induces turbidity decrease of tau187-RNA CC suspension. Tau187-RNA CCs were re-prepared with 100 μ M tau187C291S and 300 μ g/mL polyU RNA, while absorbance at 500 nm was monitored. Samples were treated with buffer (Ctrl), 1 U/ μ L RNase inhibitor (mainly inhibiting RNase A), 50 ng/mL RNase A, and 50 ng/mL RNase A with 1 U/ μ L RNase inhibitor.

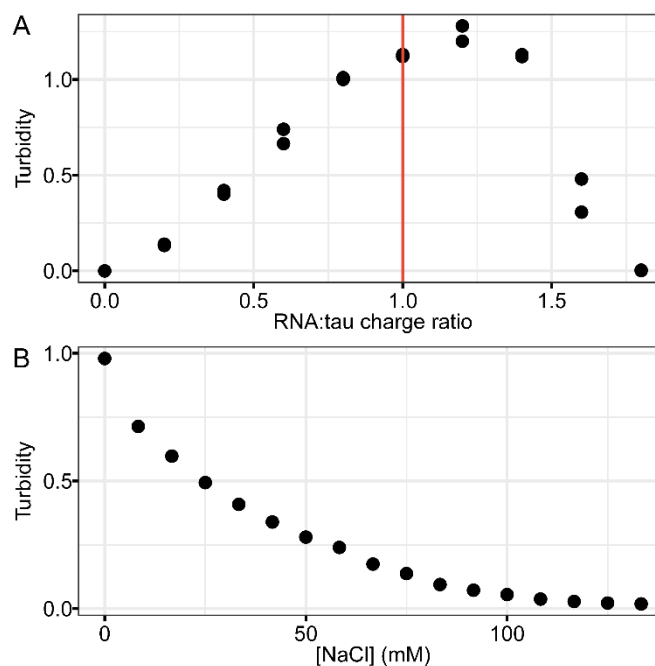


Figure S3. Turbidity of tau-RNA CC at varying charge ratios and ionic strength. (A) PolyU RNA was titrated into 20 μ M tau187C291S in the buffer of 20 mM ammonium acetate at pH 7. Charge ratio was calculated based on the estimated charge for tau, +11 per tau molecule and the estimated charge for RNA, -1 per nucleotide. Turbidity was assigned from absorbance at $\lambda = 500$ nm. Red line indicates the place where the estimated RNA:tau charge ratio equals to 1. (B) 20 μ M tau was mixed with 60 μ g/mL RNA so that RNA:tau charge ratio equals to 1. NaCl was titrated into the mixture while turbidity was monitored.

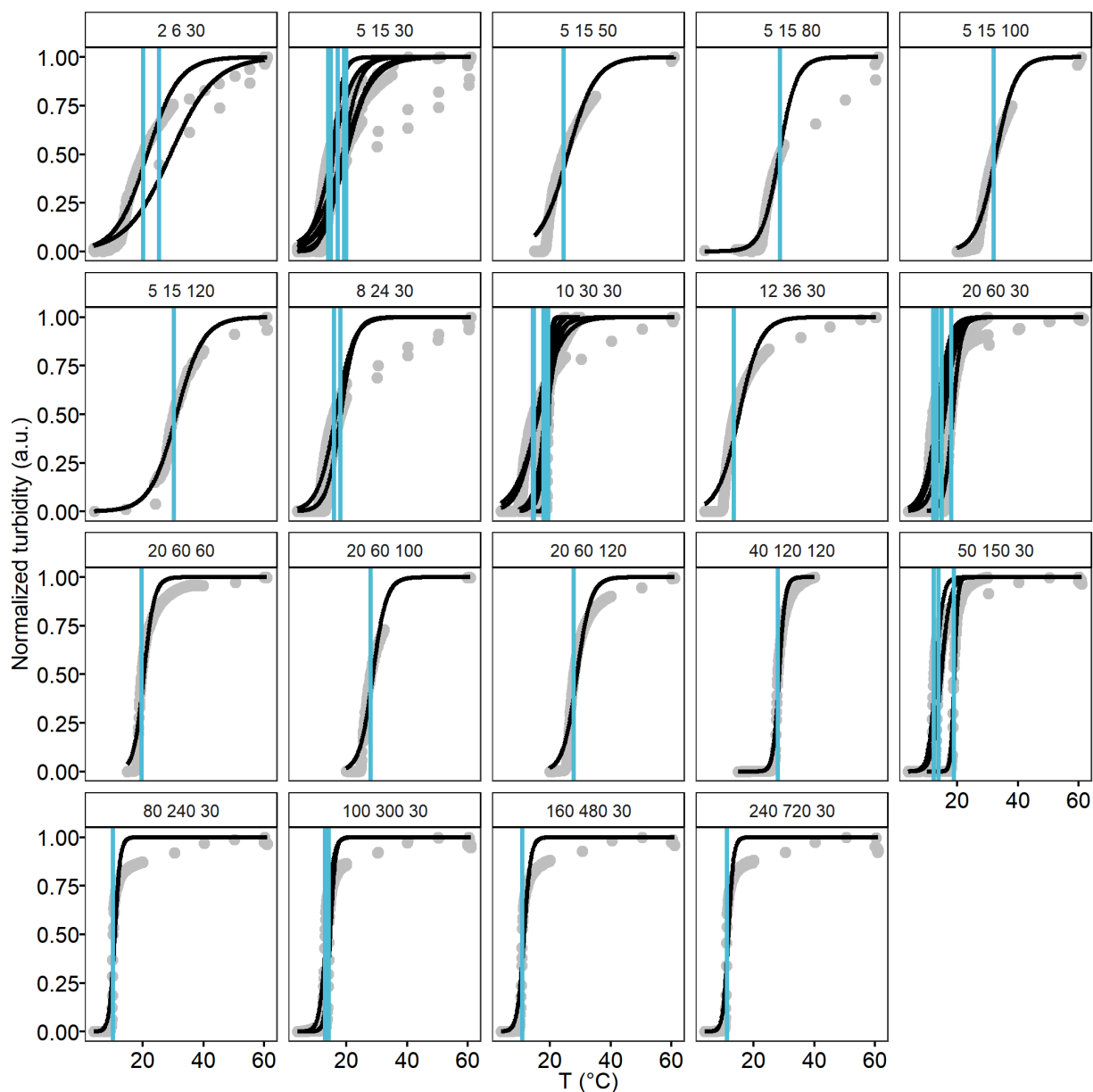


Figure S4 Turbidity-temperature data and cloud points determinations of various $[\tau]$ and $[NaCl]$. Tau187-RNA CCs were prepared at various concentration of $[\tau]$ and $[NaCl]$ with fixed ratio of $[RNA]:[\tau]$, shown as strip text (e.g. “2 6 30” refers to $[\tau] = 2 \mu M$, $[RNA] = 6 \mu g/mL$, $[NaCl] = 30 mM$). Samples were kept at 4 °C before ramping up temperature at 1 °C/min. Absorbance at 500 nm was monitored and used as turbidity (grey points). Turbidity-temperature data were fit to a sigmoid curve (black solid line), where the

cloud point, T_{cp} , were determined (blue vertical line). $[\tau]$, $[\text{NaCl}]$ and T_{cp} were used for theory and simulation modeling.

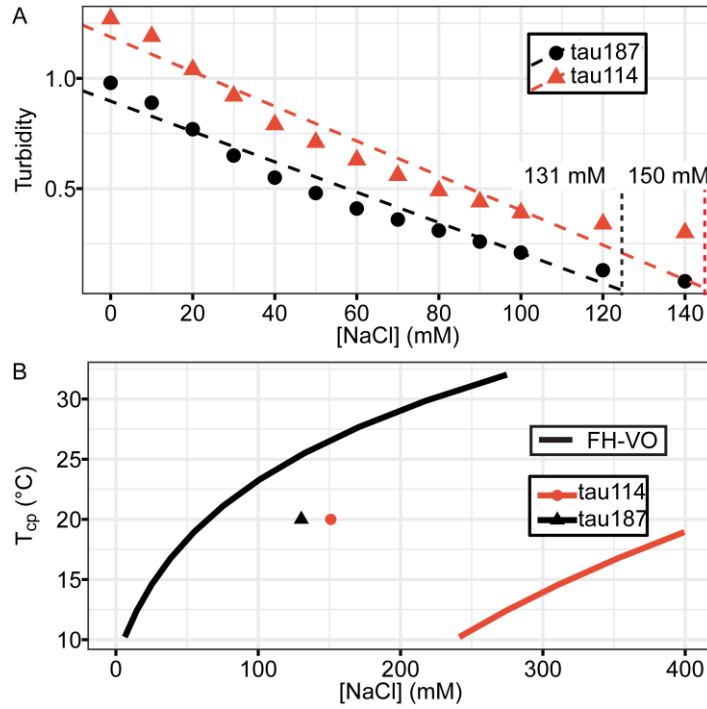


Figure S5 Phase diagrams of tau114 vs tau187. Tau-RNA CC were prepared with 20 μM tau187 with 60 $\mu\text{g/mL}$ RNA (tau187) or 28 μM tau114 with 84 $\mu\text{g/mL}$ RNA (tau114). **(A)** Turbidity was recorded with varying NaCl concentration. $[\text{NaCl}]$ where turbidity vanished were determined by linear fitting to be 131 mM for tau187 and 150 mM for tau114. **(B)** $[\text{NaCl}]$ vs. T_{cp} vs. $[\text{NaCl}]$ curves for 20 μM tau187 or 28 μM tau114 were computed by FH-VO with $\chi = \chi(T_{cp})$ obtained from Figure 2-2D, shown together with the experimental data points obtained from (A).

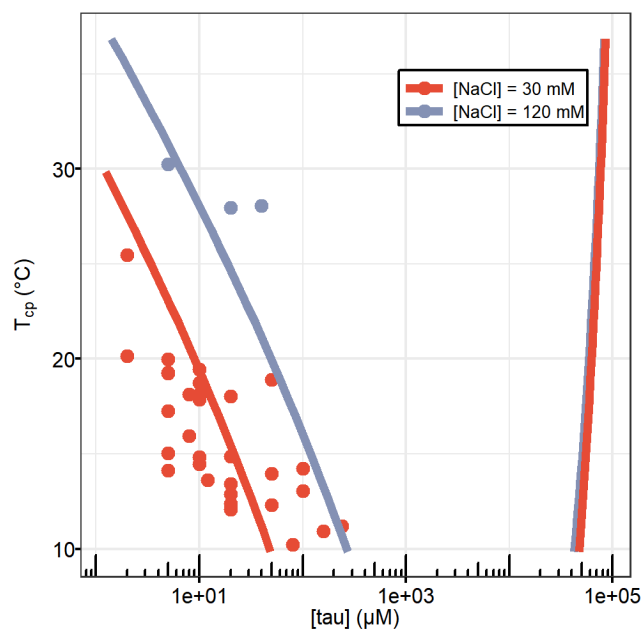


Figure S6 Full phase diagram of tau187-RNA CC. Experimental data showing $[\tau]$ vs T_{cp} was replot from Fig 2B (points). Binodal curves was generated by fitting the data to the FH-VO model (solid lines).

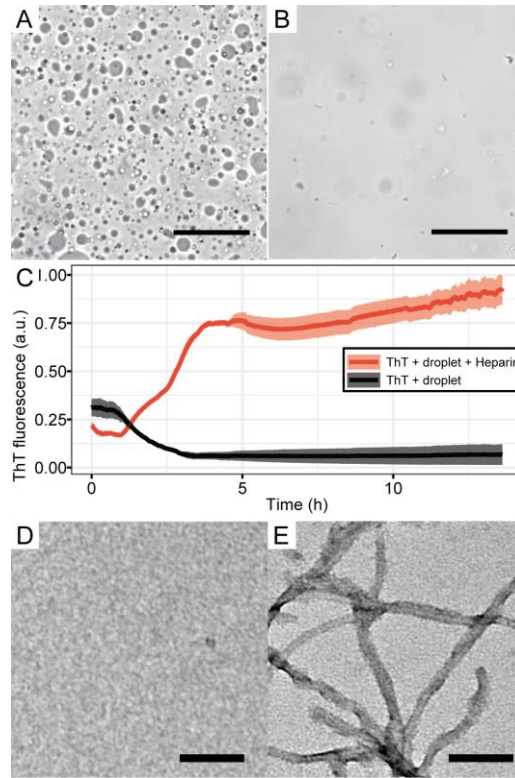


Figure S9 Tau-RNA CC upon addition of heparin. (A) 100 μ M tau187C291S-SL and 300 μ g/mL polyA RNA was mixed in the buffer of 20 mM ammonium acetate at pH 7, with 19 vol % glycerol. Images were taken after 10 minutes at room temperature. (B) Sample in A was re-prepared and incubated for 10 min. 25 μ M heparin was added afterwards, immediately followed by imaging. The scale bars in both A and B are 50 μ m long. (C) ThT fluorescences of samples in A and B were monitored with additional 10 μ M ThT. (D) TEM images of sample in A after overnight incubation, showing no structures similar to amyloid fibrils. (E) TEM images of sample in B after overnight incubation, showing structures with length and width consistent with tau fibrils. The scale bars in both D and E are 200 nm long.

tau	sequence	length
tau187	MGSSH HHHHH SSGLV PRGSH MVKSK IGSTE	207
	NLKHQ PGGGK VQIIN KKLDL SNVQS KSGSK	
	DNIKH VPGGG SVQIV YKPVD LSKVT SKCGS	
	LGNIH HKPGG GQVEV KSEKL DFKDR VQSKI	
	GSLDN ITHVP GGGNK KIETH KLTFR ENAKA	
	KTDHG AEIVY KSPVV SGDTs PRHLS NVSST	
	GSIDM VDSPQ LATLA DEVSA SLAKQ GL	
tau114	MGSSH HHHHH SSGLV PRGSH MVKSK IGSTE	134
	NLKHQ PGGGK VQIIN KKLDL SNVQS KSGSK	
	DNIKH VPGGG SVQIV YKPVD LSKVT SKCGS	
	LGNIH HKPGG GQVEV KSEKL DFKDR VQSKI	
	GSLDN ITHVP GGGN	

Table S1. Primary sequences of tau187 and tau114 used in the experiments and VO-FH calculation.

species	N	net charge	σ
tau187	207	+11.0	+0.053
tau114	134	+10.7	+0.075
RNA	2939	-2939	-1
Na ⁺	1	+1	+1
Cl ⁻	1	-1	-1
water	1	0	0

Table S2. Degree of polymerization and average charge densities of species used in the VO-FH calculation. N, degree of polymerization; net charge, estimated net charge per molecule; σ , average charge per monomer.

T (K)	α	VO-FH		FTS	
		ϵ_H/T	ϵ_S	ϵ_H/T	ϵ_S
300	3.97	-1.3	1.8	-0.370	0.876

total salt (mM)	$\phi_{\text{tau}} + \phi_{\text{RNA}}$	ϕ_{water}	$\Delta H_{\text{D-H}}$ (kJ • mol ⁻¹) per lattice site	ΔH (kJ • mol ⁻¹) per tau monomer	T ΔS (kJ • mol ⁻¹) per tau monomer
50	0.283	0.716	-0.050	-2.321	-3.214
100	0.277	0.722	-0.051	-2.339	-3.239
150	0.271	0.727	-0.051	-2.356	-3.262
200	0.265	0.732	-0.052	-2.372	-3.284

Table S3. Thermodynamics calculated by VO-FH at 300 K and physiological relevant salt concentrations. T = 300 K was used to determine α , ϵ_H/T and ϵ_S . At this temperature, 50 mM ~ 200 mM total salt concentration was used to calculate binodal compositions as described in SI Methods. The calculated composition of tau, RNA and water in the dense phase was listed as $\phi_{\text{tau}} + \phi_{\text{RNA}}$ and ϕ_{water} . $\Delta H_{\text{D-H}}$, the Debye-Huckel approximated phase separation enthalpy; ΔH , the Flory-Huggins phase separation enthalpy and T ΔS , the Flory-Huggins phase separation entropy.

Chapter 3.

Electrostatically Driven Complex Coacervation and Aggregation

Material presented in this chapter is reprinted with permission from Lin, Yanxian, Yann Fichou, Zhikai Zeng, Nicole Y. Hu, and Songi Han. “Electrostatically Driven Complex Coacervation and Amyloid Aggregation of Tau Are Independent Processes with Overlapping Conditions.” ACS Chemical Neuroscience, January 23, 2020. Copyright 2020, American Chemical Society.

Introduction

LLPS has been found to be essential for multiple cellular functions for the last 10 years [10], [12], [181]–[184]. However, its association with amyloid aggregation has only recently become a focus [11], [13]–[15], [185], with the phenomenon of LLPS of tau discovered very recently [22], [121]–[124], [186], [187]. We have so far established that tau-RNA LLPS follows complex coacervation (LLPS-CC) under a range of polymer concentration, temperature, ionic strength and stoichiometry between RNA and tau [22], and we have further mapped out the tau-RNA LLPS-CC phase diagram by experiment, Flory Huggins-based theory and field-theoretic simulation. The phase diagram revealed a narrow equilibrium window near cellular conditions, demonstrating that cells can readily access conditions to assemble and dissolve tau-RNA LLPS *in vivo* [186]. Meanwhile, Ambadipudi *et al.* in 2017 [121] and Wegmann *et al.* in 2018 [124] reported that tau can also undergo LLPS without RNA or other reactants under physiological conditions, hence in a simple coacervation (SC) process. In these studies, the conditions for LLPS-SC coincided with those for amyloid aggregation, and therefore LLPS was postulated to mediate and facilitate aggregation. Despite the observation that tau LLPS and amyloid formation occur in sequential order, it is not clear whether LLPS facilitates aggregation of tau, or if both processes occur independently, but merely have overlapping conditions. Using cofactor-driven tau aggregation as a model system, this study sets out to unravel whether LLPS-CC facilitates the aggregation of tau and *vice versa*, as well as present experimental protocols to interrogate this question.

Tau amyloid aggregation colocalizes with the dense phase of LLPS-CC

We used truncated variants of the longest human tau isoform, 2N4R, that contains four repeat domains (R1 to R4) and the entire C-terminal region (residues 255-441, named tau187 here [156]) to study tau-polyanion liquid-liquid phase separation by complex coacervation (LLPS-CC) and amyloid aggregation. Four variants of tau187 were used in this work, as listed in (Table 1) and summarized here: 1) tauS: tau187 with C291S mutation; 2) tauSS: tau187 with C291S and C322S mutations; 3) tauSP301L: tauS with additional P301L mutation; 4) tauSSP301L: tauSS with additional P301L mutation. At neutral pH, all four variants are positively charged with an estimated +11 net charge per tau molecule, while full length 2N4R tau is estimated to have a +3 net positive charge per tau molecule (Table 1).

Tau has been reported to undergo LLPS-CC with RNA under certain conditions. However, whether this process is driven by tau-RNA specific association or is general to tau-polyanion has not been explicitly tested. To answer this question, tauS was mixed with various polyanions: poly(A) RNA, poly(dA) DNA, heparin and hyaluronic acid (Table 2). The concentrations were chosen so that polyanion and tau reach approximately charge neutrality, i.e., a charge ratio, R , of polyanion:tau is ~ 1 . Immediately after mixing, the clear solution became turbid within seconds, and when imaged under bright field microscope, liquid condensates were visible (Figure 3-1A). They are characterized by clear round boundaries and dynamic fusion with each other. Hence, we refer to these as droplets. Despite having completely different backbone and charged group chemistry, all tested polyanions induced droplet formation upon mixing with tau, suggesting LLPS-CC can be formed relatively

independent of chemical identity, as long as charge matching with multivalent polyanions can be achieved.

We incubated tauSS with heparin at a mixture that achieves net charge neutrality. Confocal microscopy showed that droplets emerged and are retained after 16 hours immediately after mixing (Figure 3-1B), as well as verified the localization of amyloid aggregates within the droplet phase. All droplets showed strong fluorescence of ThT, with the fluorescence intensity increasing after overnight incubation. Transmission electron microscopy (TEM) images confirmed the presence of tau amyloid fibrils (Figure S11A). Both replicas performed at room temperature and with 2N4R full length tau and heparin consistently showed colocalization of ThT fluorescence within droplets (Figure S1, Figure S9B). These results demonstrated that tau can undergo amyloid aggregation under conditions coinciding with that for LLPS-CC, and that the resulting amyloid aggregates colocalize within the dense droplets.

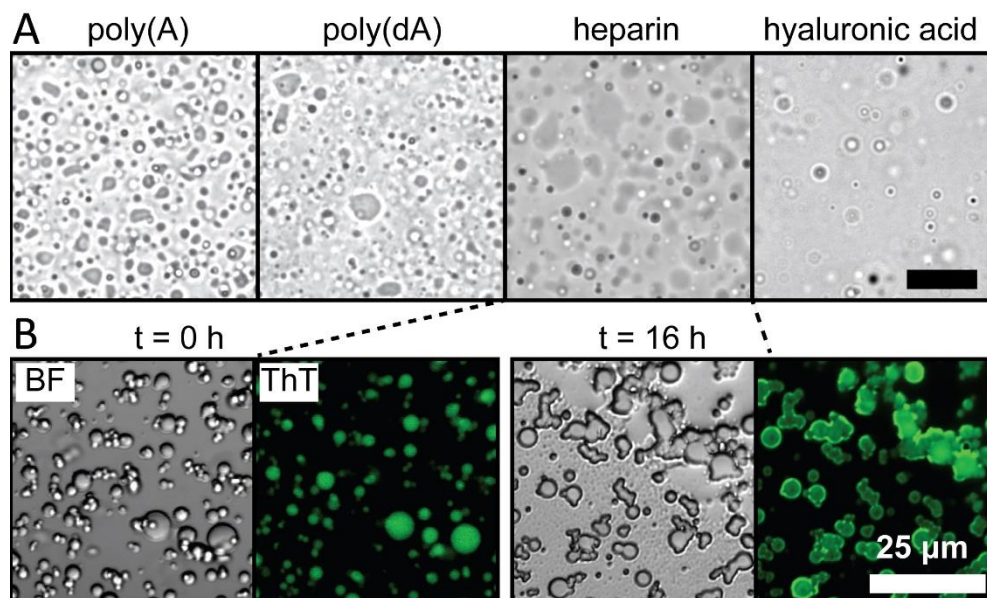


Figure 3-1. Bright field and confocal microscope images of tau-polyanion LLPS and amyloid aggregation.

A. 100 μM tauS was mixed with 300 $\mu\text{g/mL}$ poly(A) RNA, 300 $\mu\text{g/mL}$ poly(dA) DNA, 170 $\mu\text{g/mL}$ heparin, 440 $\mu\text{g/mL}$ hyaluronic acid, respectively. Images were taken at room temperature. **B.** Confocal images of tau-heparin LLPS. 100 μM tauS was incubated with 170 $\mu\text{g/mL}$ heparin and 10 μM ThT at 37 $^{\circ}\text{C}$ for 16 h. Confocal images of both bright field (BF) and fluorescence of ThT ($\lambda_{\text{emission}}=485\text{ nm}$) were taken immediately after mixing ($t = 0\text{ h}$), and 16 hours after incubation ($t = 16\text{ h}$). Scale bars in both A and B are 25 μm long.

The extent of amyloid aggregation is independent of LLPS-CC

Despite the observation that amyloid aggregates colocalized within tau droplets, it is not clear whether this is simply because tau is present inside the droplets, or LLPS-CC facilitates aggregation, for instance, through favorable local physical/chemical properties. In the following three sections, we explore whether or not the LLPS-CC state changes tau

conformation before aggregation, changes kinetics during aggregation and alters the extent of amyloid fibril formation. We present these questions in reverse order, by first asking whether LLPS-CC influences the quantity of tau fibrils formed.

Here, we used turbidity reading at $\lambda = 500$ nm to estimate the volume fraction of phase separated droplets and maximum ThT fluorescence to estimate the relative amount of amyloid aggregates. The turbidity reading was calibrated with model polyelectrolytes and shown to linearly correlate with the volume fraction of LLPS-CC droplets (Figure S10), while ThT fluorescence in both droplet and non-droplet conditions was confirmed to correlate with the presence of amyloid fibrils according to TEM imaging (Figure S11), and to tightly correlate with the amount of fibrillar tau aggregates according to Blue Native PAGE (Figure S8). To avoid interference and to control background noise, the turbidity was read at $t < 1$ h where ThT fluorescence is below 10% (Figure S3), while the maximum ThT fluorescence was extracted from fitting a sigmoidal curve to the aggregation kinetic data (see Materials and Methods).

We first investigated the phase behavior of tau-heparin LLPS, by titrating heparin against tauS, and monitoring the turbidity reading. The results showed that the turbidity peaks at a charge ratio $R = 1$ of heparin:tau (Figure S2A). At such a condition we prepared another sample and varied the NaCl concentration and monitored the turbidity reading. The results showed that the turbidity steadily decreased with increasing [NaCl] to a baseline value at [NaCl] exceeding 40 mM (Figure S2B). The systematic effect of ionic strength in modulating intermolecular association is a signature of polyelectrolyte complex coacervation—the mechanism identified for the LLPS of tau and RNA [186].

We next compared LLPS and amyloid aggregation of tau-heparin at varying stoichiometry and ionic strength. We incubated 20 μM of tauSS with heparin at room temperature at neutral pH overnight on a microplate. We varied $[\text{NaCl}]$ from 0 to 320 mM on each column and varied $[\text{heparin}]$ from $R = 0$ to $R = 16$ on each row. Conditions were carefully chosen to be near physiological conditions (pH ~ 7.4 , ionic strength ~ 100 mM and tau ~ 1 μM). Turbidity and ThT fluorescence of each sample were monitored (Figure S3). Both turbidity and maximum ThT fluorescence were scaled 0 to 1, and presented in a scatter plot side by side (Figure 3-2). A bivariate normal distribution was fitted and shown as red contour (see **Materials and Methods**), indicating the condition preferring amyloid aggregation and/or LLPS-CC. The results showed that amyloid aggregation occurs at a much broader range of $[\text{NaCl}]$ and $[\text{heparin}]$, while LLPS-CC occurs at a small subset of these conditions (Figure 3-2 and Figure S3). The fitting results showed that the maximum position for amyloid aggregation is distinct from that for LLPS-CC, showing optimal LLPS-CC is neither necessary nor sufficient to achieve optimal amyloid aggregation. To answer whether this observation is limited to cysteine-free tau, we repeated it using tauS-heparin under non-reducing condition to encourage disulfide bonding. The results showed again that amyloid aggregation occurs under a broader range of $[\text{NaCl}]$ and $[\text{heparin}]$ at different optimal stoichiometry (Figure S4). Repeated experiments using full length tau 2N4R and heparin showed again a broader range of $[\text{NaCl}]$ for amyloid aggregation compared with LLPS-CC (Figure S9), suggesting such independence

is not specific to tau187 but general to tau. We can conclude that the extent of amyloid aggregation is independent of LLPS-CC of tau and heparin.

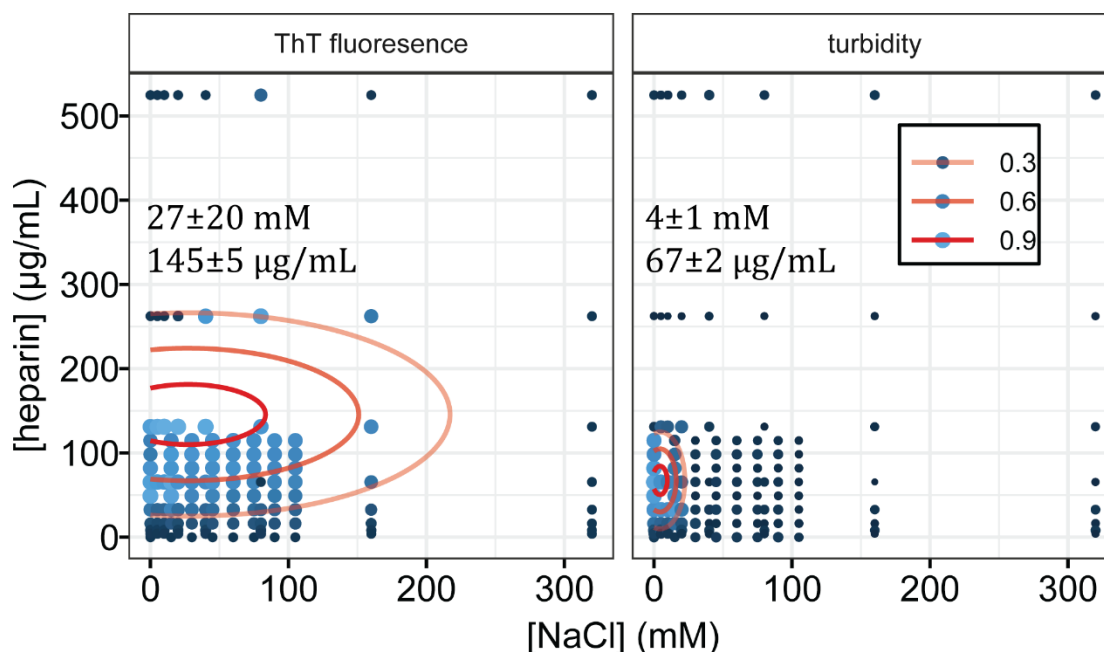


Figure 3-2. LLPS and amyloid aggregation of tau-heparin at varying [NaCl] and [heparin].

20 μM of tauSS was incubated with heparin at varying [heparin] from 0 to 544 $\mu\text{g/mL}$ and [NaCl] from 0 to 320 mM. Turbidity and ThT fluorescence of each sample were monitored and the maximum readings were extracted. Both the maximum turbidity and maximum ThT fluorescence across all the samples were normalized to scale of 0~1. The size and color of data points showed the normalized values. Data points come from three independent replicates using different batches of proteins. Three red solid contour lines from outward to inward showed the fitted bivariate normal distribution at 0.3, 0.6 and 0.9 respectively. Average and standard error of the optimal conditions were listed.

Half time and monomer dependence of amyloid aggregation are independent of LLPS-CC

LLPS-CC results in the formation of concentrated and viscous droplets of tau and polyanions. As high protein concentration tends to accelerate aggregation, while high viscosity tends to decelerate assembly, it is not immediately obvious whether aggregation of tau in droplets will slow down or speed up in the LLPS state. TauSS-heparin droplets were prepared and mixed with varying [NaCl] and ThT fluorescence and turbidity reading were analyzed. The turbidity readings of samples were normalized to 1. For qualitative estimation, we regarded conditions where turbidity falls above 0.3 as droplet conditions, and below 0.3 as non-droplet conditions. To quantify the kinetics of tau aggregation, we used the time when ThT fluorescence reading reaches half maximum, referred to as half time or $t_{1/2}$ (see Materials and Methods).

We first investigated $t_{1/2}$ while keeping [heparin] at $R = 1$ and $R = 3$ (Figure 3-3A). Results showed that overall $t_{1/2}$ increases with increasing [NaCl], regardless of [heparin]. Importantly, near the phase separation boundary, the $t_{1/2}$ value under droplet condition was not significantly different compared to the non-droplet condition (Figure 3-3A). Independent repeats of the same conditions in (Figure 3-3A) showed similar results (Figure S5B). Meanwhile, the dependence of $t_{1/2}$ on [heparin] from $R = 0.5$ to $R = 4$ was also investigated and shown to be independent of LLPS-CC formation (Figure 3-3B).

The aggregation kinetics of many amyloid-forming proteins, including insulin [188], A β [189], as well as tau [190]–[192], have been modeled by a nucleation-elongation process, in which fibrils form through sequential addition of monomers to the nucleus [193]. The slope of the log-log plot of half time vs initial monomer concentration, denoted scaling exponent γ , has been used to identify the dominant microscopic process in the overall reaction [194]–[196]. A value for this slope $\gamma = 0$ implies a completely saturated dominant process [192], [194], meaning the rate of fibril formation is limited by the interaction between the monomer and the interface of the nucleus, and the monomer concentration is so high that the interface is fully occupied, resulting in an apparent independence of $t_{1/2}$ on monomer concentration. Meanwhile, $-0.5 < \gamma < 0$ implies reduced saturation and a recovery of the monomer dependence [194]. Here, we adopted the nucleation-elongation model for tau aggregation and utilized γ to quantify the effects of LLPS-CC on the monomer dependence of aggregation. We varied the initial monomer concentration of tau, $[\text{tau}]_0$, keeping heparin at the same ratio $R = 1$, and recorded $t_{1/2}$. Then, we calculated γ from the slope of the log-log plot of $t_{1/2}$ vs $[\text{tau}]_0$. We used several $[\text{NaCl}]$ values so that aggregation kinetics is monitored under droplet to non-droplet conditions.

We prepared tauSS and heparin samples with $[\text{NaCl}] = 0$. Turbidity readings scaled linearly with $[\text{tau}]_0$, confirming that droplets formed (Figure S6A). ThT fluorescence of each sample was monitored for 16 hours. The readings were normalized and fitted to extract $t_{1/2}$ (Figure 3-3C) (see Materials and Methods). The log-log plot of $t_{1/2}$ vs $[\text{tau}]_0$ extracted from (Figure 3-3C) resulted in data points that can be fit by linear regression with $R^2 = 0.64$ to extract γ

(Figure 3-3D). We obtained $\gamma = (-0.11 \pm 0.02)$ at $[\text{NaCl}] = 0$ under LLPS-CC conditions (Figure 3-3D). This implies that tau aggregation under LLPS-CC conditions has minimal monomer dependence. We further varied $[\text{NaCl}]$ from 50 to 200 mM. At $[\text{NaCl}] \geq 50$ mM, turbidity readings are independent of $[\text{tau}]_0$, implying that droplet is absent (Figure S6A). The log-log plot of $t_{1/2}$ vs $[\text{tau}]_0$ at all $[\text{NaCl}]$ conditions from 50 to 200 mM can be fit linearly with R^2 above 0.64 to obtain γ (Figure S6C). We observed that γ changes from (-0.11 ± 0.03) at $[\text{NaCl}] = 50$ mM to (-0.26 ± 0.04) at 200 mM, and can be linearly fit with $R^2 = 0.84$ (Figure 3-3E). This means the monomer dependence of aggregation at non-droplet conditions increases as the ionic strength increases. Importantly, γ under droplet condition at $[\text{NaCl}] = 0$ (-0.11 ± 0.02) falls well within the standard error of the linear regression obtained from non droplet conditions (Figure 3-3E), implying γ is altered by the change in ionic strength, but not by the state of LLPS-CC itself. In other words, the monomer dependence of the microscopic process depends on the inter-molecular electrostatic interaction strength modulated by ionic strength, but the increased protein concentration under LLPS-CC is insufficient in and of itself to modulate the microscopic processes governing tau aggregation activity.

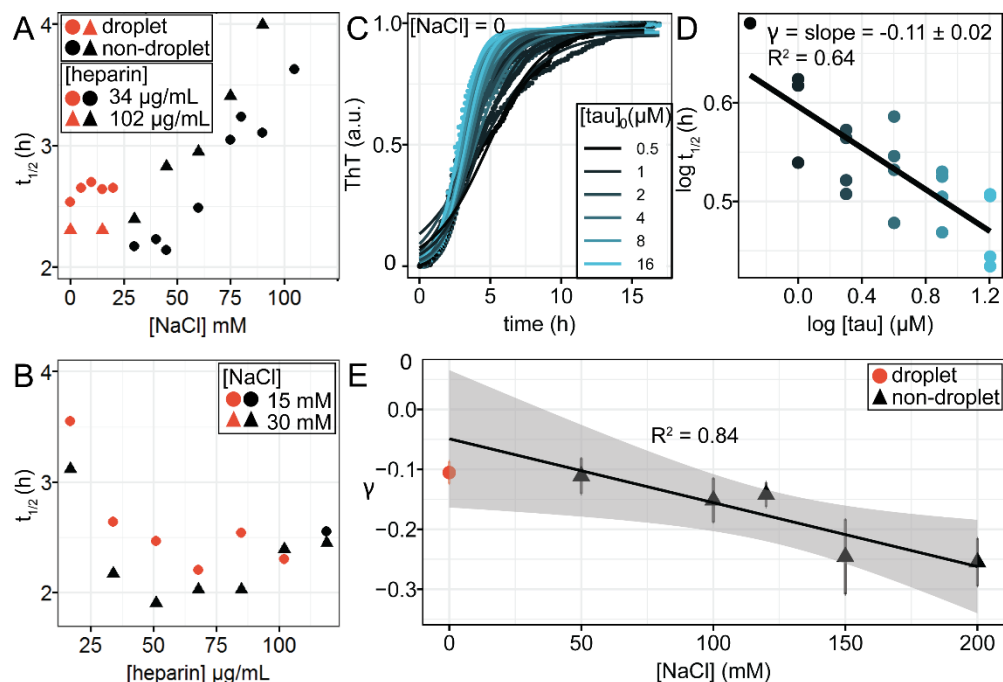


Figure 3-3. Effects of LLPS on tau-heparin aggregation half time and monomer

dependence.

A. $t_{1/2}$ of tau-heparin aggregation at different $[\text{NaCl}]$. 20 μM tauSS with 34 or 102 $\mu\text{g/mL}$ heparin were used. **B.** $t_{1/2}$ of tau-heparin aggregation at different $[\text{heparin}]$. 20 μM tauSS and 15 or 30 mM NaCl were used. Data points in A and B come from independent replicates using three different batches of protein. **C.** Normalized ThT fluorescence of tauSS-heparin mixture at droplet conditions ($[\text{NaCl}] = 0$) with varying initial tau concentration, $[\text{tau}]_0$, from 0.5 μM to 16 μM , colored in gradient from black to blue. Readings are marked in points. Solid line shows the fitted results using sigmoid function. Ratio of heparin was fixed at 1.7 $\mu\text{g/mL}$ heparin per 1 μM tau. **D.** log-log plot of $t_{1/2}$ vs $[\text{tau}]_0$. Data points are $t_{1/2}$'s extracted from fitting (solid lines in A). Solid line is a linear regression of the data points, with $R^2 = 0.64$. The slope of log-log plot is denoted scaling exponent γ . **E.** scaling exponent γ of tauSS-heparin at varying $[\text{NaCl}]$ conditions. Error bars are standard error of the estimate. Solid line is a linear regression of $[\text{NaCl}] = 50$ mM to 200 mM with $R^2 = 0.84$, and shaded area is the confidence interval ($\alpha = 0.95$) of the regression. Data points in C, D and E come from independent replicates using three different batches of protein. In A, B and E, data points in red are conditions with turbidity above 30% maximum and were labeled as droplet conditions.

Aggregation-signature conformation is independent of LLPS-CC

We have previously identified a structural signature of aggregation-prone tau conformers, which consists of an opening of the flanking regions of the hydrophobic PHF6 and PHF6* hexapeptide segments of tau [48]. We here assessed whether a similar conformational change is triggered under LLPS-CC conditions. Double electron-electron resonance (DEER) spectroscopy is a powerful tool that measures intramolecular distances to report on a local conformational ensemble [197], [198]. Here we used DEER to measure the distribution of intra-molecular distances of the tau ensemble between residues 300 and 313, flanking both sides of the PHF6 segment (i.e. ³⁰⁶VQIVYK³¹¹). We referred to the construct containing spin labels at site 300 and 313 as tauSL₂. The concept of this experiment was to measure conformation around tau's PHF6 segment immediately after adding a cofactor that either triggers aggregation, LLPS-CC, or both. The conformation of the PHF6 segment is used as a proxy to evaluate aggregation-prone conformations of tau, as described in previous studies [48]. For reference, two control samples were introduced: tauSL₂ in the absence of polyanion was used to represent PHF6 conformation of tau monomer in solution (referred to as monomer); tauSL₂ in fully aggregated tau-heparin fibrils (24h incubation) was used to represent tau conformation in fibrils. The goal of this set of experiment was to reveal whether tau in the LLPS-CC state populates soluble aggregation-prone conformers.

The first DEER sample (sample I) was prepared by mixing the tauSL₂ with heparin at a ratio $R = 1$. A clear solution immediately became turbid, and light microscope confirmed the abundance of droplets (Figure 3-4A, column 1). Replica were prepared and incubated with

ThT. Fluorescence showed that amyloid aggregates became gradually abundant after overnight incubation. Within 5-10 minutes of preparation, i.e. a state in which the ThT signal was minimal revealing the absence of significant quantities of amyloid aggregates, the sample was flash frozen for DEER measurements (Figure 3-4B, column 1). As expected, both the DEER time trace (Figure 3-4C, column 1) and the extracted distance distribution, $P(r)$ (Figure 3-4D, column 1) showed extended conformations, similar to conformation observed in fully aggregated sample.

This observation is consistent with the previous report that tau adopts aggregation-prone conformation at early stages of amyloid aggregation [48]. The question is whether droplet formation is related to, or presumably facilitates such conformation change. We next prepared the second DEER sample by introducing 4 times more heparin (sample II) to reach a ratio $R = 4$. Under this condition, LLPS did not occur (Figure 3-4A, column 2), while ThT assay shows that aggregation is still triggered (Figure 3-4B, column 2). Despite the absence of droplet, DEER signal and $P(r)$ of the sample II were very similar to the signatures of the fibril sample (Figure 3-4C, D, column 2). This suggests that droplet formation does not further promote tau to adopt the aggregation-prone signature conformation.

Sample III was prepared by incubating tau with hyaluronic acid at charge ratio $R = 1$. Hyaluronic acid has similar backbone and molecular weight as heparin (used in sample I and II), but is free of sulphate groups (Table 2). By doing so, we created LLPS-CC (Figure 3-4A, column 3) without triggering amyloid aggregation (Figure 3-4B, column 3). In the droplet state of tau, the DEER signal and $P(r)$ were found to be similar to those of the monomer tau sample

(Figure 3-4C, D, column 3). This shows that droplet formation in and of itself is not sufficient to drive tau aggregation-prone conformation change. Together, these results show that LLPS-CC does not directly result in tau conformational changes associated with the population of aggregation-prone tau species.

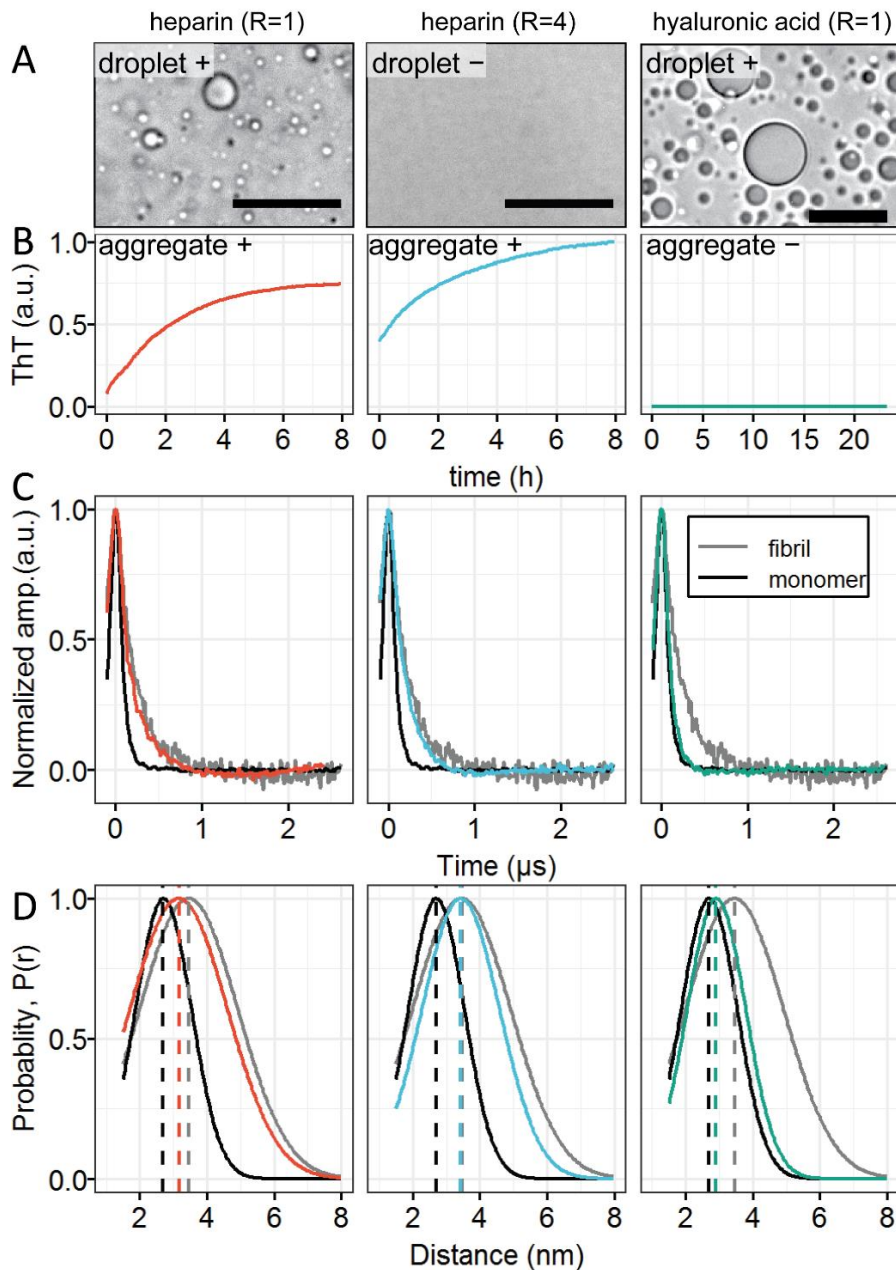


Figure 3-4. LLPS dependence of tau aggregation-signature conformation.

A. Bright field microscope images of tau-heparin sample at $R = 1$, $R = 4$ and tau-hyaluronic acid sample at $R = 1$ in the DEER conditions. $[\text{tau}] = 220 \mu\text{M}$. Scale bars are $25 \mu\text{m}$ long. **B.** ThT fluorescence of samples in A during incubation. **C.** DEER time domain signal. **D.** Corresponding distance distribution $P(r)$. Results in this figure are representative.

Amyloid aggregation can be modulated independently of LLPS-CC

Knowing that LLPS-CC has no direct impact on the conformational state of tau, aggregation reaction rate of tau or final extent of amyloid aggregation, we hypothesized that LLPS-CC and amyloid aggregation are driven by distinct interactions. To test this hypothesis, we modulated tau amyloid aggregation without disturbing the charge-charge interactions between tau and polyanion. We then measured and compared their LLPS-CC and amyloid aggregation under the same experimental conditions.

We first compared 6-O-desulfated, 2-O-desulfated and N-desulfated-reN-acetylated heparins, named 6OD, 2OD and ND, respectively (Table 2). They all have glycosaminoglycan backbone with 2 sulfate and 1 carboxyl charged groups, resulting in an identical charge density ($3 e^-$ per disaccharide), but with different charge location on the backbone (Table 2). According to the supplier, these desulfated heparins are products of the same parent heparin from porcine mucosa. Consequently, they are broadly similar in molecular weight and length distribution. We identify the charge ratio of heparin to tau, R , to represent its stoichiometry. When mixed with tauS under charge neutrality conditions, i.e., $R = 1$, all three heparin variants make droplets with tau (Figure 3-5A). Furthermore, the titration of different ratio R showed that desulfated heparins have indistinguishable turbidity readings on its own for all R in the interval of 0 to 2 (Figure 3-5B). In other words, these three desulfated heparins have similar LLPS-CC propensity. However, incubation of tauS overnight with the desulfated heparins at $R = 1$ resulted in dramatically different ThT fluorescence (Figure 3-5C). Notice 6-O-desulfated heparin has been reported to have lowest affinity with full length tau 2N4R, compared with 2-

O-desulfated and N-desulfated-reN-acetylated heparin [199], while under our experimental conditions 6-O-desulfated heparin showed the highest aggregation propensity (Figure 3-5C). The polydispersity and average molecular weight of the three desulfated heparins have not been tested, but are expected to be comparable given the source and supplier. Regardless of the ordering of aggregation propensity and unknown polydispersity and molecular weight, the observation is clear that the different desulfated heparins yielded similar turbidity upon LLPS-CC of tau and RNA but different ThT fluorescence, demonstrating that tau fibrillization can be modulated by arranging the charged sulfate group position on the glycosaminoglycan backbone, without interfering with and without being affected by LLPS formation.

We then asked whether the disease-associated P301L tau mutation influences the propensity for tau to form LLPS-CC. We compared LLPS-CC with tauS vs. with tauSP301L. TauSP301L differs from tauS by a single P301L mutation—a well-known disease mutation found in fronto temporal dementia [200], but has unaltered charge distribution (Figure 3-5). When mixed with RNA at ratio $R = 1$, both tauS and tauSP301L form droplets (Figure 3-5D). Further titrating tau with varying R showed that both tau variants have similar LLPS-CC propensity (Figure 3-5E). However, incubation of two tau-RNA sample at $R = 1$ showed that tauSP301L-RNA has ThT readings by 2 orders of magnitude higher than tauS-RNA (Figure 3-5F). The much higher aggregation propensity of P301L variants of tau is well known. These results together demonstrate that amyloid aggregation can be modulated by changing either the polyanion chemistry or the tau protein mutation without affecting the LLPS-CC properties.

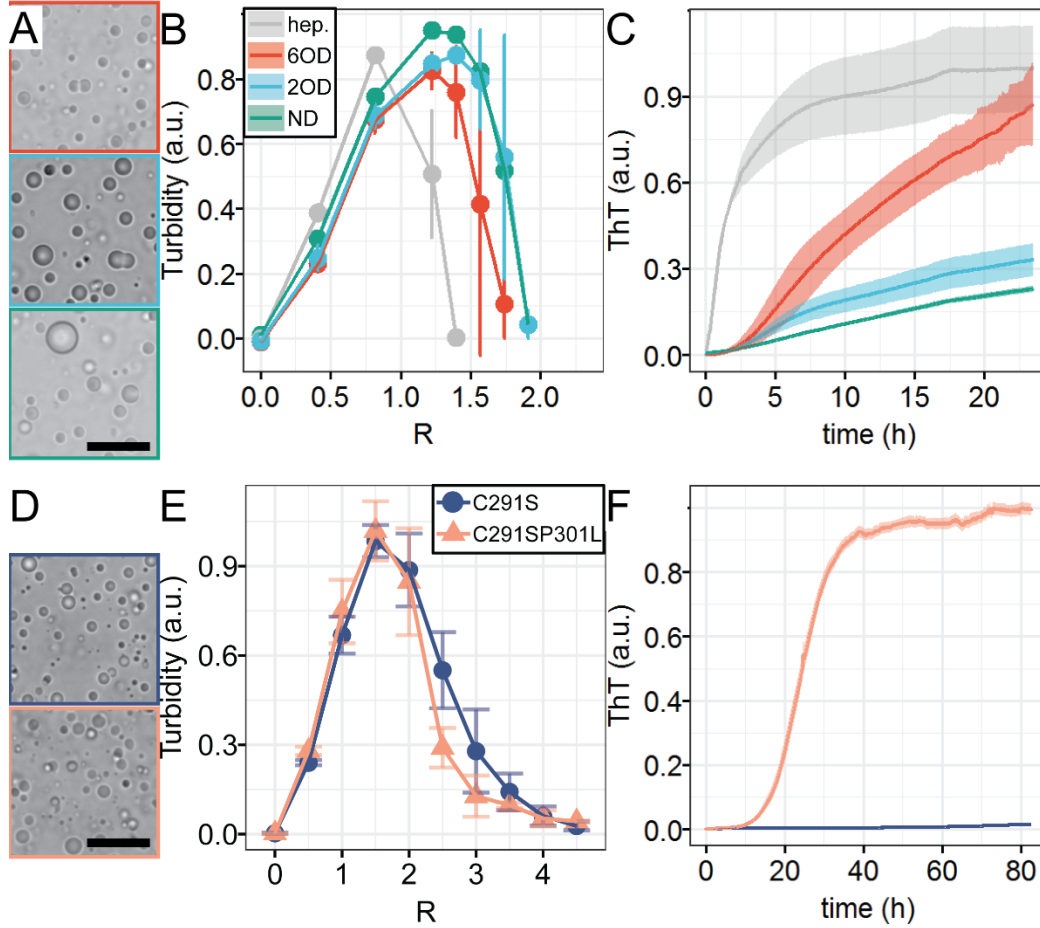


Figure 3-5. Dependence of LLPS on modulating amyloid aggregation.

A. Representative bright field microscope images of tau-polyanions. Hep., 6OD, 2OD, ND are heparin, 6-O-desulfated heparin, 2-O-desulfated heparin and N-desulfated reN-acetylated heparin, respectively. Desulfated heparins were derived from heparin of same molecular weight. $[\text{tau}] = 100 \mu\text{M}$, $[\text{NaCl}] = 0$, $R = 1$. **B.** charge ratio, R , dependence of turbidity for tauS titrated with heparin and different desulfated heparins. $[\text{tau}] = 20 \mu\text{M}$, $[\text{NaCl}] = 0$. **C.** ThT fluorescence of $20 \mu\text{M}$ tauS incubated with heparin and different desulfated heparins over 24 hours. $R = 2.5$, $[\text{NaCl}] = 0$. **D.** Representative bright field images of tau-poly(U) RNA for two tau variants. **E.** Turbidity of tau-poly(U) RNA with different tau variants at varying R . **F.** ThT fluorescence of tau-RNA for different tau variants. Scale bar lengths in both A and B are $20 \mu\text{m}$. Error bars in both B and E, as well as shaded areas in both C and F, show standard deviation of 3 technical replicates.

Different types of tau LLPS exist and possess different properties

The independence of tau amyloid aggregation on LLPS-CC does not necessarily extend to all forms of LLPS, but may be unique to CC of tau and polyanionic cofactors. Hence, we ask ourselves whether the independence between LLPS-CC and aggregation processes of tau is universal to all forms of tau LLPS, especially given literature reports suggesting otherwise [121], [124]. As electrostatic interaction and association between tau and polyanions is the primary driving force of LLPS-CC of tau, we next test whether non-electrostatic interactions can drive tau LLPS. We added excess amount of NaCl to tauSP301L to completely screen electrostatic interactions between the biopolymers. Screening electrostatic repulsion to amplify the effects of non-electrostatic interactions has been applied to induce LLPS of other proteins including mussel adhesive proteins by Hwang and coworkers[201], [202] and TDP-43 [61], [203]. Indeed, in the presence of [NaCl] ~3 M or above liquid droplets were observed (Figure 3-6A). We referred to such LLPS as LLPS-high salt, and the observed droplets as high-salt droplets. A NaCl concentration of 3M is unlikely to be physiologically relevant, and thus we use the LLPS-high salt driven droplet state only as a physical chemistry model. To confirm that LLPS-high-salt is non-electrostatically driven, we added 6 wt% hexanediol (HD). HD has been shown in the literature to disrupt hydrophobic interactions [204], [205], and had been used to dissolve LLPS in other studies [11], [19, p. 72], [124], [206]. Interestingly, LLPS-CC of heparin and tau, formed with heparin at $R = 1$ with 0 mM NaCl, were not affected by the addition of 6 wt% HD (Figure 3-6D). In contrast and remarkably, LLPS-high-salt droplets immediately dissolved with HD (Figure 3-6B), suggesting that the two types of droplets are

driven, and hence disrupted, by different interactions. We hypothesize that LLPS-CC is purely electrostatically driven and the droplet and the polyelectrolyte constituents fully hydrated and therefore insensitive to HD, while LLPS-high salt is at least partially driven by hydrophobic interactions that then can be disrupted by the amphiphilic HD molecules.

Furthermore, incubation of LLPS-high-salt droplets showed sigmoidal growth of ThT fluorescence and fibril-like structure under TEM (Figure 3-6A), showing LLPS-high salt states may promote amyloid fibrilization of tau. Reassuringly, incubation of LLPS-high-salt droplets with HD completely eliminated the ThT fluorescence (Figure 3-6B), suggesting that LLPS-high-salt formation and amyloid aggregation have direct correlations. In contrast, incubation of LLPS-CC droplets showed rapid development of ThT fluorescence, indicating amyloid aggregation is proceeding (as discussed in the earlier sections) independent of HD addition (Figure 3-6B, D). The results (i) show that HD does not interfere with amyloid formation from the LLPS-CC state, and (ii) reinforce the hypothesis that HD can prevent tau aggregation under high-salt conditions by inhibiting LLPS-high-salt. In other words, high-salt droplets might be on-pathway towards amyloid aggregates. While more studies are needed to understand the connection between LLPS and amyloid aggregation of tau at high salt concentration, these results already show that tau LLPS can be driven by various interactions and that LLPS-CC of tau displays specific characteristics that may not be universal to all forms of LLPS of tau.

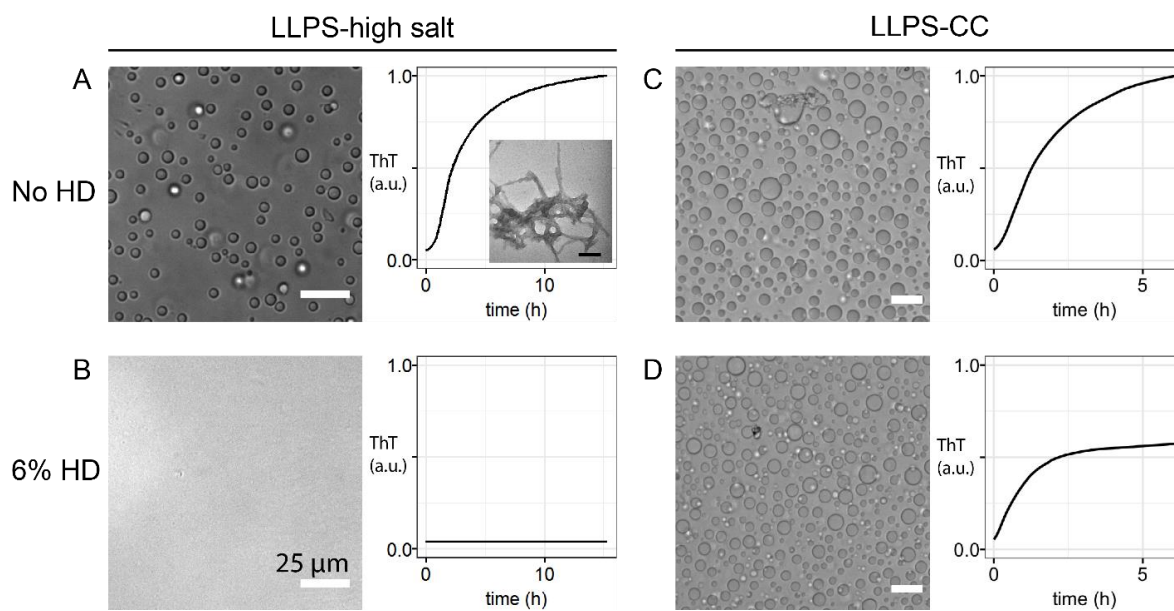


Figure 3-6. LLPS and amyloid aggregation of LLPS-CC vs LLPS-high salt.

Representative bright field images and ThT fluorescence intensity of **A.** 100 μ M tauSP301L mixed with 3.0 M NaCl (Inset shows the TEM image of sample after incubation, scale bar is 100 nm length.); **B.** sample in A with additional 6% hexanediol; **C.** 100 μ M tauSP301L mixed with 170 μ g/mL heparin with no additional NaCl; and **D.** sample in C with additional 6% hexanediol. Reactions were carried out in 1 mM HEPES of pH 7.0 at room temperature. Scale bars of bright field images are of 25 μ m length.

Discussion

Tau droplets and amyloid aggregates have been found to occur simultaneously[121], [124], but it was unclear to date whether tau in condensed droplet state is on pathway towards aggregation of tau. Our study demonstrated that electrostatically driven LLPS-CC and amyloid aggregation of tau can be two independent processes, but that can influence each other under certain conditions. We proposed possible underlying mechanisms.

First, we propose that LLPS-CC and amyloid aggregation of tau-cofactor systems are driven by distinct interactions. This is supported by the observation that tau-heparin amyloid aggregation is eliminated by ionic strength between 160 mM and 320 mM, while $[\text{NaCl}] = 50$ mM is enough to completely dissolve LLPS-CC (Figure 3-2). The common preference of LLPS-CC for low ionic strength is consistent with previous studies [207], [208], and explains why these two processes are often observed under overlapping experimental conditions. However, the Debye lengths (characteristic distance between two point charges in solution beyond which electrostatic interactions become negligible [209]) at 160 mM and 50 mM NaCl are approximately 0.76 nm and 1.36 nm [209], corresponding to an estimated contour length of 2 and 3.6 amino acids, for amyloid aggregation and LLPS-CC, respectively [210]. Therefore, it is likely that amyloid aggregation is mediated by shorter range electrostatic interactions than LLPS-CC conditions can invoke or modulate, as LLPS-CC is already dissolved at the closer contour length of 2 amino acids. Furthermore, the stability of amyloid fibril is known to originate from the inter-backbone hydrogen bond network [211], [212] assisted by specific side-chain interactions [213], [214]. In contrast, complex coacervation of tau and polyanion is dominantly controlled by long-range, weaker and multivalent electrostatic interactions [22], [186]. This explains the result of our study that tau amyloid aggregation is sensitive to changes in the site-specific location and distribution of negative charges on different polyanion cofactors, and is sensitive to specific mutations on tau (Figure 3-5), while LLPS-CC is more tolerant to those variations.

Second, LLPS-CC and amyloid aggregation of tau may have separated pathways. Aggregation-prone conformation of tau facilitates amyloid aggregation regardless of LLPS-CC (Figure 3-4), while LLPS-CC is both insensitive to changes in tau conformations and does not modulate tau conformations. This is consistent with recent reports that the conformational distribution of polyelectrolyte chains under LLPS-CC is indistinguishable from that in solution [81], [215]. Meanwhile we observed that the optimal stoichiometry of heparin that facilitates amyloid aggregation is distinctly different from that for LLPS-CC (Figure 3-2). This is consistent with the previous observations that LLPS of tau and polyanions favors stoichiometry that meets net charge balancing [22], while tau-heparin amyloid aggregation proceeds via a defined molar ratio between tau:heparin, typically 4:1 [216]–[218], likely mediated by directed conformational templating [207], [219].

Tau aggregation and LLPS have been suggested to be linked in recent studies in the literature [121], [124], [187]. It is worth noting that few of the previous studies on tau LLPS carried out extensive measurements at either side of the phase separation boundary, as performed in this manuscript. It is therefore possible that some of the previous reports observed an overlap of LLPS and aggregation conditions, but did not establish a direct cause-effect relationship. The independence of these two processes in our study appears to show contrasting conclusions, but does not necessarily contradict with the observation in the literature. The independence of amyloid aggregation on LLPS-CC may be specific to the tau-cofactor system and the type of LLPS state generated here. LLPS can be achieved also by the simple coacervation mechanism, solely of tau in the absence of polyanion cofactors, as a result of high

salt concentration as shown in Figure 3-6, specific truncation [121], crowding reagent [68] or post-translational modifications (PTMs), such as heavy phosphorylation found in insect cell-expressed tau [124]. Simple coacervation of tau likely involves stronger tau-tau interactions that are unlikely dominant in complex coacervation, as reflected in LLPS-CC being sensitive to ionic strength, but insensitive to 1,6-hexanediol. In contrast, LLPS-high salt and other LLPS states have been reported to be more tolerant to ionic strength and susceptible to 1,6-hexanediol[121], [124]. The observation that LLPS-CC does not induce tau conformational changes[121], [187] and does not facilitate subsequent amyloid aggregation[121], [124] suggest that electrostatic interactions may not be the most relevant force for driving tau aggregation. The observation that LLPS-high salt dissolves upon 1,6-hexanediol addition and facilitates tau aggregation suggests that amyloid aggregation of tau is favorable under conditions where hydrophobic interactions between tau constituents are promoted and/or prevalent.

While our work shows that electrostatically driven LLPS-CC and aggregation of tau-cofactor system have distinct driving forces, the two processes still can interfere when occurring simultaneously. We point out small but reproducible non-linear dependence of $t_{1/2}$ on [NaCl] under droplet conditions (Figure S5B). Data at non-droplet conditions can be fitted to a linear regression trend line (Figure S5B), which indicates the direct dependence of $t_{1/2}$ on [NaCl]. Comparing with this trend line, aggregation under droplet conditions appears slightly slower than without phase separation. We proposed such change may result from two counter-acting properties of droplets: 1) LLPS-CC creates a high concentration environment, which

increase collision probabilities for tau and may speed up amyloid aggregation; 2) Such compartment may also have high viscosity, which reduces the diffusion of tau, and therefore can slow aggregation. If one of the opposing effects outweighs the other, for example the high viscosity over the high concentration effect, this can increase the half time for tau aggregation.

Complex coacervation permits the concentration and colocalization of two or more compounds that have matching charge patterns into LLPS that may be closely related to, or underlie the mechanism of membrane-less organelle formation [12]. This concentration effect is likely to have a much more prominent effect in a cellular context than *in vitro* where only two purified compounds are present (tau and RNA) at 10s of μM . Firstly, the concentration of unbound tau in neurons can be spatially heterogeneous and orders of magnitude lower than in our model experiment, giving little probability for tau-tau collisions and interactions (necessary step of aggregation), unless there is a mechanism of colocalization of tau, possibly in the form of LLPS that may involve additional constituents than simulated in these *in vitro* experiments. Secondly, it has been recently pointed out tau fibrils might naturally incorporate cofactors that may change the dependence between aggregation and LLPS processes [8], [219]. In addition, the colocalization and concentration of enzymes could promote PTMs, such as phosphorylation [220] that may then indirectly influence tau aggregation. LLPS might hence be an essential step to mix tau and pathologically relevant cofactors that become part of or facilitate tau aggregation, or regulate other functional processes. What our study is showing is that the physical properties of the most basic LLPS state formed by the electrostatically driven complex coacervation of tau and cofactor is not in and of itself, and not causatively, providing

a mechanistic basis and driving factors for enhanced aggregation kinetics or propensity. If there is a role that LLPS-CC plays in the aggregation process of tau, it would be on the basis of the interplay of biological factors that can induce aggregation-prone conformational changes mediated by shorter range electrostatic interaction.

Conclusion

In this work we showed that tau is able to undergo LLPS-CC with a wide range of polyanions tested. Among these polyanions, only a subset can facilitate the process of tau amyloid aggregation. Under conditions where tau undergoes LLPS-CC, amyloid aggregates do colocalize with the tau droplets. By establishing a 2-dimensional map (ionic strength and stoichiometry) of LLPS-CC and amyloid aggregation, we found that the state of LLPS-CC does neither directly change the conformational state of tau nor the extent of amyloid aggregation. We found that the half time for aggregation kinetics is insignificantly altered, nor is the monomer dependency of the dominant microscopic processes during aggregation affected by the LLPS-CC state. Instead, we were able to modulate the amyloid aggregation propensity by either changing the polyanion charge configuration or by introducing disease mutations to tau without affecting the tau-cofactor LLPS-CC propensity. We also found the LLPS-CC state does not facilitate cofactor-assisted seeded aggregation of tau. In contrast, we found that the tau LLPS state formed under high salt concentration, driven by completely different interactions, does directly correlate with increased amyloid aggregation propensity of tau.

Figure S1 and Tables

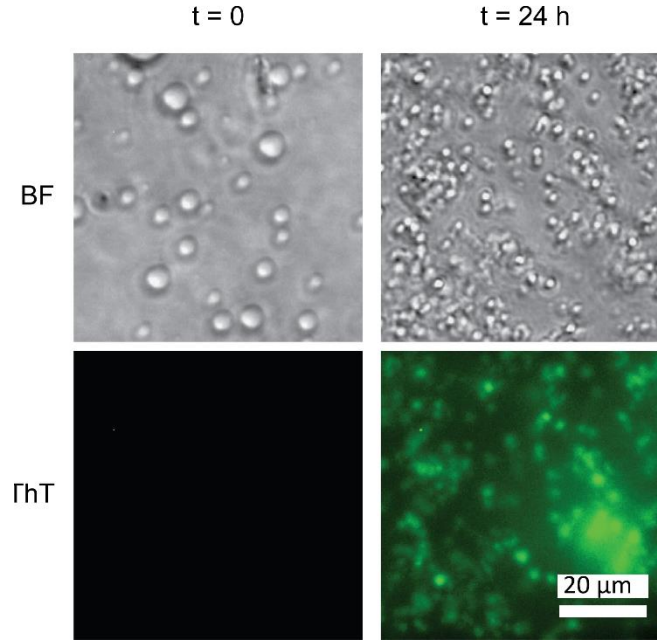


Figure S1. Microscope images of tau-heparin LLPS and amyloid aggregation at room temperature. 100 μM tauS was incubated with 170 $\mu\text{g/mL}$ heparin and 10 μM ThT at room temperature for 24 h. Bright field (BF) images and fluorescence of ThT ($\lambda_{\text{emission}}=485\text{ nm}$) were taken immediately after mixing ($t = 0\text{ h}$), and 24 hours after incubation ($t = 24\text{ h}$). Scale bar is 20 μm long. Results in this figure are representative.

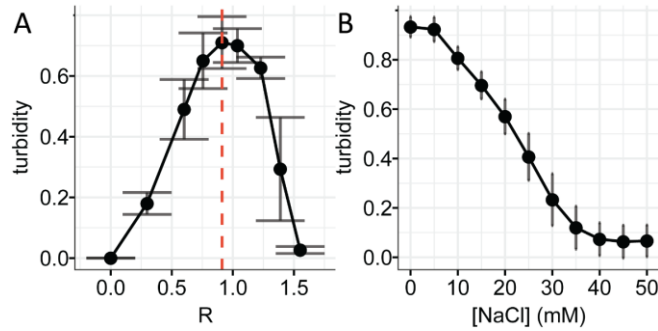


Figure S2. Turbidity dependence of tau-heparin LLPS at varying charge ratio and ionic strength. A. Turbidity of tauS-heparin mixture at varying charge ratio (R). $[\text{tau}] = 20\text{ }\mu\text{M}$, $[\text{NaCl}] = 0$. $R = 1$ corresponds to 1.7 $\mu\text{g/mL}$ heparin per 1 μM tau. Dashed line shows the

position of the peak reading. **B.** turbidity of tau-heparin at varying [NaCl] from 0 to 50 mM. [tau] = 20 μ M, R = 1. Error bars are standard deviation of 3 independent technical replicates.

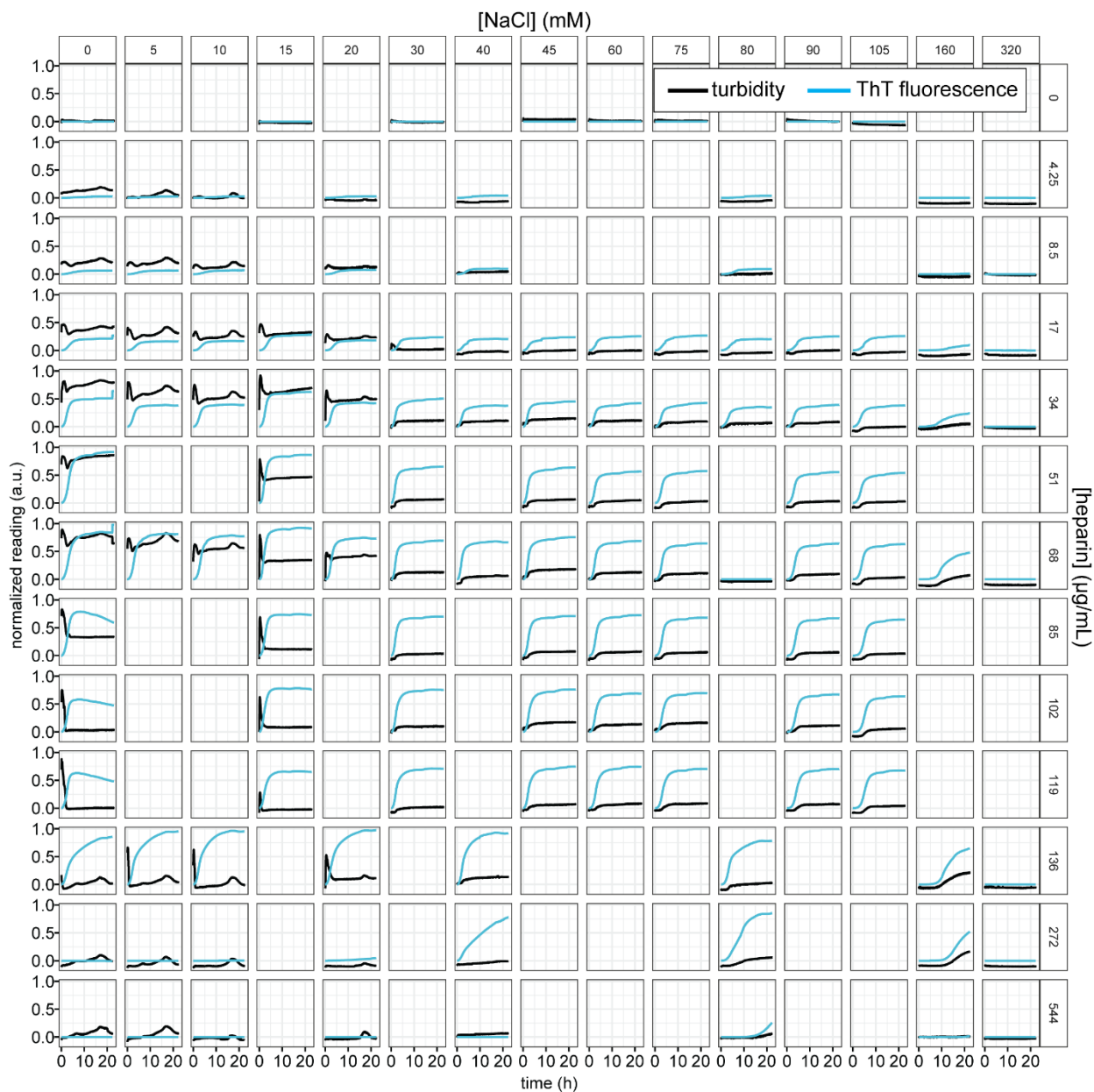


Figure S3. ThT fluorescence and turbidity data of Figure 3-2. 20 μ M of tauSS was incubated with heparin at varying [heparin] and [NaCl]. Turbidity (black) and ThT

fluorescence (blue) of each sample were monitored and scaled to 0~1. Different rows correspond to varying [heparin] from 0 to 544 $\mu\text{g/mL}$. Different columns correspond to varying [NaCl] from 0 to 320 mM. Results in this figure come from three different batches of protein.

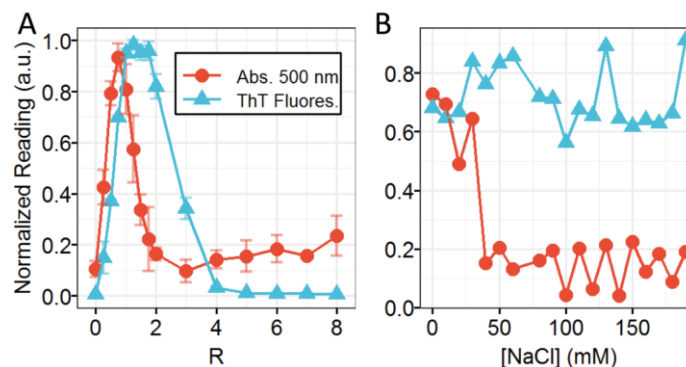


Figure S4. Turbidity and ThT fluorescence of tauS-heparin. **A.** Normalized Turbidity and ThT fluorescence of tau187C291S-heparin aggregation at different charge ratio, R. [tau] = 20 μM , [NaCl] = 0 mM. R = 1 corresponds to [heparin] = 34 $\mu\text{g/mL}$. Error bars show standard deviation of 3 technical replicates. **B.** Normalized turbidity and ThT fluorescence of tau-heparin aggregation at different [NaCl]. [tau] = 20 μM . Charge ratio R = 1. Result in B is representative.

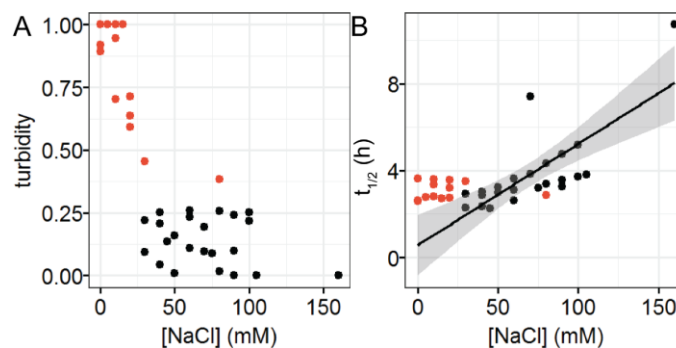


Figure S5. Effects of LLPS on tau-heparin aggregation half time. **A.** Normalized turbidity reading of tauSS-heparin mixture at varying [NaCl]. Data points are independent replicates from three different batches of protein. **B.** $t_{1/2}$ of tauSS-heparin aggregation at different [NaCl]. 20 μM tauSS with 34 $\mu\text{g/mL}$ heparin were used. In both A and B, data points with normalized turbidity above 0.3 are colored in red.

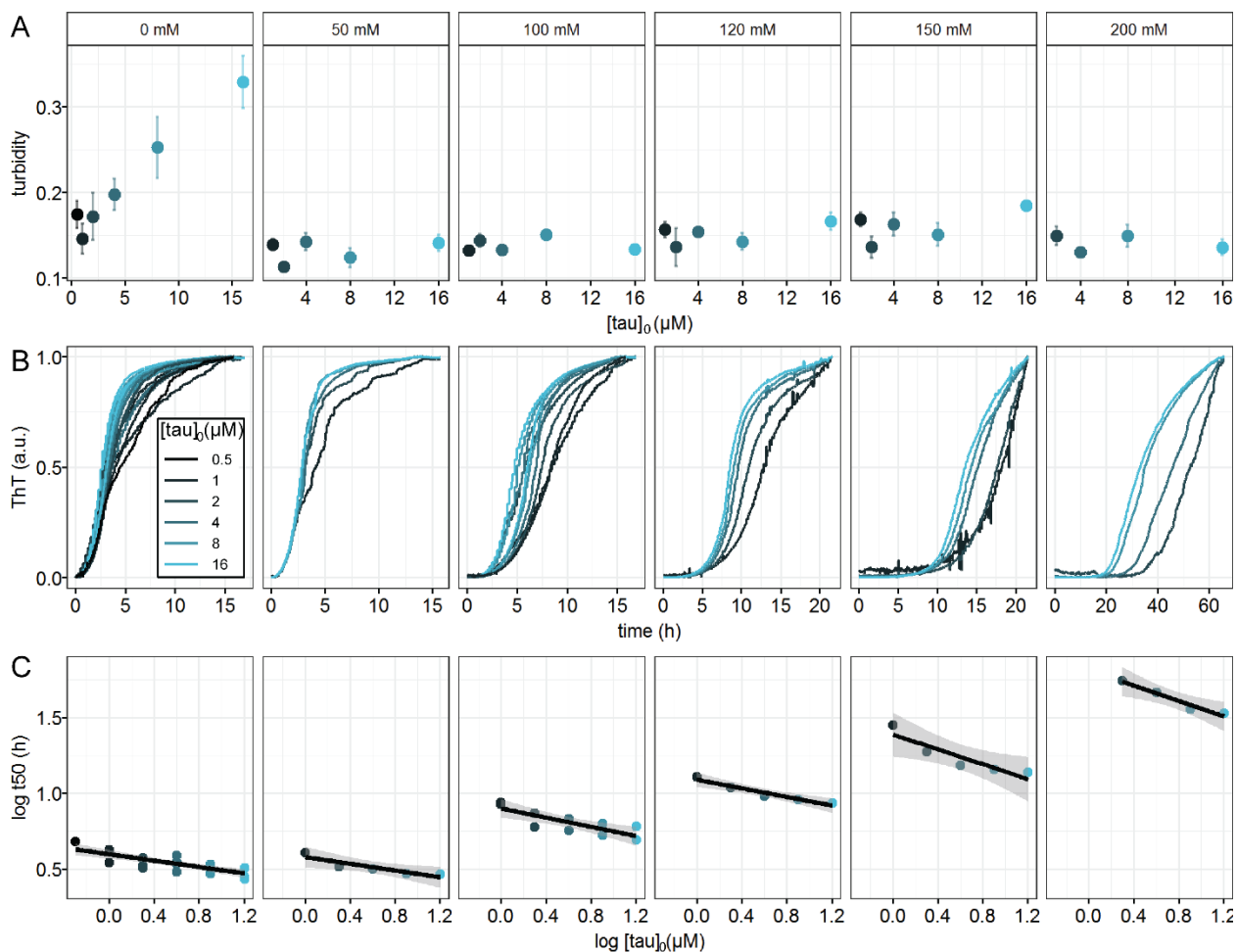


Figure S6. Effects of LLPS on tau-heparin aggregation monomer dependence. **A.** Turbidity of tauSS-heparin mixture at varying initial tau concentration, $[\text{tau}]_0$. Ratio of heparin was fixed at 1.7 $\mu\text{g/mL}$ heparin per 1 μM tau. **B.** Normalized ThT fluorescence of tauSS-heparin mixture at varying $[\text{tau}]_0$ and $[\text{NaCl}]$. Data were fit with sigmoid function to extract $t_{1/2}$ (see Materials and Methods). **C.** log-log plot of $t_{1/2}$ vs $[\text{tau}]_0$. Solid lines are linear regression of the data points. Shade areas show confidence interval of the regression. Slopes of the fit, or γ , are -0.11 ± 0.02 , -0.11 ± 0.03 , -0.15 ± 0.04 , -0.14 ± 0.02 , -0.24 ± 0.06 , -0.26 ± 0.04 , for each panel from left to right respectively. R^2 of the regression are 0.64, 0.82, 0.68, 0.94, 0.84, 0.95, for each panel from left to right respectively. Results in this figure come from biological replicates using three different batches of protein.

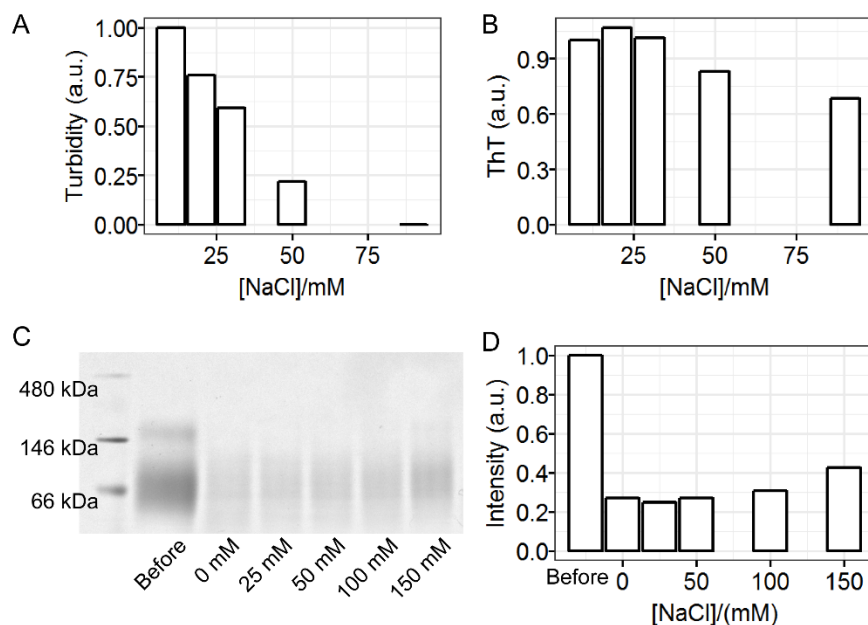


Figure S8. ThT fluorescence of tau-heparin LLPS correlates with amount of amyloid aggregates. 100 μ M of tauSS was mixed with 170 μ g/mL heparin in the presence of varying NaCl. **A.** Mean turbidity of samples at the initial 1 hour. **B.** Mean ThT fluorescence of samples after incubation. **C.** Blue Native PAGE of samples after incubation. **D.** Integrated band intensity of C. Results in this figure are representative.

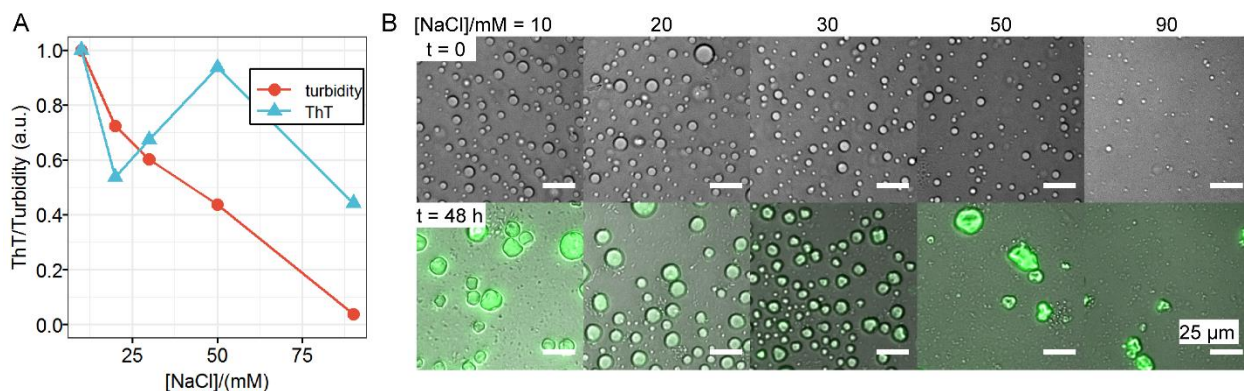


Figure S9. LLPS-CC and amyloid aggregation of full length 2N4R-heparin. 10 μ M of 2N4RC291SC322S was mixed with 17 μ g/mL heparin for an estimated charge ratio of $R = 1$. Samples were incubated at room temperature for 48 hours in the presence of varying additional

NaCl. **A.** Initial (mean of $t = 0-1$ h) reading of turbidity normalized by samples at $t = 0$ mM and 90 mM, compared with final (mean of $t = 48$ h) readings of ThT scaled by reading at $t = 0$ mM. **B.** Microscope images of bright field superimposed with ThT fluorescence (green) of samples at initial and final stages of incubation. Results in this figure are representative.

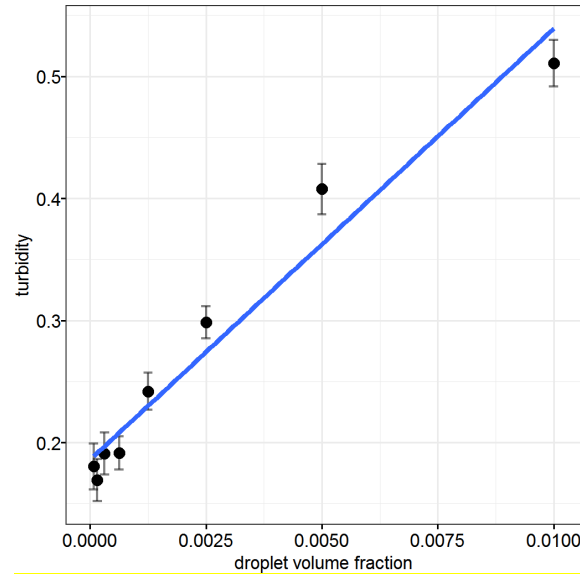


Figure S10. Turbidity vs droplet volume fraction of LLPS-CC formed by hyaluronic acid and poly-L-lysine. We got the materials Hyaluronic acid (HA) and poly-L-lysine (PLL), as well as the idea of using such system from Dongsoo Hwang. HA and PLL stocks were prepared in sodium acetate buffer (pH 5.0) and mixed by 5:1 HA:PLL volume ratio to prepare LLPS-CC. Phase separated mixture was centrifuged at 1000 rcf for 5 min, resulting in dense phase separated from dilute phase. Dense and dilute phases were then collected and mixed at various ratio to prepare samples of given droplet volume fraction. Turbidity readings were acquired, plot against volume fraction (black points), and fit with linear regression (blue line). Error bars show standard deviation of 5 technical repeats.

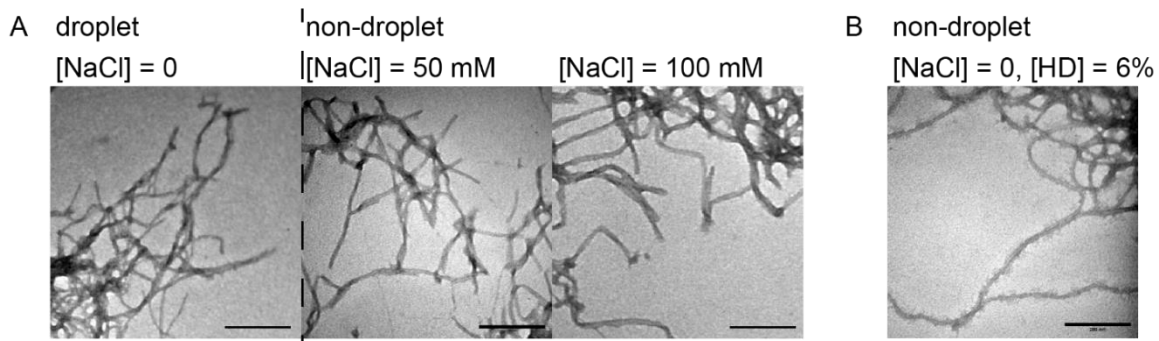
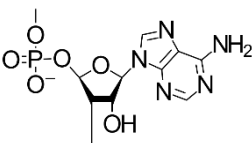


Figure S11. Representative TEM images of tau-heparin samples after incubation. 20 μ M tauSS was mixed with 34 μ g/mL heparin in low ionic strength condition to prepare droplet sample (LLPS-CC). Either additional 50 mM and 100 mM NaCl (**A**), or additional 6 wt% of hexanediol (HD) (**B**) was added to eliminate droplets. Of all samples in this figure, mixture was incubated overnight until ThT fluorescence reached plateau. Samples were then used to prepare TEM grids (fcf-cu-200, EMS), and images were acquired with a JEOL JEM-1230 (JEOL USA, Inc) electron microscopy. Length of all scale bars is 200 nm.

Name	Construct	Est. net charge at pH=7	Est. charge density (e^- /kD)
2N4R	--	+3.1	+0.068
Tau187	Truncated 2N4R, residues 255-441	+9.7	+0.50
TauS	Tau187/C291S		
TauSP301L	Tau187/C291S/P301L		
TauSS	Tau187/C291S/C322S		
TauSSP301L	Tau187/C291S/C322S/P301L		
Tau187V300CV3 13C	Tau187/C291S/C322S/V300C/V31 3C		

Table 1: Names and constructs of different tau variants. Full length longest isoform of human tau, 2NR4, is listed with truncated version, tau187, as well as its mutated variants. The net charge at pH = 7 is estimated by Innovagen's Peptide Property Calculator (<http://pepcalc.com/>), using primary sequence as input. The estimated charge density is calculated using net charge at pH = 7 divided by molecular weight in kD.

Polyanion	Repeating unit	Backbone	Charged groups per repeating unit	Est. net charge at pH=7 per repeating unit	Est. charge density (e^- /kD)
poly(A) RNA		ribose-phosphate	1 phosphate	-1	-3.4

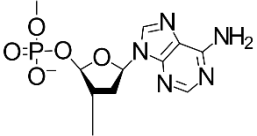
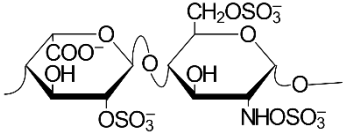
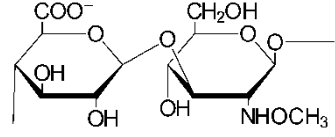
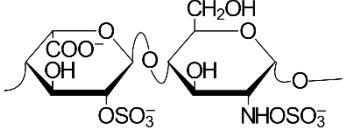
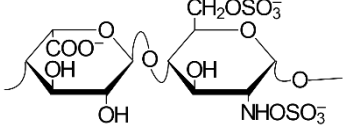
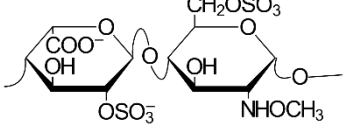
poly(dA) DNA		deoxyribose-phosphate	1 phosphate	-1	-3.2
heparin		glycosaminoglycans	3 sulfate and 1 carboxyl group	-3	-6.7
hyaluronic acid		glycosaminoglycans	1 carboxyl group	-1	-2.6
6-O-desulfated heparin		glycosaminoglycans	2 sulfate and 1 carboxyl group	-2	-6.0
2-O-desulfated heparin		glycosaminoglycans	2 sulfate and 1 carboxyl group	-2	-6.0
N-desulfated reN-acetylated heparin		glycosaminoglycans	2 sulfate and 1 carboxyl group	-2	-5.6

Table 2: Backbone and charged groups of polyanions. The repeating units for heparin and desulfated heparins represent >70% of the chemical. Estimated charge densities are based on the formula weight of the repeating unit.

Chapter 4.

Hydrophobic vs Electrostatic Interactions in Coacervation and Aggregation

Material presented in this chapter is reprinted with permission from Lin, Yanxian, Yann Fichou, Andrew P. Longhini, Luana C. Llanes, Yinson Yin, Guillermo C. Bazan, Kenneth S. Kosik, and Songi Han. “Liquid-Liquid Phase Separation of Tau Driven by Hydrophobic Interaction Facilitates Fibrillization of Tau.” *BioRxiv*, 2020.

Introduction

Tau is a protein mainly present in the central nervous system that binds and stabilizes microtubules in neurons [5], [31], [221]. Under healthy conditions, tau is soluble across a wide range of temperatures, protein concentrations, pH and ionic strengths of the buffer, while under pathologic conditions, tau undergoes amyloid aggregation that yields insoluble, irreversible and cross- β rich fibrils. While the functions of tau are not fully understood, in the healthy state tau is tightly bound to microtubules [222] and the concentration of the unbound tau protein is exceptionally low—on the order of $1\sim 10\text{ nM}^1$. Under pathological conditions, intracellular tau transforms from its microtubule-bound or soluble state to a fibrillar state. In fact, intracellular deposits of aggregated tau are a diagnostic hallmark of a wide range of neurodegenerative diseases known as tauopathies [225]. The mechanism by which low concentrations of tau is recruited to assemble into tangles remains undetermined. Hence, factors that drive assembly and condensation, or generally mechanisms that increase the intracellular local concentration of tau are of great interest to understand this important pathological process.

Liquid-liquid phase separation (LLPS) is a process that is readily driven by multivalent weak interactions between flexible polymers, yielding a polymer-rich phase separated from a polymer-depleted phase [12], [65], the former of which is usually observed as micrometer size

¹ Estimated from tubulin concentration of $40\text{ }\mu\text{M}$ [223], total tau concentration (bound and free) of $1\sim 2\text{ }\mu\text{M}$ [224], dissociation constant of $0.1\sim 1\text{ }\mu\text{M}$ [222] as well as stoichiometry of ~ 0.5 tau/tubulin dimer [157]. See Materials and Methods for calculation.

fluidic droplets. Here, we use the widest definition of polymers that hence includes intrinsically disordered proteins (IDPs) and ribonucleic acid (RNA). LLPS has been used to describe the formation of membraneless organelles *in vivo* that are proposed to play important roles in mediating cellular functions [226], [227]. The interest in biomolecular condensates in the cellular context has exploded in recent years, fueled by intriguing observations of LLPS of IDPs associated with neurodegenerative diseases, including FUS, TDP-43, hnRNPA1, synuclein [11], [13]–[15], [185], [228] as well as more recently tau [22], [121]–[124], [186], [229]. Despite the ubiquitous occurrence of LLPS with IDPs, the physical principles that govern their formation, phase diagrams or properties are not universal. LLPS of IDPs can be driven by a variety of interaction types and with a wide range of interaction strengths. The driving interaction for association that forms the basis for LLPS typically includes electrostatic charge-charge and dipole-dipole interactions between the backbone, charged/polar side chains and polar solvent molecules, and hydrophobic interactions. The latter involve water-repelling protein or polymer side chains that can be aromatic [70], non-polar [65], [230] or even charged residues [231], [232] that, in the context of the protein or polymer surface, may display less favorable protein-water interactions compared to protein-protein and water-water interactions. Molecular crowding, often modeled by adding polyethylene glycol (PEG), can therefore enhance hydrophobic interactions by removing hydration water from the dense LLPS phase [233]. However, the potentially differential role of electrostatic and hydrophobic interactions for the LLPS of tau have neither been investigated nor dissected to date. Recent work [64], [65], [67]–[71] has highlighted certain interactions as particularly important in driving protein

LLPS, in particular π - π and π -cation interaction between charged and aromatic residues [21], [202]. Tau has few aromatic amino acids (~2% for full length tau 2N4R) or arginine residues (~3% for 2N4R), consequently little possibility to engage in π - π or π -cation interactions. Nevertheless, tau's sequence exhibits a rich landscape of chemical properties with polar, charged and hydrophobic residues present throughout the protein. There is a need to study the driving forces of tau LLPS and uncover what role they play in pathology.

LLPS has been shown to promote amyloid aggregation of FUS and hnRNPA1 [11], [13]–[15]. The verdict is not so clear for LLPS of tau. Ambadipudi *et al.* in 2017 [121] and Wegmann *et al.* in 2018 [124] proposed that tau in a LLPS state actively promoted amyloid aggregation, while a recent study from our group [23] showed that tau in LLPS formed by complex coacervation with RNA does not induce or protect from aggregation. Herein, we extensively explore the hypothesis that the nature of the interactions driving tau LLPS is the main factor that influence how LLPS impact amyloid aggregation.

We and others have previously shown that tau undergoes electrostatically driven LLPS (LLPS-ED), either with itself—in a process known as simple coacervation (SC)—or with polyanions—in a process known as complex coacervation (CC) [22], [23], [68], [186]. Meanwhile, tau can undergo LLPS upon addition of high concentration of salt (LLPS-HS)[23]. Concentrated salt (e.g. of NH_4^+ , K^+ or Na^+ along the Hofmeister series) has been shown to exert a “salting-out” effect [234], [235], presumably by dehydrating the protein and promoting entropy-driven hydrophobic interactions among proteins [236], [237]. High concentration of salt including NaCl has been found to induce LLPS of several proteins, including BSA [238],

lysozyme [239] and most recently FUS, TDP-43, and Annexin A11 [240]. In this article, we use the condensation of tau induced by adding high concentration of salt (LLPS-HS) as a model for tau LLPS driven by hydrophobic interactions. Using EPR spectroscopy, fluorescence spectroscopy and biochemical assays, we compared the properties of tau in LLPS-HS with that of LLPS-ED formed by tau-tau or tau-RNA to uncover whether there is a cause-effect relationship between the LLPS and aggregation of tau.

Tau undergoes LLPS at high salt concentration

The longest human tau isoform (2N4R) is a charged and hydrophilic IDP near physiological conditions, displaying both high solubility and stability. The charge and Hopp-Woods hydrophobicity plots (both are moving-averaged over 25 consecutive residues) show that 2N4R consists of a hydrophilic and negatively charged N-terminal half and a weakly hydrophobic and overall positively charged C-terminal half (Figure 4-1A). The four repeat domains (R1–R4) are responsible for binding microtubules and constitute a large part of the core of amyloid fibrils found *in vivo* and *in vitro* [241]. The goal of our study is to investigate tau LLPS based on hydrophobic interactions separately from those based on electrostatic interactions. To maximize the hydrophobicity while keeping the repeat domains, we studied the LLPS of N-terminal-truncated 2N4R between residues 255-441, referred to as tau187 (Figure 4-1A). To mute potential effects of covalent disulfide bonding, we introduced double site mutations to the two native cysteines, C291S/C322S. Unless stated explicitly, we refer to tau187C291SC322S as tau187, and to 2N4RC291SC322S as 2N4R throughout this work.

To eliminate electrostatic interactions, we mixed tau with excess amount of NaCl. Both tau187 and 2N4R samples became turbid and formed abundant droplets when [NaCl] was adjusted to above 4 M and 4.75 M, respectively (Figure 4-1B). After formation, droplets merged within seconds, confirming their fluidity (Figure 4-1C). We refer to this process of high salt concentration-induced LLPS as LLPS-HS, and the resulting droplets as high salt droplets in this article. We furthermore confirmed that both tau187C291S and tau187C291SP301L form LLPS-HS (**Figure 4-1-figure supplement 1**), showing that inter-tau disulfide bonding and aggregation-prone mutations do not prevent LLPS-HS.

We have previously shown that tau187 undergoes LLPS-ED, and established a phase diagram using a combination of experiments, theory underlying coacervation and field theoretic simulations (FTS) of LLPS [186]. The LLPS-ED phase (formed either by SC or CC) typically dissolves at a total salt concentration above [NaCl] ~ 100-200 mM [68], [186], while the LLPS-HS obviously only forms above a much higher salt concentration (3-4 M; Figure 4-1B). The question we ask is whether the properties of the protein tau and the LLPS phase are different between the two forms of LLPS. We start by testing the sensitivity of the dense liquid phase to 1,6-hexanediol (1,6-HD), an amphiphilic small molecule that is known to disrupt weak hydrophobic interactions, [204], [242], [243] which has been widely used to verify the formation and dissolution of various forms of LLPS, including that of FUS [244] and of tau [124], [245]. We prepared tau LLPS-ED in two ways: by mixing tau187 with RNA by the CC mechanism, or by lowering the ionic strength of the solution containing 2N4R (< 10 mM,

referred to as low-salt droplets) that induces SC (Figure 4-1D). When adding 4% 1,6-HD, neither form of tau LLPS-ED, tau-RNA droplets formed by CC or tau low-salt droplets formed by SC, dissolved. In contrast, tau LLPS-HS dissolved completely upon addition of 4% 1,6-HD (Figure 4-1D).

The distinct effect of 1,6-HD demonstrates that the tau molecules are held together in the condensed phase of LLPS by different types of interactions in LLPS-ED versus in LLPS-HS. The observation that the stability of LLPS-ED, whether formed of tau187-RNA CC or of 2N4R SC, is insensitive to 1,6-HD confirmed that the interactions holding tau together in the condensed phase is not weakened by an amphiphilic molecule; this behavior is expected for purely electrostatic associations. Considering that the Debye length at 4 M NaCl is ~0.1 nm, which is much smaller than the diameter of a water molecule [209], [246], electrostatic interactions between tau molecules are muted in LLPS-HS. Besides electrostatic screening, salts made of Na⁺ and Cl⁻ at these concentrations also exert dehydration induced salting out of proteins following the Hofmeister series. Together with the observation that 1,6-HD dissolves high salt droplets, these results demonstrate that LLPS-HS are predominantly hydrophobically driven. Hydrophobic interactions arise from weaker protein-water compared to water-water and protein-protein interactions, resulting in (i) water to be readily expelled from the protein surface to rather hydrogen bond with other solvent molecules, i.e. other water molecules in the bulk, and (ii) protein molecules to interact via van der Waals interactions. Amphiphilic molecules such as 1,6-HD can restore interactions between protein and water and/or disrupt interaction between associated proteins, disrupting the hydrophobic driving forces for LLPS-

HS. These results verify that LLPS-HS is a good model system to study the consequences of hydrophobically driven LLPS on the irreversible process of aggregation.

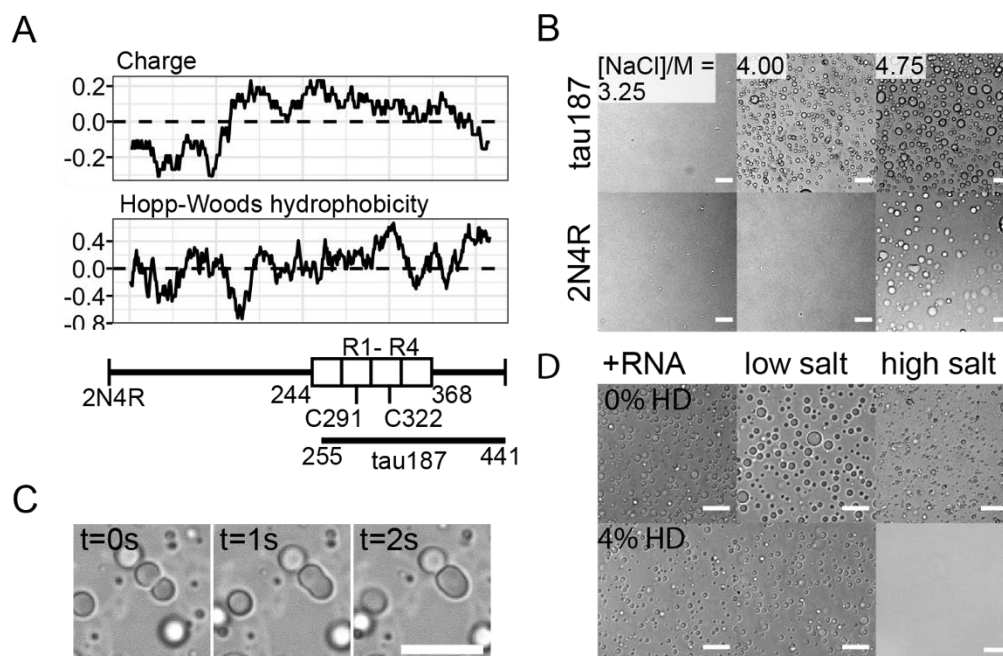


Figure 4-1. Tau undergoes LLPS at high salt concentration.

A. Charge and Hopp-Woods hydrophobicity plot of 2N4R. Data points show the average values of consecutive 25 amino acids. Reference values of Glycine are shown as dashed lines. Diagram of tau187 (2N4R 255-441), four repeat domains (R1–R4, 244-368) and two native cysteines (C291, C322) are shown. **B.** Microscope images of tau187 and 2N4R at varying [NaCl]. 44 μ M tau187 and 20 μ M 2N4R were chosen to have same mass concentration. Scale bar length is 25 μ m. **C.** Droplet merging of tau LLPS-HS. 450 μ M tau187 with 2.2 M NaCl was used. Scale bar length is 50 μ m. **D.** Effects of 4 wt% 1,6-hexanediol on different types of tau LLPS. Tau-RNA LLPS (+RNA) was prepared with 20 μ M 2N4R and 40 μ g/mL polyU RNA; Tau low salt simple coacervation (low salt) was prepared with 20 μ M 2N4R at 5 mM NaCl; Tau high salt simple coacervation (high salt) was prepared with 100 μ M tau187 with 4.75 M NaCl. Scale bar length is 25 μ m.

LLPS-HS undergoes irreversible maturation.

Many examples of protein LLPS have been shown to undergo irreversible maturation [15], [247]. To study the reversibility property of LLPS-HS, we recorded turbidity of high salt droplet samples upon repeated heating-cooling cycles. At 3.5 M NaCl, turbidity at $T < 35\text{ }^{\circ}\text{C}$ remains near zero and significantly increases to 0.4 at $T > 40\text{ }^{\circ}\text{C}$, indicating a lower critical saturation temperature behavior (LCST) where LLPS is thermodynamically more favorable at higher temperature (**Figure 4-2-figure supplement 1A**). When cooled down to low temperature, the original transparent sample remained slightly turbid (**Figure 4-2-figure supplement 1A**), a second heating-cooling cycle showed further increase of remaining turbidity. In contrast, tau-RNA LLPS-ED formed by CC showed no remaining turbidity after consecutive heating-cooling cycles (**Figure 4-2-figure supplement 1B**). The same results were found with 2N4R (**Figure 4-2-figure supplement 1C**). The hysteresis in the build-up of turbidity with repeated heating-cooling cycle implies that LLPS-HS leads to partially irreversible associations between tau, while LLPS-ED formation and melting is reversible.

To further probe the micro-environment inside droplets, we labeled tau with an in-house synthesized fluorescence molecular rotor derived from a boron-dipyrromethene (BODIPY) core [248] and performed Fluorescence Lifetime Image Measurements (FLIM) over the course of 48 hours (See Materials and Methods for synthesis and microscopy details). Molecular rotors are a class of dyes whose fluorescent lifetimes are sensitive to the local microviscosity of their environment, with a low lifetime indicating a fluid, water-like environment and a high lifetime representing a viscous environment [249]–[251]. Further, within a limited regime, the

relationship between the fluorescent lifetime and the microviscosity follows the Förster-Hoffman equation (see calibration between fluorescent lifetime and viscosity in **Figure 4-2-figure supplement 2**). Unlike viscosity that describes the bulk property of a liquid, microviscosity describes the friction that, in this case, is experienced by a single biomolecule due to its local environment. The molecular rotor was conjugated to 2N4R, as described in Materials and Methods. FLIM images were collected on a confocal microscope and a pixelwise fit of the images binned into histograms. Shortly after triggering LLPS, 2N4R LLPS-HS droplets showed a Gaussian distribution of lifetimes centered around 4.08 ± 0.32 ns (916 cP). In comparison, 2N4R LLPS-ED droplets formed by CC between 2N4R and RNA (**Figure 4-2E, F**) showed a lifetime centered around 3.55 ± 0.07 ns (195 cP). In other words, 2N4R in LLPS-HS experiences a higher microviscosity than in LLPS-ED. After a 48 hour incubation period, the average fluorescence lifetime of 2N4R in LLPS-HS samples increased from 4.08 ± 0.26 to 4.15 ± 0.13 ns (**Figure 4-2F**), while that of 2N4R in LLPS-ED decreased from 3.55 ± 0.07 ns to 3.39 ± 0.12 ns (**Figure 4-2E, F**). Concurrently, amorphous, non-spherical condensates formed within LLPS-HS, while the overall droplet shape of LLPS-ED (of 2N4R-RNA CC) remains spherical (**Figure 4-2B, D**). The emergence of non-spherical structures within the droplets and the increase in microviscosity sensed by the tau protein indicate that LLPS-HS undergo maturation of the condensate. LLPS-ED on the other hand retains liquid properties that appears to slightly less viscous over time.

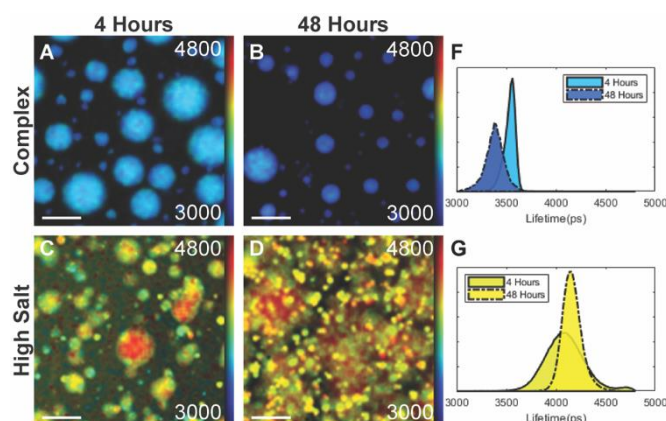


Figure 4-2. FLIM fits of tau-RNA LLPS-CC and tau LLPS-high salt.

Fluorescence Lifetime Imaging Measurements were taken at 4 and 48 hours at the same resolution, scale bar = 25 μm . **A-D**, Fluorescent microscope images of tau-RNA droplets and tau high salt droplets before (4 hour) and after incubation (48 hour). Individual pixels were fit with a 2 component exponential decay using the FLIMfit software tool developed at Imperial College London [252], and the data was visualized using the higher lifetime component. The colors in the fluorescent images and corresponding histograms represent a pseudo color heat map that ranges from 3000 to 4800 ps, with blue representing low lifetimes and red representing high lifetimes. **F-G**, Histograms of fitted results in A-D. The histograms are normalized so that area under the curve is 1. The color under each histogram corresponds to the pseudo color of the heat map at the histograms max value. Solid line = 4 hours, Dashed line = 48 hours.

LLPS-HS triggers canonical tau amyloid aggregation

To test the hypothesis that maturation of droplets is associated with amyloid formation in the sample, we incubated high salt droplets with a trace amount of Thioflavin T (ThT). While high salt droplets emerge spontaneously and fully upon preparing samples under droplet-forming conditions, ThT fluorescence starts from baseline and steadily increases over ~24 hour duration (**Figure 4-3A**). The increase of ThT fluorescence reflects an increase in cross- β sheet content developing over hours. Subsequent imaging of tau samples—in LLPS-HS conditions

after overnight incubation— showed fibril-like species by TEM that are visually similar to tau-heparin fibrils (**Figure 4-3B**). This supported the hypothesis that LLPS-HS is followed by the amyloid aggregation of tau.

To show the connection between LLPS-HS and amyloid aggregation, we incubated tau at equal concentration, while varying [NaCl] on a multi-well plate. We recorded bright field microscope images before incubation showing the amount of high salt droplets, after which we monitored ThT fluorescence over time (**Figure 4-3A**). The abundance of droplets visually observed via bright field microscope imaging immediately after sample preparation (at $t = 0$) strongly correlates with the ThT fluorescence intensity after incubation ($t = 24$ hours). The same results were found with 2N4R (**Figure 4-3-figure supplement 2**). The initial turbidity (at 500 nm) that quantifies the volume fraction of high salt droplets at $t = 0$ (Figure SI 10 in [23]) was plotted against final ThT fluorescence readings at $t = 24$ hours, representing the relative amount of amyloid aggregates formed (**Figure 4-3C**). We found a proportional correlation (linear R^2 of 0.43) between the initial turbidity and the final ThT fluorescence readings (**Figure 4-3C**). This result implies that LLPS-HS causally triggers amyloid formation. In contrast, electrostatically driven LLPS neither promotes RNA-assisted tau aggregation, nor prevents heparin-induced tau aggregation as shown in **Figure 4-3C** and **Figure 4-3-figure supplement 1**, and as previously reported [23]. These results show that the strong correlation between LLPS and amyloid aggregation is unique to hydrophobically-driven LLPS, as represented by LLPS-HS, while LLPS-ED and aggregation are independent processes.

We further studied the effects of the frontotemporal dementia-related mutation P301L of tau on the correlation between LLPS-HS and aggregation. Our data showed that tau187P301L shows an even steeper dependence of the final ThT fluorescence intensity to the initial droplet quantity at $t = 0$ (**Figure 4-3C**), implying that for a similar initial volume of droplets, tau187P301L generates higher quantities of cross β -sheet structures, resulting in higher ThT fluorescence intensity. Meanwhile, an analysis of the aggregation half time showed that in all examined conditions P301L has significantly shortened the half time (**Figure 4-6-figure supplement 2**). These results showed that P301L promotes tau aggregation under LLPS-HS conditions, consistent with its broadly known aggregation-promoting properties under various *in vitro* and *in vivo* conditions. Similar results were observed with 2N4R (**Figure 4-6-figure supplement 1**).

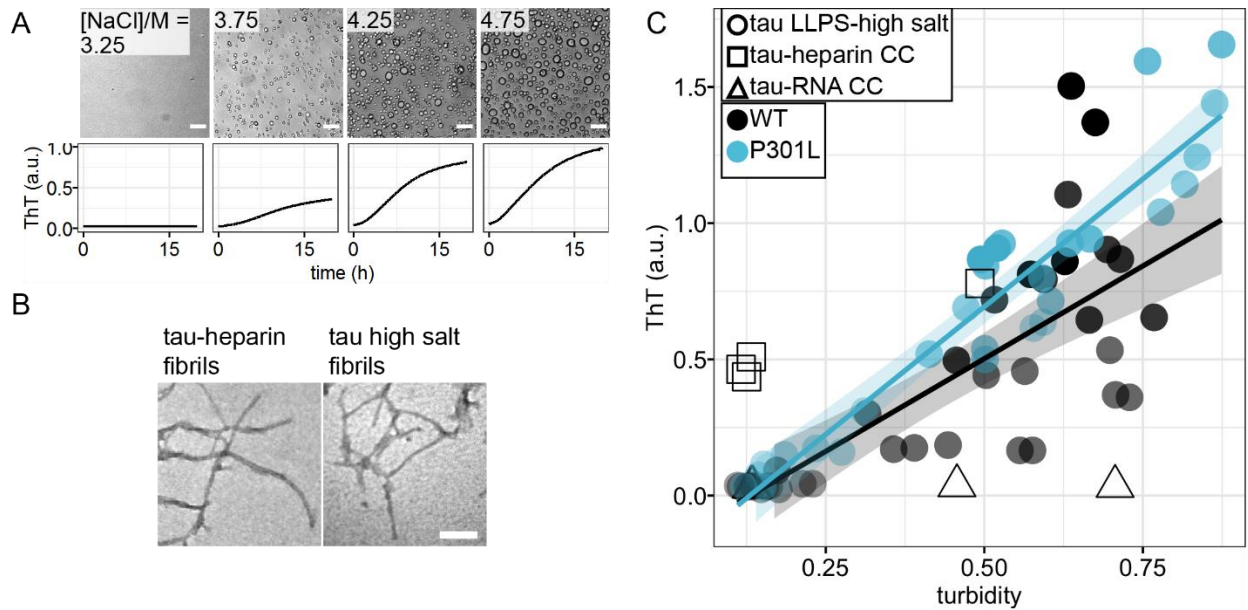


Figure 4-3. Correlation of LLPS-high salt and amyloid aggregation.

A. Representative microscope images at $t = 0$ and ThT fluorescence at room temperature overnight of tau LLPS-high salt at various [NaCl]. 44 μM tau187 was used. **B.** Representative TEM image of tau LLPS-high salt sample after overnight incubation, compared with tau-heparin fibrils. **C.** Correlation of initial turbidity and final ThT fluorescence of tau LLPS-high salt vs LLPS-CC. Solids line and shadow show linear regression and its standard error. 40 $\mu\text{M} \pm 10\%$ of tau187 was used. Samples come from 5 different batches of proteins.

Dehydration facilitates hydrophobically driven LLPS-HS

To reveal the mechanisms that promote the transition of tau from high salt droplet to tau in fibrils, we next focused on investigating the driving forces for tau to form in LLPS-HS. The dissolution by 1,6-HD showed high salt droplets to be held together by hydrophobic interaction (**Figure 4-1D**). When increasing the amount of 1,6-HD, we found the minimum [NaCl] to induce LLPS-HS to shift significantly towards higher NaCl concentration (**Figure 4-4-figure supplement 3C**). This implies that a greater amount of salt is needed to restore the same enhancement of hydrophobic interactions that are disrupted by 1,6-HD.

Turbidity shows LLPS-HS is favored at higher temperature, following lower critical saturation temperature behavior (LCST) (**Figure 4-2-figure supplement 1A, C**). This suggests that free energy for LLPS-HS is rendered negative ($\Delta G < 0$) by a dominant and positive entropy term, $T\Delta S$, according to $\Delta G = \Delta H - T\Delta S$. LCST behavior is seen when phase separation is accompanied by an increase in total entropy (i.e. $\Delta S > 0$) that, as a result, leads to an increasingly dominant and positive entropy ($T\Delta S$) term at higher temperature. The temperature at which $\Delta G = 0$ is then the phase transition temperature, cloud point T_{cp} , above which phase separation occurs spontaneously. Interestingly, either increasing [NaCl] or increasing [tau] lowers the T_{cp} above which LLPS-HS occurs (**Figure 4-4-figure supplement 1**). This finding suggests that

both the addition of salt and higher tau concentration contribute to entropy gain upon LLPS. When adding PEG as a molecular crowder, we observed that the minimum [NaCl] necessary to induce LLPS-HS also shifted towards lower concentrations (**Figure 4-4-figure supplement 3B**). A recent study by Park et al. demonstrated that PEG increases the entropy term upon LLPS by dehydration, and so enhances LLPS without partitioning into the dense phase of LLPS [233]. Taken together, our results are consistent with NaCl and PEG both sequestering water, and hence depleting the protein system of free water in a process known as salting out [236], [253]. Dehydration of the tau-water system will facilitate hydrophobic interactions and subsequent condensation by an increase of the entropic term $T\Delta S$.

While the observations made by systematic changes in [NaCl], [tau], [PEG] and temperature is consistent with dehydration- and entropy-driven LLPS-HS, a more direct observation of dehydration is more satisfying. To measure the effect of dehydration near the tau protein surface, we labeled tau with unpaired electron spin labels to perform electron spin envelope echo modulation (ESEEM) and Overhauser dynamic nuclear polarization (ODNP) measurements. ESEEM measures the relative changes in the local water density within a $\sim 3\text{-}6$ Å shell around a spin label [254], [255], while ODNP measures water accessibility [256] and translational diffusivity within a shell of $\sim 5\text{-}10$ Å [257], [258] (**Figure 4-4A**).

We labeled tau187 with MTSL on site 313 within the R3 domain and dissolved it into a deuterium-based buffer. The magnitude of the ESEEM deuterium peak intensity dropped by over 20%, immediately upon addition of NaCl that led to the formation of high salt droplets

(**Figure 4-4B**). This result represents a significant reduction of local water density near site 313.

We furthermore carried out ODNP relaxometry measurements to determine the cross-relaxivity parameter k_σ , for tau187 at sites 303, 313, 322 and 404, representing the 4R domain and the C-terminal region of tau. The k_σ value reflects on local water accessibility and/or translational diffusivity within ~1 nm of the spin label (Eq. 5 of [259]). We found that the value of k_σ dropped from 31 - 56 $\text{M}^{-1}\text{s}^{-1}$ to 9 - 23 $\text{M}^{-1}\text{s}^{-1}$ for all four sites as soon as high salt droplets formed (see per site trend in **Figure 4-4C**). Note that k_σ measured on the free radical 4-hydroxyl-TEMPO was unchanged upon addition of salt at concentrations that induce LLPS-HS (**Figure 4-4C**). Therefore, the decrease of k_σ observed reflects a change in hydration properties near the tau protein surface upon LLPS-HS formation. The reduction of the deuterium peak magnitude in ESEEM at site 313 shows that the reduction of water accessibility contributes to the drop of k_σ . Given the ~25% reduction of deuterium peak magnitude together with the 50~80% drop in k_σ (**Figure 4-4, Figure 4-4-source data 1**), it is reasonable to assume that it reflects, in addition to local dehydration, a significant slowdown of surface water diffusivity near the microtubule binding domain and C-terminal of tau when condensed into LLPS-HS. Strikingly, k_σ remains unchanged upon formation of tau-RNA LLPS-ED (**Figure 4-4C**), showing that dehydration of LLPS-internal water is a characteristic associated with hydrophobically driven LLPS-HS, but not of LLPS-ED.

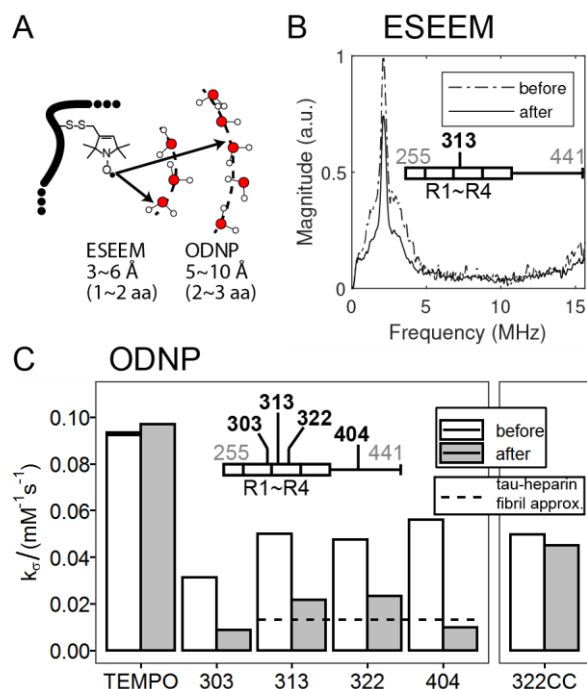


Figure 4-4. LLPS high salt undergoes dehydration.

A. Schematic diagram showing sensitive hydration shell in Electron Spin Echo Envelope Modulation (ESEEM) and Overhauser Nuclear Dynamic Polarization (ODNP). **B.** Representative 3 pulse-ESEEM of tau187 at site 313 at solution (before) and upon addition of 3.75 M NaCl (after). 22.5% Ficoll was used as glassing reagent. **C.** Representative ODNP cross-relaxivity parameter k_{σ} of tau187 at various sites at solution (before) and upon addition of 3.75 M NaCl (after). 250 μM tau was used. For comparison, k_{σ} of tau187 at site 322 upon tau-RNA complex coacervation was shown (322CC). 80% reduction of k_{σ} has been reported at site 313, 322 and 404 for tau-heparin fibrils (Pavlova, et al 2016), and is shown as dashed line.

Dehydration reduce tau dynamics and trigger oligomer formation

To study the dynamics of tau within high salt droplets, we carried out continuous wave (cw) EPR spectroscopy. We labeled tau187 at four different sites: 303, 313, 322 and 404, and extracted the rotational correlation times of the tethered spin label, τ_R , from fitting the cwEPR

lineshape (see Materials and Methods). The value for t_R of the tethered spin reflects on the local protein mobility, as the spin label is tethered to the protein side chain with steric constraints [104]. We first looked at t_R of the four sites before and after forming LLPS-HS. We found that LLPS-HS formation results in dramatic changes in the spectral lineshape of the spin labeled tau (**Figure 4-5A**, **Figure 4-5-figure supplement 2**). We used the microscopic order macroscopic disorder (MOMD) model [260] with incremental complexity to fit the cw EPR lineshapes, using the MultiComponent program developed by Christian Altenbach. At $[\text{NaCl}] = 0\text{--}1.5\text{ M}$ (no droplets), lineshapes of the samples were well fit with one isotropic t_R component (**Figure 4-5-figure supplement 2**). Increasing $[\text{NaCl}]$ to 3 M and above resulted in LLPS-HS. The lineshape of the samples deviated from the one component fit, and required an additional mobility component (**Figure 4-5-figure supplement 1A**). The extracted t_R and the population of each component is represented in **Figure 4-5B** as a function of salt concentration. We found that t_R of the second component was significantly higher than for the first component (i.e. slower dynamics), for all sites. The second component represented 65–96% of the spin label population above 3 M NaCl (**Figure 4-5-source data 1**). Meanwhile, increasing $[\text{NaCl}]$ up to 4.5 M alone does not change the lineshape of the free radical 4-hydroxyl-TEMPO (**Figure 4-5-figure supplement 4**), showing the effects of high salt concentration do not change the rotational dynamics of the spin itself. We hypothesize that this increase of rotational correlation time t_R reflect on the formation of higher molecular weight assemblies, i.e. oligomers. These results imply that the dynamics of the majority of tau proteins, reported on via protein-tethered spin labels, is slowed down in the LLPS-HS state. In

addition to the slowed rotational dynamics, we found emergence of rotational anisotropy in the second component for [NaCl] above 4 M. The presence of anisotropy indicates that the tethered spin label is highly restricted [260], [261], likely from steric hindrance of nearby tau protein, suggesting that tau starts to more tightly pack into protein assembly at very high salt concentration.

Next, we endeavor to show whether the formation of these oligomer species, revealed by slow label dynamics, originates from high salt concentration or from LLPS itself. First, in the absence of high salt droplets, we observed that the lineshape of cw EPR spectra of the tau-tethered spin label broadened upon NaCl addition, giving an average t_R of ~450 ps without NaCl and ~600 ps at 1.5M, at all sites (**Figure 4-5-source data 1**). In addition, at constant [NaCl] we titrated [HD] from 0% to 10%, where [HD] above 2% eliminated droplets. CwEPR lineshape analysis showed that the correlation time was neither abruptly nor distinctly reduced in the absence of droplets above 2% HD (**Figure 4-5-figure supplement 3**). These results show that the drastic reduction in protein dynamics, which we hypothesized to reflect on the formation of oligomers, originate from dehydration by concentrated salt, only indirectly by LLPS.

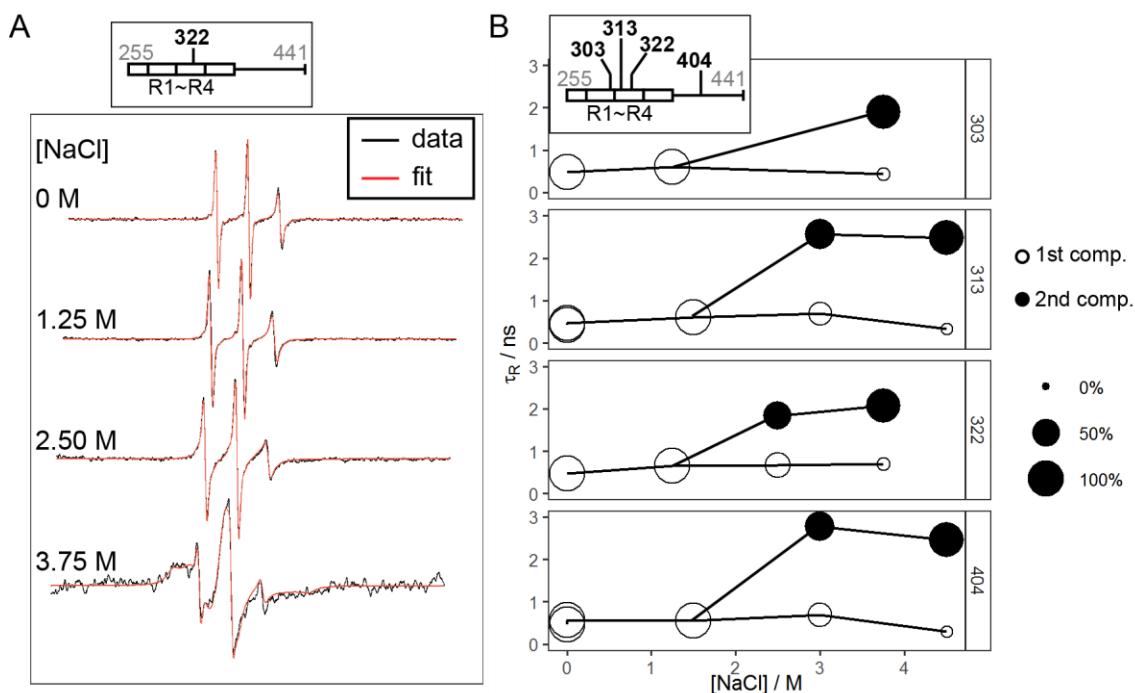


Figure 4-5. Site specific dynamics of tau187 upon LLPS-high salt.

A. Representative X-band cwEPR lineshape of tau187 at site 322 at varying [NaCl]. Black line shows the experiment data and blue line shows the fit. Spectra are shifted to avoid overlap. **B.** Rotational correlation time, τ_R , of tau187 at site 303, 313, 322 and 404 at varying [NaCl]. Data at low [NaCl] were fit with 1 component with the y-axis showing the τ_R . Data at high [NaCl] were fit with 2 components with the area of the disk proportional to the percentage of each component.

P301L promotes hydrophobic interactions

One of the mysteries in tau amyloid aggregation is how a single site mutation, e.g, P301L, dramatically promotes the aggregation propensity of a protein of hundreds of amino acids. We propose here a plausible mechanism. We utilize LLPS-HS as a tool to measure hydrophobic interactions among tau. We studied the effects of the P301L mutation on LLPS-HS propensity. We measured turbidity of tau187 with and without P301L mutation under the exact same

conditions. Turbidity from independent biological repeats showed that in the presence of an intermediate salt concentration of 3.25 M, the presence of P301L mutation significantly promoted LLPS-HS formation (**Figure 4-6B**). In other words, the P301L mutation lowers the [NaCl] threshold required to induce LLPS-HS. Representative microscope images, shown in **Figure 4-6A**, confirmed that P301L promotes high salt droplet formation. These results suggest that the P301L mutation promotes hydrophobic interactions among tau proteins, in agreement with previous proposal that P301L mutation extends local conformation, hence reveals the hydrophobic hexapeptide ³⁰⁶VQIVYK³¹¹ [262]. However, whether the increased hydrophobicity of tau in the presence of P301L is solely due to conformational changes or other biophysical factors requires in-depth studies in the future. In addition, we observed that the ThT activity triggered by LLPS-HS (shown in **Figure 4-3** for wild type (WT)) increases further for P301L compared to WT (**Figure 4-6C**). This enhanced ThT fluorescence for P301L mutant is most likely a combination of both the promotion of droplet formation (which in turn triggers ThT-sensitive aggregation) and a high aggregation propensity that facilitate the droplet to fibril transition.

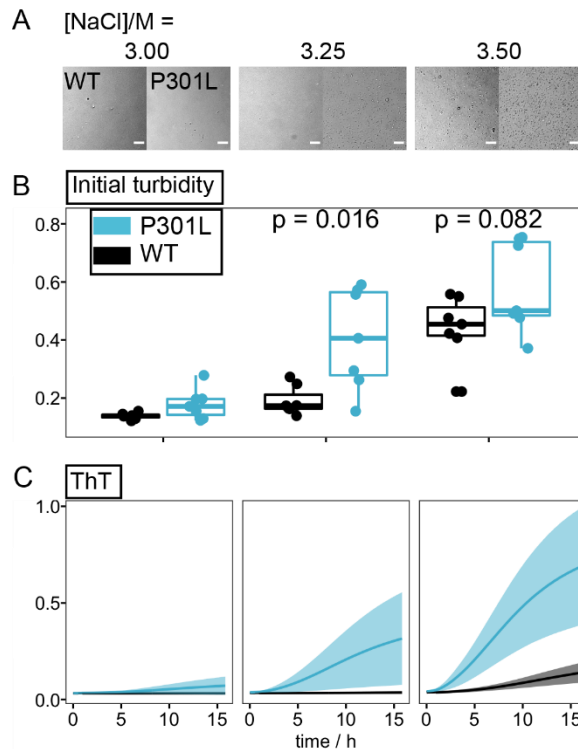


Figure 4-6. Effects of P301L mutation on LLPS and amyloid aggregation of tau at high salt concentration.

A. Representative microscope images of tau187 Cysless and CyslessP301L mutants at varying [NaCl]. **B.** Turbidity of corresponding samples in A. **C.** ThT fluorescence of samples in A after overnight incubation at room temperature. ThT fluorescence was scaled by a constant throughout the manuscript. Ribbons in C show standard deviation of readings from 5 different batches of proteins.

Discussion

Protein liquid-liquid phase separation in pathological contexts have led to intense investigation in the recent past. In particular, tau LLPS has been studied in several reports leading to contrasting hypothesis whether or not LLPS directly triggers amyloid aggregation. We address in this study two key questions: (1) Is tau LLPS of a universal type or could

droplets formed in different conditions possess different properties? (2) Is there a direct cause-and-effect relationship between LLPS and aggregation?

In this report, we have shown that tau at high salt concentration is capable of forming LLPS (referred to as LLPS-HS) driven by hydrophobic interactions. High NaCl concentrations both screen electrostatic interactions and sequester water away from the protein, thereby amplify the effect of hydrophobic association of tau. The concentration of salt needed to achieve LLPS of tau of the order of ~3M is not physiological by any means. However, the influence of such condition on the proteins or biopolymers, i.e. strong electrostatic screening and amplified hydrophobic attraction can easily represent physiologically relevant state. For example, tau under conditions of significant phosphorylation and acetylation would experience effects similar to that of screening the net positive charge effects of the many lysine residues lining on the tau surface, while strong hydrophobic attraction was proposed to be at the origin of hyperphosphorylated tau aggregation [263].

Using EPR spectroscopy, FILM and biochemical assays, we showed that LLPS-HS exhibit slowed local dynamics, restricted water accessibility, elevated microviscosity, as well as irreversible maturation, in stark contrast to electrostatically driven LLPS-ED. Many different conditions can facilitate tau LLPS, but this study shows that the classification of hydrophobically or electrostatically driven LLPS might be an effective framework to classify tau droplets and predict their properties or effects on aggregation. We used tau-RNA complex coacervation to showcase LLPS-ED, but as shown in **Figure 1D** and elsewhere [68], [71], both complex and simple coacervation can form LLPS-ED.

Establishing a causal relationship between LLPS and protein aggregation is challenging because the two processes can occur under identical conditions without necessarily being dependent [23]. Importantly, under conditions where both phenomena occur, it is tempting to deduce a cause-and-effect relationship. Firstly, droplets can form and dissolve within seconds to minutes, while aggregation occurs on the timescale of hours to days, therefore the sequential occurrence of droplets then aggregates does not necessarily imply LLPS is an intermediate state towards aggregation. Secondly, droplets, by definition, increase protein concentration. Therefore, even if both phenomena were completely independent, one would observe aggregates slowly forming in the inside of pre-existing droplets, merely because it is where the protein is, which might lead to the wrong conclusion that droplets directly *trigger* aggregation. In our opinion, a robust way to establish causation between droplets and aggregates is to examine multiple conditions across the LLPS phase boundary, and correlate the changes of droplet volume to the change of fibril mass. Using this approach, we have shown in [23] that although tau-cofactor LLPS-ED and amyloid aggregation are concomitant in many conditions, they are biophysically independent processes. In this study, we show that hydrophobically driven LLPS-HS is different, and that LLPS-HS of tau trigger amyloid formation (**Figure 4-3C** and **Figure 4-3-figure supplement 3**).

Previous reports on tau LLPS made with K18 at low salt concentrations showed that the droplets were dissolved above ~200 mM NaCl and at 3 % HD, suggesting that a combination of electrostatic and hydrophobic driving forces were holding the liquid condensed state together [121], [245]. These droplets were not reported to evolve spontaneously to ThT-active

species. In contrast, droplets formed by hyperphosphorylated 2N4R in Wegmann *et al.* [124] were shown to evolve to amyloid fibrils and to be insensitive to $[\text{NaCl}] > 1\text{M}$, but to be sensitive to 10% HD, showing that they are driven mostly by hydrophobic interactions. These results together with our work suggest a general mechanism that hydrophobically-driven droplets promote aggregation.

We have shown that the local environment in the high salt droplets is drastically different from the one in tau LLPS-ED droplets. FLIM showed that, initially after high salt droplet formation, i.e. even in the absence of significant aging, the micro-viscosity is significantly higher in LLPS-HS than in LLPS-ED droplets. Furthermore, ESEEM and ODNP measurements revealed that water accessibility and water dynamics is significantly more retarded in LLPS-HS than in LLPS-ED. These properties found in LLPS-HS are favorable to protein aggregation because amyloid formation requires a critical step of dehydration, where even hydrophilic residue must give up their ideal hydration to pack into cross- β sheets and steric zippers. Besides, amyloid fibers form a solid-like matrix of high viscosity. We suggest that the features of high viscosity, perturbed protein dynamics and dehydration are general hallmarks of protein LLPS on-pathway to aggregation.

Cw EPR lineshape analysis provides a mechanistic view of tau aggregation through LLPS-HS. We found that increasing the concentration of salt progressively triggers the formation of high order oligomers, as evidenced by a long rotational correlation time of the spin labels tethered to tau. These oligomers are observed even at medium $[\text{NaCl}]$ (e.g. 1.5 M) where droplets are not present. An analysis of the dipolar broadening of the cwEPR spectra

(**Figure 4-5-figure supplement 4**) shows the absence of specific packing (such as in-register cross- β sheets or steric zipper structures) in these ThT-inactive oligomers. LLPS seems however necessary and sufficient to convert these oligomers into ThT-active species and eventually amyloid fibers, as shown by the direct correlation between ThT fluorescence and droplet amount (**Figure 4-3C**).

Finally, we demonstrate that the disease-associated mutation P301L promotes both LLPS-HS and amyloid formation (**Figure 4-6**). Conversely, P301L mutation has no influence on the formation of LLPS-ED [23]. Therefore, we can conclude that P301L mutation promotes intermolecular hydrophobic interactions that drives LLPS-HS. Furthermore, the correlation plots shown in **Figure 4-3C** and **Figure 4-6-figure supplement 2C** show that at similar droplet quantity, P301L mutant will form greater quantity of ThT active species, and does so more rapidly than tau WT. The aggregation-promoting effect of P301L is well known and elegant explanations have been suggested recently [262, p. 201]. Here, we show that the P301L mutation exerts two seemingly independent effects that both ultimately increase aggregation: (i) It promotes local hydrophobic interactions, thereby promoting hydrophobically-driven phase separation, which in turn triggers aggregation and (ii) promotes aggregation-prone conformations, in particular by exposing amyloidogenic segments PHF6(*), independently of LLPS formation. Other disease-related mutations might not combine these effects, because they do not modulate the accessibility of the hydrophobic PHF6(*) segments, explaining why P301L is particularly potent at promoting fibril formation under wide experimental conditions, from *in vitro*, in cells and *in vivo* mouse models.

In conclusion, this study uncovers that there is a clear cause-effect relationship between LLPS and aggregation of tau, only when LLPS is driven by hydrophobic association of tau that we found to be preceded by dehydration of its interfacial water. Different physical or biological factors can drive hydrophobically driven LLPS. While this study showcases the principle by relying on dehydration-promoting salting-out mechanisms induced at high [NaCl] concentration, we posit that hydrophobically driven LLPS can be exerted by many other factors of pathological significance, including the posttranslational modification of tau that can mute the strong positive surface charge density from the abundant lysine residues on tau, e.g. by acetylation and phosphorylation, or enhanced intracellular osmotic crowding pressure, as well as certain pathological mutations of tau, with P301L representing one prominent example. Hence, the liquid condensed state of tau that can be seen *in vitro* and intra cellularly may be a mediating mechanism by which tau can be sequestered and initially protected from aggregation if LLPS can be reversed, or is inadvertently and irreversibly on pathway towards a pathological state.

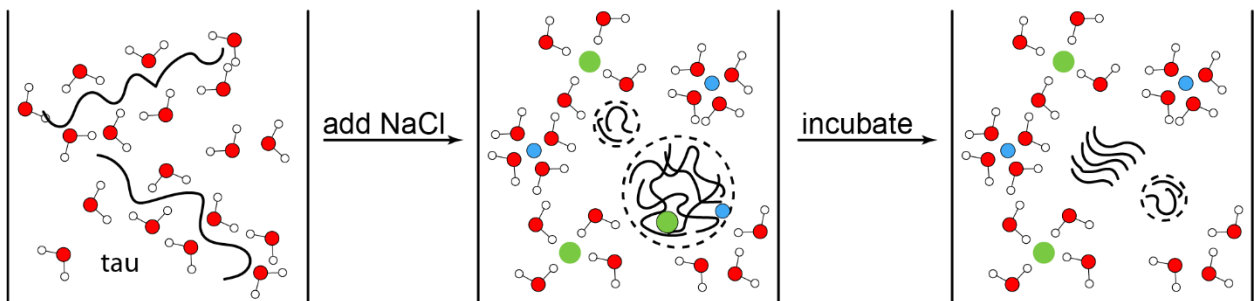


Figure 4-7. Schematic diagram of dehydration-driven droplet-to-fibril transition.

Figure S1 and Tables

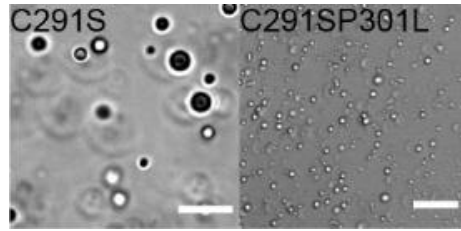


Figure 4-1-figure supplement 1. Microscope images of LLPS-high salt of various tau constructs. 450 μ M Tau187C291S with 2.2 M NaCl; 100 μ M tau187C291SP301L with 3.0 M NaCl.

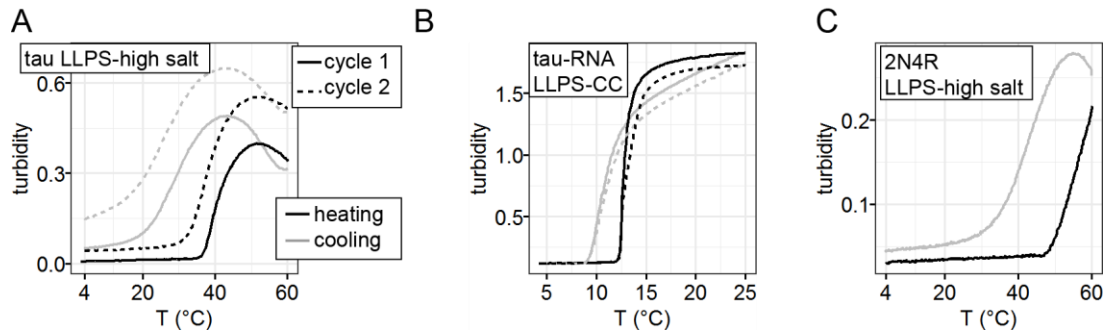


Figure 2-figure supplement 1. Temperature dependence of LLPS-HS. **A.** turbidity of tau187 LLPS-high salt upon heating-cooling cycles. 34 μ M tau187 and 3.5M NaCl was used. **B.** turbidity of tau187-RNA LLPS-CC upon heating-cooling cycles. 100 μ M tau187 with 300 μ g/mL PolyU RNA and 30 mM NaCl was used. **C.** turbidity of 2N4R LLPS-high salt upon heating-cooling cycle. 20 μ M tau with 3.5M NaCl was used. Samples were pre-cooled to 4 $^{\circ}$ C, heated to 25 or 60 $^{\circ}$ C then cooled back to 4 $^{\circ}$ C (cycle 1, solid lines). A second cycle immediately follows (cycle 2, dashed lines). The rate of both heating and cooling are 4 $^{\circ}$ C/min in A and C, and 1 $^{\circ}$ C/min at B.

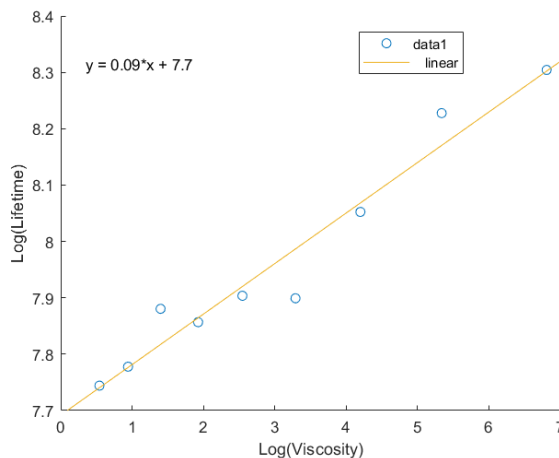


Figure 2-figure supplement 2. Calibration and Fit of Fluorescent Lifetimes to a Glycerol Standard Curve. 4 μM 2N4R conjugated the BODIPY was placed in solutions of glycerol concentrations in ddH₂O ranging from 20-100%. FLIM measurements of the solutions were made and the resulting gaussians were fit and extracted in FLIMFit. The gaussians were fit and the mean values were plotted on a log/log scale against the corresponding solutions viscosity. The data was fit to the Förster Hoffman equation,

$$\log \tau = \log \frac{z}{k_0} + x \log \eta$$

Where τ is the lifetime in ps, $\log \frac{z}{k_0}$ is treated as a variable, x is the slope, and η is the viscosity in centipoise. Fitting the data gave an equation of the form $y = 0.09x + 7.7$.

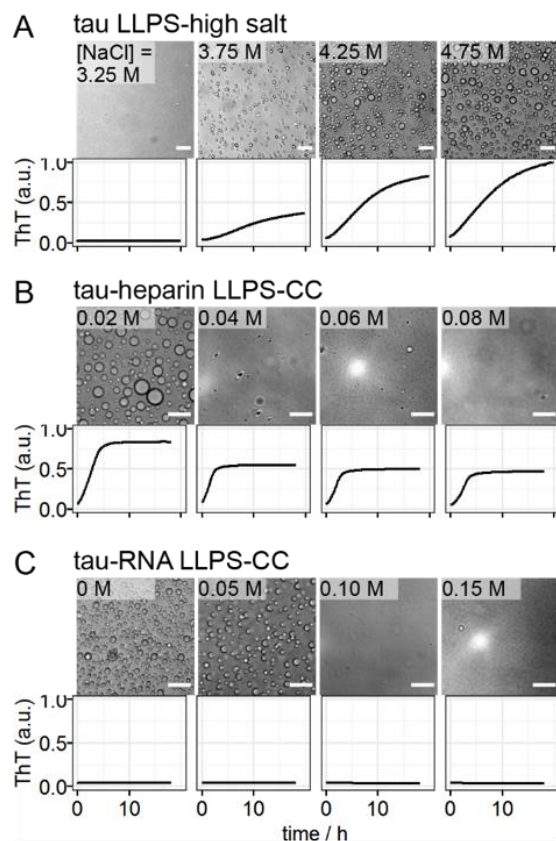


Figure 3-figure supplement 1. Representative microscope images and ThT fluorescence at room temperature overnight of tau LLPS-high salt, tau-heparin LLPS-CC, tau-RNA LLPS-CC at various [NaCl]. 44 μ M tau187, 73 μ g/mL heparin and 132 μ g/mL RNA were used.

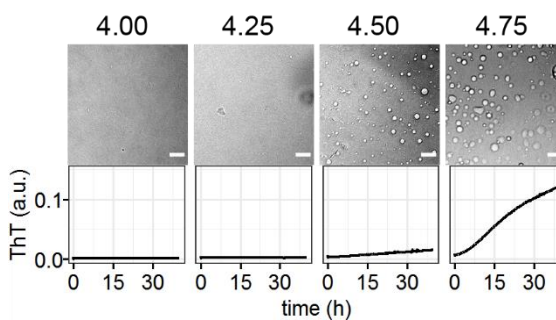


Figure 3-figure supplement 2. Correlation of LLPS-high salt and amyloid aggregation of 2N4R. 20 μ M 2N4R was incubated with varying [NaCl]. Microscope images were taken 10 minutes after mixing while ThT fluorescence readings were recorded overnight. Scale bar length was 25 μ m.

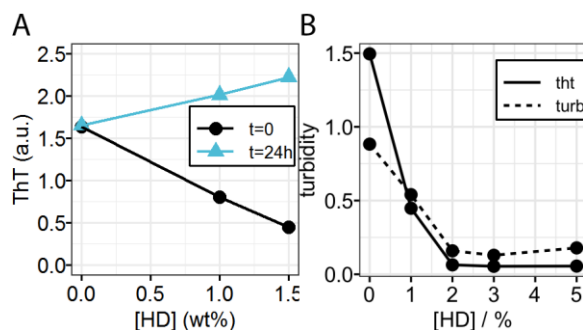


Figure 3-figure supplement 3. Hexanediol dependence of ThT fluorescence and turbidity of LLPS-HS. **A.** Varying concentration of 1,6-hexanediol were added to fresh LLPS-HS sample ($t=0$) and matured LLPS-HS sample ($t=24\text{h}$). After hexanediol was added, samples were incubated for 24 hours and ThT fluorescence was recorded. **B.** Initial turbidity and final ThT fluorescence of LLPS-HS samples mixed with varying concentration of 1,6-hexanediol. In both A and B, 100 μM tau187 and 3.0 M NaCl were used.

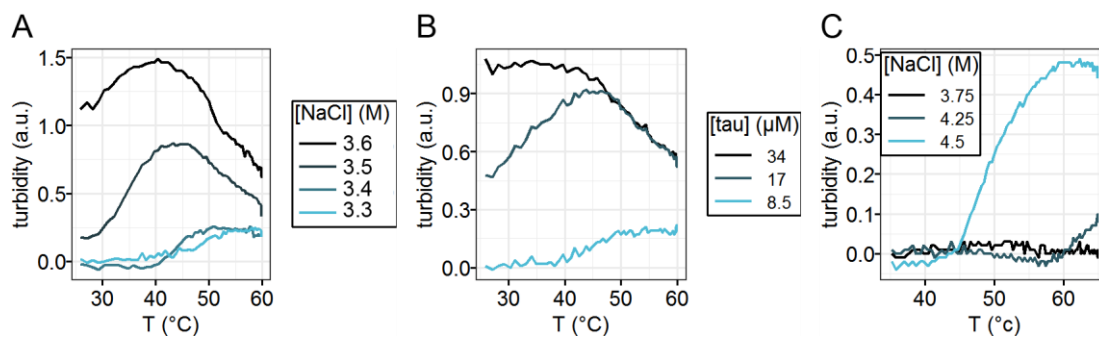


Figure 4-figure supplement 1. LCST behavior of tau LLPS-high salt. **A-B.** turbidity of tau187 LLPS-high salt upon heating at various [NaCl] with 34 μM tau (A) and at varying [tau] with 3.9 M NaCl (B). **C.** Turbidity of 2N4R (C291SC322S) LLPS-high salt upon heating and cooling at various [NaCl]. 20 μM tau was used. In A-C, samples were prepared at room temperature (25 °C) and heated to 65 °C at a rate of $\sim 1^\circ\text{C}/\text{min}$.

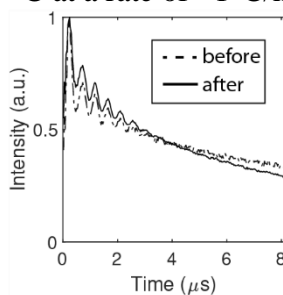


Figure 4-figure supplement 2. 3p-ESEEM data of tau187 upon LLPS-high salt in Figure 4-5B. Signals were scaled to 1 for comparison.

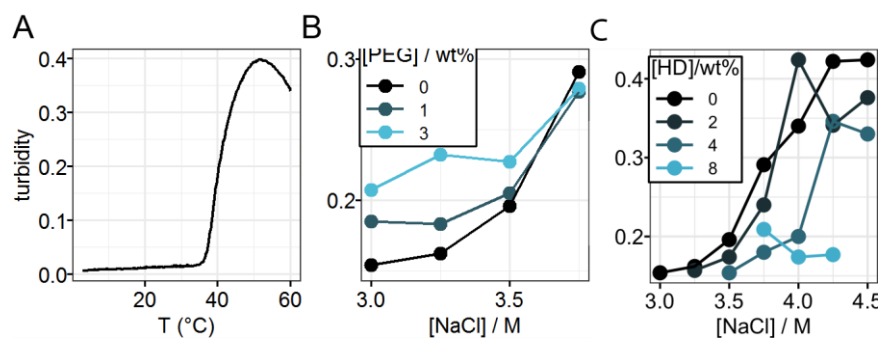


Figure 4-figure supplement 3. Hydrophobic interaction drives tau LLPS-high salt. A Turbidity of tau LLPS-high salt upon heating. 34 μ M tau187 and 3.5 M NaCl was used. Samples were pre-cooled to 4 °C and heated up to 65 °C at a rate of 4 °C/min. **B** Representative turbidity vs [NaCl] of tau LLPS-high salt at varying [PEG]. **C.** Turbidity of tau LLPS-high salt at varying [NaCl] and [HD]. In both B and C, 20 μ M tau187 was used.

site	$k_{\sigma} / \text{mM}^{-1}\text{s}^{-1}$	
	before	after
303	0.031	0.009
313	0.050	0.021
322	0.048	0.023
404	0.056	0.010
4OH-TEMPO	0.092	0.097
322CC	0.050	0.045

Figure 4-source data 1. ODNP measured k_{σ} in Figure 4.

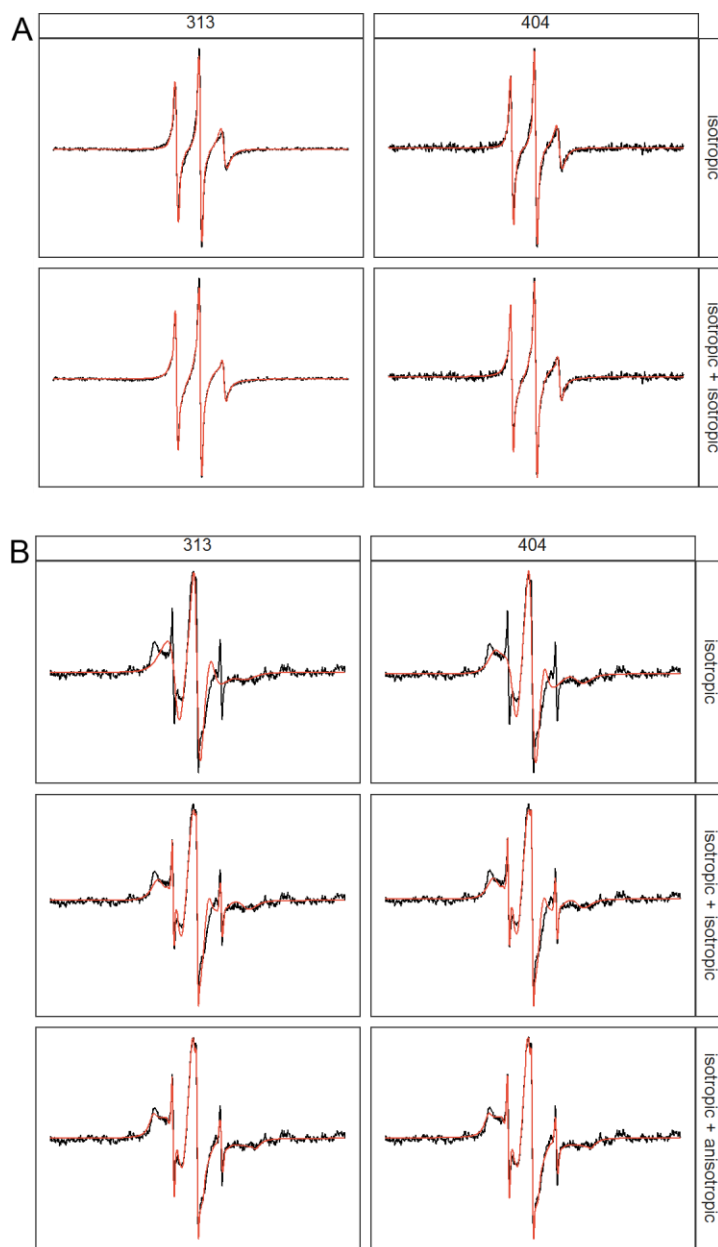


Figure 5-figure supplement 1. Multicomponent and Anisotropic fitting of cwEPR lineshapes. A. Comparison of 1 isotropic component fitting vs 2 isotropic component fitting of tau187 at site 313 and 404 at intermediate [NaCl] of 3.0 M. **B.** Comparison of 1 isotropic, isotropic+isotropic and isotropic+anisotropic components fit of tau187 at site 313 and 404 at very high [NaCl] of 4.5 M.

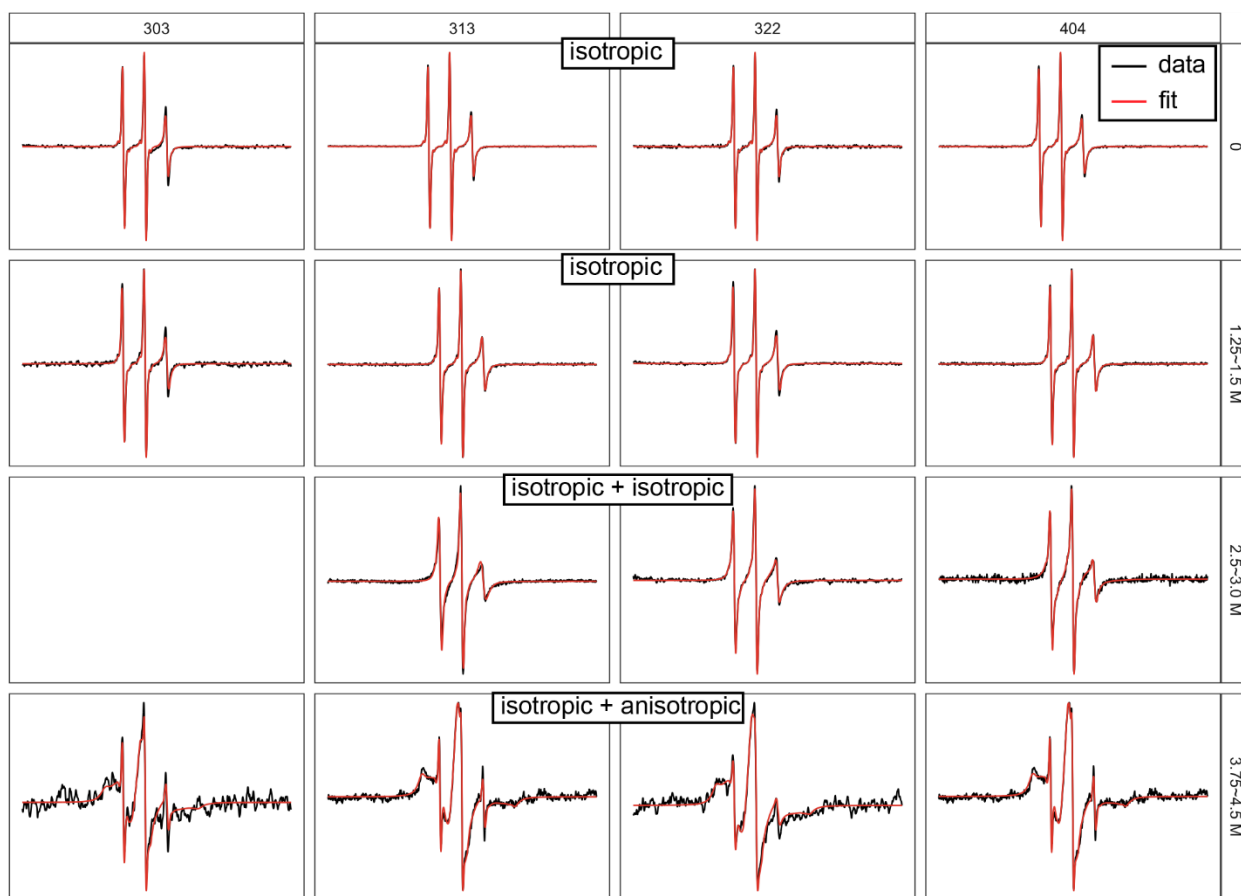


Figure 5-figure supplement 2. Best fit of cwEPR spectra of tau187 at varying sites and varying [NaCl]. Fit results were shown in Figure 4-6B.

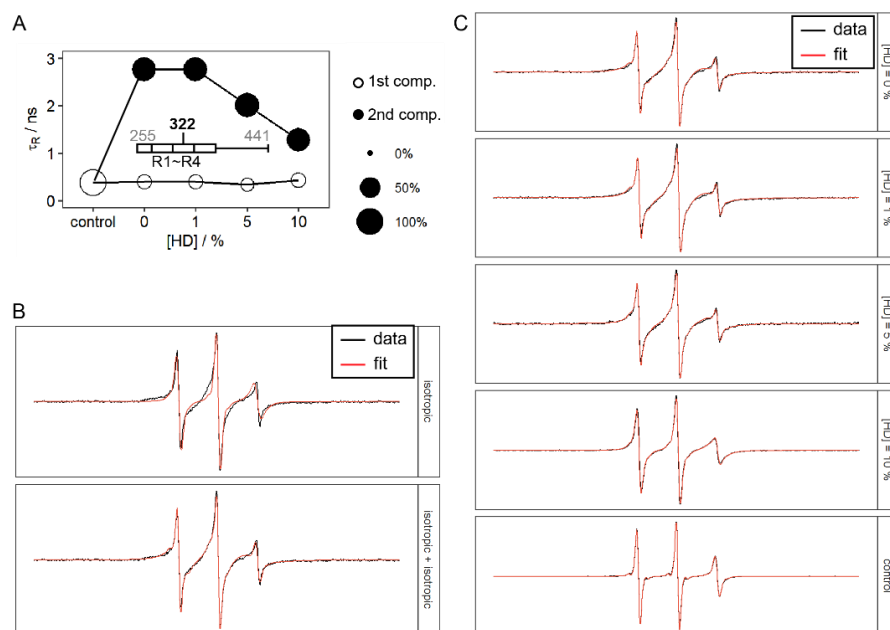


Figure 5-figure supplement 3. Effects of 1,6-hexanediol on tau LLPS-high salt. A. Rotational correlation time of tau LLPS-high salt at varying [HD]. 100 μ M tau187P301LC322SL and 2.5 M NaCl were used. **B.** Comparison of fitting cwEPR lineshape using one component vs two component. [NaCl] = 2.5 M, [HD] = 0. **C.** cwEPR lineshape and fitting results of data in A.

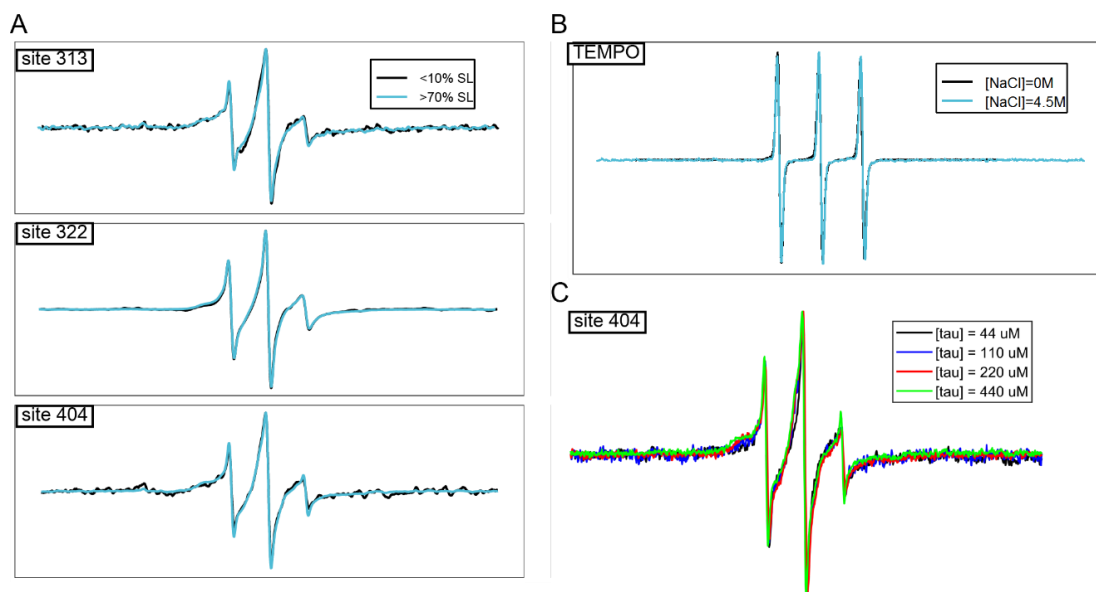


Figure 5-figure supplement 4. Spin dilution and concentration dependence of cwEPR lineshape. In order to gain information on the oligomer structure, we investigated the site-

specific intermolecular interactions by cwEPR. Spin dilution, which consists in mixing 1 spin-labelled tau for 9 non-labeled tau, allows to diminish spin-spin dipolar coupling that could induce EPR lineshape broadening. By comparing cwEPR lineshape of spin-diluted sample vs non-spin-diluted sample, we can determine the population of spins that directly interact within a radius of ~1.5 nm. **A.** Effects of spin dilution on cwEPR lineshape of tau187 at site 313, 322 and 404. 3.0 M NaCl was used. **B.** Effects of 4.5 M NaCl on 4OH-TEMPO cwEPR lineshape. **C.** Effects of concentrations on cwEPR lineshape of tau187 at site 404 at LLPS-HS conditions with 3.0 M NaCl.

site	[NaCl] / M	$t_{R,1}$ / ns	$t_{R,2}$ / ns	p_1 / %	p_2 / %
303	0.00	0.48		100	
	1.25	0.61		100	
	3.75	0.43	1.89	4	96
313	0.00	0.42		100	
	1.50	0.61		100	
	3.00	0.69	2.57	32	68
	4.50	0.34	2.48	3	97
322	0.00	0.47		100	
	1.25	0.65		100	
	2.50	0.68	1.83	40	60
	3.75	0.70	2.08	4	96
404	0.00	0.47		100	
	1.50	0.56		100	
	3.00	0.69	2.77	35	65
	4.50	0.29	2.45	3	97

Figure 5-source data 1. Calculated parameters for cwEPR spectral simulation of tau187 mutants 10 minutes after LLPS at various [NaCl]. Experiment details and fit results were shown in Figure 5B.

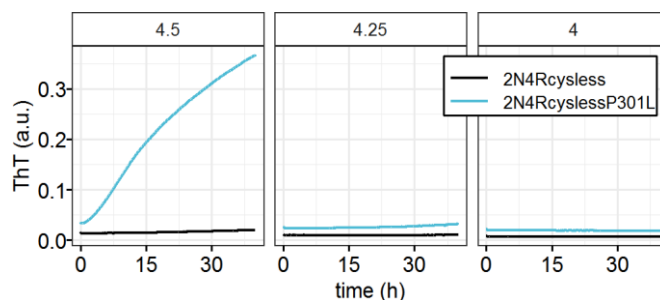


Figure 6-figure supplement 1. Effects of P301L mutation on amyloid aggregation of 2N4R at high salt concentration. 20 μ M 2N4R was used. [NaCl] was shown in panel (unit: M). Samples were incubated at room temperature.

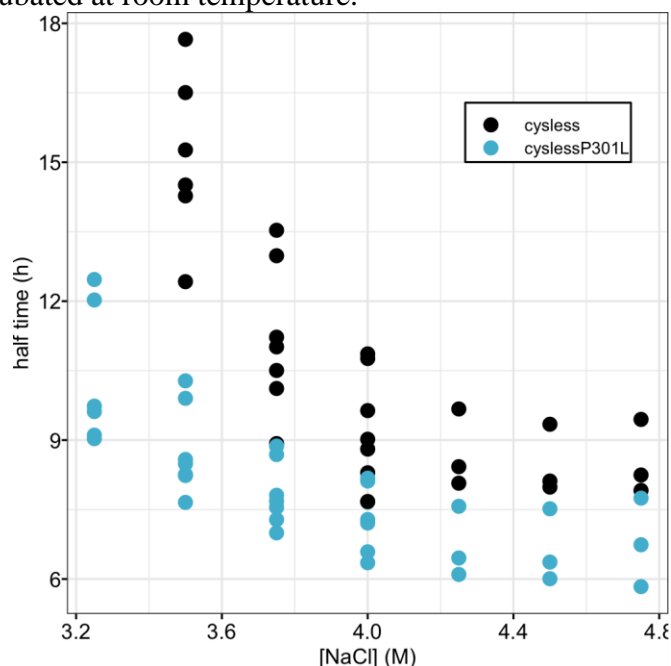


Figure 6-figure supplement 2. Effects of P301L mutation on half time of ThT fluorescence in high salt droplet conditions. ThT fluorescence readings were recorded at varying [NaCl] using 34 μ M tau187C291SC322S (cysless) and tau187C291SC322SP301L (cyslessP301L). Fluorescence readings were fit using a sigmoid function to extract the half time, defined as the time when ThT fluorescence reach half maximum. Data were obtained using $n > 5$ biological independent repeats.

Conclusion and Outlook

Amyloid aggregation of tau irreversibly into insoluble fibrils has been involved in many neurodegenerative diseases. Despite the urgency of understanding disease pathogenesis and developing therapies, the mechanism of tau aggregation is not entirely clear. Recent findings that tau undergoes liquid liquid phase separation make droplets as potential intermediates *en route* to tau fibrils. While droplets implied pathologic aggregation for FUS, hnRNPA1 and other intrinsically disordered proteins, their physical principles are not universal and unclear for tau LLPS. With this in mind, studies in this dissertation build physical models to explain the driving forces for tau LLPS, probe the structure and dynamics of tau and finally determine its impacts on tau amyloid aggregation.

This dissertation sets out to understand cofactor-induced tau aggregation, presented in Chapter 1, I aimed to understand whether at least part of the aggregated fibrils is made of added cofactors or the entire fibril can be cofactor-free. By digesting cofactor using RNase and heparinase, applying site-directed spin labeling and cwEPR spectrum lineshape analysis, we observed that the tau fibrils spontaneously depolymerize and release tau monomers. Results showed that cofactors are essential for stable tau fibrils, which urge future studies to identify relevant cofactors *in vivo*.

With RNA as a relevant binding cofactor of tau *in vivo*, tau is able to undergo LLPS with RNA, which we determined as complex coacervation (LLPS-CC). Chapter 2 aimed at understanding the principles behind tau-RNA LLPS-CC. By using temperature-resolved

turbidimetry and microscopy, tau-RNA LLPS-CC presents a reversible process which is entropically driven. CWEPR lineshape analysis and fluorescence assay show tau in droplets remains solution-like dynamics and free of aggregates. Mapping the phase diagram and fitting with Flory Huggins-based theory as well as Field Theoretic Simulation show tau-RNA LLPS can be described by electrostatic interactions. Meanwhile, we observed certain deviations between theory and experiments, which can result from other electrostatic interactions such as dipole-dipole, cation- π interactions as well as non-electrostatic interactions including potential tau-RNA short range bindings. Current work has not included such effects into considerations and call for future investigation.

Chapter 3 further generalized tau-RNA LLPS-CC to tau-polyanion, and studied relationship between electrostatically driven LLPS-CC and amyloid aggregation. By thoroughly comparing the LLPS-CC and aggregation in terms of molecular conformation before the aggregation, kinetics during aggregation and extent of reaction after aggregation, we found the two processes are independent processes with overlapping conditions. While tau LLPS-CC is expected to occur *in vivo*, its biological function need further illustration. Considering the dynamic and heterogeneous structure of polycation-polyanion CC, the structure basis of such independence needs further investigation. Whether such independence is general to other types of electrostatically driven protein LLPS remains unclear and is further studied in Chapter 4.

By introducing a novel form of tau LLPS, Chapter 4 aimed at studied the roles of hydrophobic interactions on tau LLPS and aggregation. Results showed a distinct contrast

between electrostatically driven and hydrophobically driven tau LLPS, in terms of direct correlation and causation to tau fibril, interference with aggregation-promoting tau mutation and the underlying dynamic of tau molecules. Whether the previous reported tau aggregation in hyperphosphorylated tau droplets and truncated tau droplets is due to hydrophobic interactions needs further studies. The molecular elements of hydrophobically driven tau LLPS and their association with cofactor-induced and phosphorylation-induced/inhibited tau aggregation are still unresolved. In wildest imagination of the author, certain critical hydrophobic hotspots of tau may drive tau LLPS, and the resulting concentrated state of tau in droplets can further facilitate the formation of tau fibrils.

Reference

- [1] P. V. Arriagada, J. H. Growdon, E. T. Hedley-Whyte, and B. T. Hyman, “Neurofibrillary tangles but not senile plaques parallel duration and severity of Alzheimer’s disease,” *Neurology*, vol. 42, no. 3, pp. 631–631, Mar. 1992, doi: 10.1212/WNL.42.3.631.
- [2] D. P. Hanger, B. H. Anderton, and W. Noble, “Tau phosphorylation: the therapeutic challenge for neurodegenerative disease,” *Trends Mol. Med.*, vol. 15, no. 3, pp. 112–119, Mar. 2009, doi: 10.1016/j.molmed.2009.01.003.
- [3] M. Goedert and M. G. Spillantini, “A Century of Alzheimer’s Disease,” *Science*, vol. 314, no. 5800, pp. 777–781, Nov. 2006, doi: 10.1126/science.1132814.
- [4] F. Hernández and J. Avila, “Tauopathies,” *Cell. Mol. Life Sci.*, vol. 64, no. 17, pp. 2219–2233, Sep. 2007, doi: 10.1007/s00018-007-7220-x.
- [5] T. Guo, W. Noble, and D. P. Hanger, “Roles of tau protein in health and disease,” *Acta Neuropathol. (Berl.)*, vol. 133, no. 5, pp. 665–704, 2017, doi: 10.1007/s00401-017-1707-9.
- [6] A. W. P. Fitzpatrick *et al.*, “Cryo-EM structures of tau filaments from Alzheimer’s disease,” *Nature*, vol. advance online publication, Jul. 2017, doi: 10.1038/nature23002.
- [7] B. Falcon *et al.*, “Structures of filaments from Pick’s disease reveal a novel tau protein fold,” *Nature*, vol. 561, no. 7721, pp. 137–140, Sep. 2018, doi: 10.1038/s41586-018-0454-y.
- [8] B. Falcon *et al.*, “Novel tau filament fold in chronic traumatic encephalopathy encloses hydrophobic molecules,” *Nature*, vol. 568, no. 7752, p. 420, Apr. 2019, doi: 10.1038/s41586-019-1026-5.
- [9] W. Zhang *et al.*, “Novel tau filament fold in corticobasal degeneration, a four-repeat tauopathy,” *bioRxiv*, p. 811703, Oct. 2019, doi: 10.1101/811703.
- [10] C. P. Brangwynne *et al.*, “Germline P granules are liquid droplets that localize by controlled dissolution/condensation,” *Science*, vol. 324, no. 5935, pp. 1729–1732, Jun. 2009, doi: 10.1126/science.1172046.
- [11] A. Molliex *et al.*, “Phase Separation by Low Complexity Domains Promotes Stress Granule Assembly and Drives Pathological Fibrillization,” *Cell*, vol. 163, no. 1, pp. 123–133, Sep. 2015, doi: 10.1016/j.cell.2015.09.015.
- [12] A. A. Hyman, C. A. Weber, and F. Jülicher, “Liquid-Liquid Phase Separation in Biology,” *Annu. Rev. Cell Dev. Biol.*, vol. 30, no. 1, pp. 39–58, 2014, doi: 10.1146/annurev-cellbio-100913-013325.
- [13] Y. R. Li, O. D. King, J. Shorter, and A. D. Gitler, “Stress granules as crucibles of ALS pathogenesis,” *J Cell Biol*, vol. 201, no. 3, pp. 361–372, Apr. 2013, doi: 10.1083/jcb.201302044.
- [14] T. Murakami *et al.*, “ALS/FTD Mutation-Induced Phase Transition of FUS Liquid Droplets and Reversible Hydrogels into Irreversible Hydrogels Impairs RNP Granule

- Function,” *Neuron*, vol. 88, no. 4, pp. 678–690, Nov. 2015, doi: 10.1016/j.neuron.2015.10.030.
- [15] A. Patel *et al.*, “A Liquid-to-Solid Phase Transition of the ALS Protein FUS Accelerated by Disease Mutation,” *Cell*, vol. 162, no. 5, pp. 1066–1077, Aug. 2015, doi: 10.1016/j.cell.2015.07.047.
- [16] M. Kato *et al.*, “Cell-free formation of RNA granules: low complexity sequence domains form dynamic fibers within hydrogels,” *Cell*, vol. 149, no. 4, pp. 753–767, May 2012, doi: 10.1016/j.cell.2012.04.017.
- [17] H.-R. Li, W.-C. Chiang, P.-C. Chou, W.-J. Wang, and J. Huang, “TAR DNA-binding protein 43 (TDP-43) liquid-liquid phase separation is mediated by just a few aromatic residues,” *J. Biol. Chem.*, p. jbc.AC117.001037, Mar. 2018, doi: 10.1074/jbc.AC117.001037.
- [18] I. Kwon *et al.*, “Poly-dipeptides encoded by the C9orf72 repeats bind nucleoli, impede RNA biogenesis, and kill cells,” *Science*, vol. 345, no. 6201, pp. 1139–1145, Sep. 2014, doi: 10.1126/science.1254917.
- [19] K.-H. Lee *et al.*, “C9orf72 Dipeptide Repeats Impair the Assembly, Dynamics, and Function of Membrane-Less Organelles,” *Cell*, vol. 167, no. 3, pp. 774–788.e17, Oct. 2016, doi: 10.1016/j.cell.2016.10.002.
- [20] S. Boeynaems *et al.*, “Phase Separation of C9orf72 Dipeptide Repeats Perturbs Stress Granule Dynamics,” *Mol. Cell*, vol. 65, no. 6, pp. 1044–1055.e5, Mar. 2017, doi: 10.1016/j.molcel.2017.02.013.
- [21] T. J. Nott *et al.*, “Phase Transition of a Disordered Nuage Protein Generates Environmentally Responsive Membraneless Organelles,” *Mol. Cell*, vol. 57, no. 5, pp. 936–947, Mar. 2015, doi: 10.1016/j.molcel.2015.01.013.
- [22] X. Zhang *et al.*, “RNA Stores Tau Reversibly in Complex Coacervates,” *bioRxiv*, p. 111245, Feb. 2017, doi: 10.1101/111245.
- [23] Y. Lin, Y. Fichou, Z. Zeng, N. Y. Hu, and S. Han, “Electrostatically Driven Complex Coacervation and Amyloid Aggregation of Tau Are Independent Processes with Overlapping Conditions,” *ACS Chem. Neurosci.*, Jan. 2020, doi: 10.1021/acscchemneuro.9b00627.
- [24] M. Goedert, R. Jakes, M. G. Spillantini, M. Hasegawa, M. J. Smith, and R. A. Crowther, “Assembly of microtubule-associated protein tau into Alzheimer-like filaments induced by sulphated glycosaminoglycans,” *Nature*, vol. 383, no. 6600, pp. 550–553, Oct. 1996, doi: 10.1038/383550a0.
- [25] T. Kampers, P. Friedhoff, J. Biernat, E. M. Mandelkow, and E. Mandelkow, “RNA stimulates aggregation of microtubule-associated protein tau into Alzheimer-like paired helical filaments,” *FEBS Lett.*, vol. 399, no. 3, pp. 344–349, Dec. 1996.
- [26] B. B. Holmes *et al.*, “Heparan sulfate proteoglycans mediate internalization and propagation of specific proteopathic seeds,” *Proc. Natl. Acad. Sci.*, vol. 110, no. 33, pp. E3138–E3147, Aug. 2013, doi: 10.1073/pnas.1301440110.

- [27] A. Maïza *et al.*, “The role of heparan sulfates in protein aggregation and their potential impact on neurodegeneration,” *FEBS Lett.*, vol. 0, no. 0, doi: 10.1002/1873-3468.13082.
- [28] T. Mitchison and M. Kirschner, “Cytoskeletal dynamics and nerve growth,” *Neuron*, vol. 1, no. 9, pp. 761–772, Nov. 1988, doi: 10.1016/0896-6273(88)90124-9.
- [29] M. W. Kirschner and T. Mitchison, “Microtubule dynamics,” *Nature*, vol. 324, no. 6098, p. 621, Dec. 1986, doi: 10.1038/324621a0.
- [30] M. D. Weingarten, A. H. Lockwood, S. Y. Hwo, and M. W. Kirschner, “A protein factor essential for microtubule assembly,” *Proc. Natl. Acad. Sci. U. S. A.*, vol. 72, no. 5, pp. 1858–1862, May 1975.
- [31] J. Q. Trojanowski, T. Schuck, M. L. Schmidt, and V. M. Lee, “Distribution of tau proteins in the normal human central and peripheral nervous system,” *J. Histochem. Cytochem. Off. J. Histochem. Soc.*, vol. 37, no. 2, pp. 209–215, Feb. 1989, doi: 10.1177/37.2.2492045.
- [32] J. Q. Trojanowski, A. B. Smith, D. Huryn, and V. M.-Y. Lee, “Microtubule-stabilising drugs for therapy of Alzheimer’s disease and other neurodegenerative disorders with axonal transport impairments,” *Expert Opin. Pharmacother.*, vol. 6, no. 5, pp. 683–686, May 2005, doi: 10.1517/14656566.6.5.683.
- [33] T. Vanderweyde *et al.*, “Interaction of tau with the RNA-Binding Protein TIA1 Regulates tau Pathophysiology and Toxicity,” *Cell Rep.*, vol. 15, no. 7, pp. 1455–1466, May 2016, doi: 10.1016/j.celrep.2016.04.045.
- [34] A. Gauthier-Kemper *et al.*, “The frontotemporal dementia mutation R406W blocks tau’s interaction with the membrane in an annexin A2-dependent manner,” *J. Cell Biol.*, vol. 192, no. 4, pp. 647–661, Feb. 2011, doi: 10.1083/jcb.201007161.
- [35] A. Sultan *et al.*, “Nuclear Tau, a Key Player in Neuronal DNA Protection,” *J. Biol. Chem.*, vol. 286, no. 6, pp. 4566–4575, Feb. 2011, doi: 10.1074/jbc.M110.199976.
- [36] M. Violet *et al.*, “A major role for Tau in neuronal DNA and RNA protection in vivo under physiological and hyperthermic conditions,” *Front. Cell. Neurosci.*, vol. 8, Mar. 2014, doi: 10.3389/fncel.2014.00084.
- [37] M. Bukar Maina, Y. Al-Hilaly, and L. Serpell, “Nuclear Tau and Its Potential Role in Alzheimer’s Disease,” *Biomolecules*, vol. 6, no. 1, p. 9, Jan. 2016, doi: 10.3390/biom6010009.
- [38] A. Andreadis, “Tau Splicing and the Intricacies of Dementia,” *J. Cell. Physiol.*, vol. 227, no. 3, pp. 1220–1225, Mar. 2012, doi: 10.1002/jcp.22842.
- [39] G. Lippens *et al.*, “NMR Meets Tau: Insights into Its Function and Pathology,” *Biomolecules*, vol. 6, no. 2, p. 28, Jun. 2016, doi: 10.3390/biom6020028.
- [40] C. Despres *et al.*, “Identification of the Tau phosphorylation pattern that drives its aggregation,” *Proc. Natl. Acad. Sci.*, vol. 114, no. 34, pp. 9080–9085, Aug. 2017, doi: 10.1073/pnas.1708448114.
- [41] A. C. Alonso, I. Grundke-Iqbal, and K. Iqbal, “Alzheimer’s disease hyperphosphorylated tau sequesters normal tau into tangles of filaments and disassembles microtubules,” *Nat. Med.*, vol. 2, no. 7, pp. 783–787, Jul. 1996.

- [42] A. Alonso, T. Zaidi, M. Novak, I. Grundke-Iqbal, and K. Iqbal, "Hyperphosphorylation induces self-assembly of tau into tangles of paired helical filaments/straight filaments," *Proc. Natl. Acad. Sci. U. S. A.*, vol. 98, no. 12, pp. 6923–6928, Jun. 2001, doi: 10.1073/pnas.121119298.
- [43] M. Haj-Yahya, P. Gopinath, K. Rajasekhar, H. Mirbaha, M. I. Diamond, and H. A. Lashuel, "Site-Specific Hyperphosphorylation Inhibits, Rather than Promotes, Tau Fibrillization, Seeding Capacity, and Its Microtubule Binding," *Angew. Chem.*, vol. 132, no. 10, pp. 4088–4096, 2020, doi: 10.1002/ange.201913001.
- [44] M. G. Spillantini, J. R. Murrell, M. Goedert, M. R. Farlow, A. Klug, and B. Ghetti, "Mutation in the tau gene in familial multiple system tauopathy with presenile dementia," *Proc. Natl. Acad. Sci.*, vol. 95, no. 13, pp. 7737–7741, Jun. 1998, Accessed: May 17, 2017. [Online]. Available: <http://www.pnas.org/content/95/13/7737>.
- [45] A. Huang and C. M. Stultz, "The Effect of a Δ K280 Mutation on the Unfolded State of a Microtubule-Binding Repeat in Tau," *PLoS Comput. Biol.*, vol. 4, no. 8, p. e1000155, Aug. 2008, doi: 10.1371/journal.pcbi.1000155.
- [46] M. Lu and K. S. Kosik, "Competition for Microtubule-binding with Dual Expression of Tau Missense and Splice Isoforms," *Mol. Biol. Cell*, vol. 12, no. 1, pp. 171–184, Jan. 2001, Accessed: May 14, 2020. [Online]. Available: <https://www.ncbi.nlm.nih.gov/pmc/articles/PMC30576/>.
- [47] S. S. Shafiei, M. J. Guerrero-Muñoz, and D. L. Castillo-Carranza, "Tau Oligomers: Cytotoxicity, Propagation, and Mitochondrial Damage," *Front. Aging Neurosci.*, vol. 9, 2017, doi: 10.3389/fnagi.2017.00083.
- [48] N. A. Eschmann *et al.*, "Signature of an aggregation-prone conformation of tau," *Sci. Rep.*, vol. 7, p. 44739, Mar. 2017, doi: 10.1038/srep44739.
- [49] B. Falcon *et al.*, "Conformation Determines the Seeding Potencies of Native and Recombinant Tau Aggregates," *J. Biol. Chem.*, vol. 290, no. 2, pp. 1049–1065, Jan. 2015, doi: 10.1074/jbc.M114.589309.
- [50] O. A. Morozova, Z. M. March, A. S. Robinson, and D. W. Colby, "Conformational Features of Tau Fibrils from Alzheimer's Disease Brain Are Faithfully Propagated by Unmodified Recombinant Protein," *Biochemistry*, vol. 52, no. 40, pp. 6960–6967, Oct. 2013, doi: 10.1021/bi400866w.
- [51] V. Meyer, P. D. Dinkel, E. Rickman Hager, and M. Margittai, "Amplification of Tau Fibrils from Minute Quantities of Seeds," *Biochemistry*, vol. 53, no. 36, pp. 5804–5809, Sep. 2014, doi: 10.1021/bi501050g.
- [52] F. Clavaguera, J. Hench, M. Goedert, and M. Tolnay, "Invited review: Prion-like transmission and spreading of tau pathology," *Neuropathol. Appl. Neurobiol.*, vol. 41, no. 1, pp. 47–58, Feb. 2015, doi: 10.1111/nan.12197.
- [53] B. Frost, R. L. Jacks, and M. I. Diamond, "Propagation of tau misfolding from the outside to the inside of a cell," *J. Biol. Chem.*, vol. 284, no. 19, pp. 12845–12852, May 2009, doi: 10.1074/jbc.M808759200.

- [54] B. B. Holmes *et al.*, “Proteopathic tau seeding predicts tauopathy in vivo,” *Proc. Natl. Acad. Sci. U. S. A.*, vol. 111, no. 41, pp. E4376–4385, Oct. 2014, doi: 10.1073/pnas.1411649111.
- [55] A. M. Sharma, T. L. Thomas, D. R. Woodard, O. M. Kashmer, and M. I. Diamond, “Tau monomer encodes strains,” *eLife*, vol. 7, p. e37813, Dec. 2018, doi: 10.7554/eLife.37813.
- [56] F. Clavaguera *et al.*, “Transmission and spreading of tauopathy in transgenic mouse brain,” *Nat. Cell Biol.*, vol. 11, no. 7, pp. 909–913, Jul. 2009, doi: 10.1038/ncb1901.
- [57] P. Anderson and N. Kedersha, “RNA granules,” *J. Cell Biol.*, vol. 172, no. 6, pp. 803–808, Mar. 2006, doi: 10.1083/jcb.200512082.
- [58] W. M. Aumiller, F. Pir-Cakmak, B. W. Davis, and C. D. Keating, “RNA-based coacervates as a model for membraneless organelles: Formation, properties, and interfacial liposome assembly,” *Langmuir ACS J. Surf. Colloids*, Sep. 2016, doi: 10.1021/acs.langmuir.6b02499.
- [59] C. P. Brangwynne, T. J. Mitchison, and A. A. Hyman, “Active liquid-like behavior of nucleoli determines their size and shape in *Xenopus laevis* oocytes,” *Proc. Natl. Acad. Sci. U. S. A.*, vol. 108, no. 11, pp. 4334–4339, Mar. 2011, doi: 10.1073/pnas.1017150108.
- [60] J. R. Buchan, J.-H. Yoon, and R. Parker, “Stress-specific composition, assembly and kinetics of stress granules in *Saccharomyces cerevisiae*,” *J. Cell Sci.*, vol. 124, no. Pt 2, pp. 228–239, Jan. 2011, doi: 10.1242/jcs.078444.
- [61] W. M. Babinchak *et al.*, “The role of liquid-liquid phase separation in aggregation of the TDP-43 low-complexity domain,” *J. Biol. Chem.*, vol. 294, no. 16, pp. 6306–6317, Apr. 2019, doi: 10.1074/jbc.RA118.007222.
- [62] L. Li *et al.*, “Real-time imaging of Huntingtin aggregates diverting target search and gene transcription,” *eLife*, vol. 5, p. e17056, Aug. 2016, doi: 10.7554/eLife.17056.
- [63] S. Elbaum-Garfinkle and C. P. Brangwynne, “Liquids, Fibers, and Gels: The Many Phases of Neurodegeneration,” *Dev. Cell*, vol. 35, no. 5, pp. 531–532, Dec. 2015, doi: 10.1016/j.devcel.2015.11.014.
- [64] S. L. Crick, K. M. Ruff, K. Garai, C. Frieden, and R. V. Pappu, “Unmasking the roles of N- and C-terminal flanking sequences from exon 1 of huntingtin as modulators of polyglutamine aggregation,” *Proc. Natl. Acad. Sci. U. S. A.*, vol. 110, no. 50, pp. 20075–20080, Dec. 2013, doi: 10.1073/pnas.1320626110.
- [65] C. P. Brangwynne, P. Tompa, and R. V. Pappu, “Polymer physics of intracellular phase transitions,” *Nat. Phys.*, vol. 11, no. 11, pp. 899–904, Nov. 2015, doi: 10.1038/nphys3532.
- [66] H. T. Tran, A. Mao, and R. V. Pappu, “Role of Backbone–Solvent Interactions in Determining Conformational Equilibria of Intrinsically Disordered Proteins,” *J. Am. Chem. Soc.*, vol. 130, no. 23, pp. 7380–7392, Jun. 2008, doi: 10.1021/ja710446s.
- [67] S. Elbaum-Garfinkle *et al.*, “The disordered P granule protein LAF-1 drives phase separation into droplets with tunable viscosity and dynamics,” *Proc. Natl. Acad. Sci. U. S. A.*, vol. 112, no. 23, pp. 7189–7194, Jun. 2015, doi: 10.1073/pnas.1504822112.

- [68] S. Boyko, X. Qi, T.-H. Chen, K. Surewicz, and W. K. Surewicz, "Liquid-liquid phase separation of tau protein: The crucial role of electrostatic interactions," *J. Biol. Chem.*, p. jbc.AC119.009198, May 2019, doi: 10.1074/jbc.AC119.009198.
- [69] P. Li *et al.*, "Phase transitions in the assembly of multivalent signalling proteins," *Nature*, vol. 483, no. 7389, pp. 336–340, Mar. 2012, doi: 10.1038/nature10879.
- [70] S. Park, S. Kim, Y. Jho, and D. S. Hwang, "Cation- π Interactions and Their Contribution to Mussel Underwater Adhesion Studied Using a Surface Forces Apparatus: A Mini-Review," *Langmuir*, Aug. 2019, doi: 10.1021/acs.langmuir.9b01976.
- [71] V. Singh, L. Xu, S. Boyko, K. Surewicz, and W. K. Surewicz, "Zinc promotes liquid-liquid phase separation of tau protein," *J. Biol. Chem.*, p. jbc.AC120.013166, Mar. 2020, doi: 10.1074/jbc.AC120.013166.
- [72] E. da S. Gulao, C. J. F. de Souza, C. T. Andrade, and E. E. Garcia-Rojas, "Complex coacervates obtained from peptide leucine and gum arabic: Formation and characterization," *Food Chem.*, vol. 194, pp. 680–686, Mar. 2016, doi: 10.1016/j.foodchem.2015.08.062.
- [73] L. Zhang, V. Lipik, and A. Miserez, "Complex coacervates of oppositely charged copolypeptides inspired by the sandcastle worm glue," *J Mater Chem B*, vol. 4, no. 8, pp. 1544–1556, 2016, doi: 10.1039/C5TB02298C.
- [74] C. J. F. Souza, E. E. Garcia Rojas, N. R. Melo, A. Gaspar, and J. F. C. Lins, "Complex coacervates obtained from interaction egg yolk lipoprotein and polysaccharides," *Food Hydrocoll.*, vol. 30, no. 1, pp. 375–381, Jan. 2013, doi: 10.1016/j.foodhyd.2012.06.012.
- [75] S. G. Anema and C. G. de Kruif, "Complex coacervates of lactotransferrin and beta-lactoglobulin," *J. Colloid Interface Sci.*, vol. 430, pp. 214–220, Sep. 2014, doi: 10.1016/j.jcis.2014.05.036.
- [76] N. Arfin, V. K. Aswal, and H. B. Bohidar, "Overcharging, thermal, viscoelastic and hydration properties of DNA-gelatin complex coacervates: pharmaceutical and food industries," *Rsc Adv.*, vol. 4, no. 23, pp. 11705–11713, 2014, doi: 10.1039/c3ra46618c.
- [77] C. Schmitt, L. Aberkane, and C. Sanchez, "Protein-polysaccharide complexes and coacervates," in *Handbook of Hydrocolloids, 2nd Edition*, G. O. Phillips and P. A. Williams, Eds. Cambridge: Woodhead Publ Ltd, 2009, pp. 420–476.
- [78] S. L. Turgeon, C. Schmitt, and C. Sanchez, "Protein-polysaccharide complexes and coacervates," *Curr. Opin. Colloid Interface Sci.*, vol. 12, no. 4–5, pp. 166–178, Oct. 2007, doi: 10.1016/j.cocis.2007.07.007.
- [79] E. Kizilay, A. B. Kayitmazer, and P. L. Dubin, "Complexation and coacervation of polyelectrolytes with oppositely charged colloids," *Adv. Colloid Interface Sci.*, vol. 167, no. 1–2, pp. 24–37, Sep. 2011, doi: 10.1016/j.cis.2011.06.006.
- [80] F. W. Tiebackx, "Gleichzeitige Ausflockung zweier Kolloide," *Z. Für Chem. Ind. Kolloide*, vol. 8, no. 4, pp. 198–201, Apr. 1911, doi: 10.1007/BF01503532.
- [81] E. Spruijt *et al.*, "Structure and Dynamics of Polyelectrolyte Complex Coacervates Studied by Scattering of Neutrons, X-rays, and Light," *Macromolecules*, vol. 46, no. 11, pp. 4596–4605, Jun. 2013, doi: 10.1021/ma400132s.

- [82] F. Horkay, A.-M. Hecht, and E. Geissler, "Similarities between polyelectrolyte gels and biopolymer solutions," *J. Polym. Sci. Part B Polym. Phys.*, vol. 44, no. 24, pp. 3679–3686, Dec. 2006, doi: 10.1002/polb.21008.
- [83] A. B. Kayitmazer, S. P. Strand, C. Tribet, W. Jaeger, and P. L. Dubin, "Effect of polyelectrolyte structure on protein-polyelectrolyte coacervates: Coacervates of bovine serum albumin with poly(diallyldimethylammonium chloride) versus chitosan," *Biomacromolecules*, vol. 8, no. 11, pp. 3568–3577, Nov. 2007, doi: 10.1021/bm700645t.
- [84] X. Wang, Y. Li, Y.-W. Wang, J. Lal, and Q. Huang, "Microstructure of β -Lactoglobulin/Pectin Coacervates Studied by Small-Angle Neutron Scattering," *J. Phys. Chem. B*, vol. 111, no. 3, pp. 515–520, Jan. 2007, doi: 10.1021/jp0632891.
- [85] F. Weinbreck, R. H. Tromp, and C. G. de Kruif, "Composition and structure of whey protein/gum arabic coacervates," *Biomacromolecules*, vol. 5, no. 4, pp. 1437–1445, Aug. 2004, doi: 10.1021/bm049970v.
- [86] F. Weinbreck, H. S. Rollema, R. H. Tromp, and C. G. de Kruif, "Diffusivity of Whey Protein and Gum Arabic in Their Coacervates," *Langmuir*, vol. 20, no. 15, pp. 6389–6395, Jul. 2004, doi: 10.1021/la049908j.
- [87] J. H. Ortony, D. S. Hwang, J. M. Franck, J. H. Waite, and S. Han, "Asymmetric Collapse in Biomimetic Complex Coacervates Revealed by Local Polymer and Water Dynamics," *Biomacromolecules*, vol. 14, no. 5, pp. 1395–1402, May 2013, doi: 10.1021/bm4000579.
- [88] R. Kausik, A. Srivastava, P. A. Korevaar, G. Stucky, J. H. Waite, and S. Han, "Local Water Dynamics in Coacervated Polyelectrolytes Monitored through Dynamic Nuclear Polarization-Enhanced ^1H NMR," *Macromolecules*, vol. 42, no. 19, pp. 7404–7412, Oct. 2009, doi: 10.1021/ma901137g.
- [89] M. Nagura, J. Konishi, Y. Mon, and H. Ishikawa, "Fine-Structure of Coacervates Prepared from Aqueous-Solutions of Denatured Tropocollagen and of Chondroitin Sulfate-C," *Kobunshi Ronbunshu*, vol. 45, no. 7, pp. 581–586, 1988.
- [90] X. Du, D. Seeman, P. L. Dubin, and D. A. Hoagland, "Nonfreezing Water Structuration in Heteroprotein Coacervates," *Langmuir*, vol. 31, no. 31, pp. 8661–8666, Aug. 2015, doi: 10.1021/acs.langmuir.5b01647.
- [91] A. Tiwari, S. Bindal, and H. B. Bohidar, "Kinetics of Protein-Protein Complex Coacervation and Biphasic Release of Salbutamol Sulfate from Coacervate Matrix," *Biomacromolecules*, vol. 10, no. 1, pp. 184–189, Jan. 2009, doi: 10.1021/bm801160s.
- [92] K.-Y. Huang, H. Y. Yoo, Y. Jho, S. Han, and D. S. Hwang, "Bicontinuous Fluid Structure with Low Cohesive Energy: Molecular Basis for Exceptionally Low Interfacial Tension of Complex Coacervate Fluids," *ACS Nano*, vol. 10, no. 5, pp. 5051–5062, May 2016, doi: 10.1021/acsnano.5b07787.
- [93] S. Chodankar, V. K. Aswal, J. Kohlbrecher, R. Vavrin, and A. G. Wagh, "Structural study of coacervation in protein-polyelectrolyte complexes," *Phys. Rev. E*, vol. 78, no. 3, p. 031913, Sep. 2008, doi: 10.1103/PhysRevE.78.031913.

- [94] K. A. Burke, A. M. Janke, C. L. Rhine, and N. L. Fawzi, "Residue-by-Residue View of In Vitro FUS Granules that Bind the C-Terminal Domain of RNA Polymerase II," *Mol. Cell*, vol. 60, no. 2, pp. 231–241, Oct. 2015, doi: 10.1016/j.molcel.2015.09.006.
- [95] M. Goedert, R. Jakes, M. G. Spillantini, M. Hasegawa, M. J. Smith, and R. A. Crowther, "Assembly of microtubule-associated protein tau into Alzheimer-like filaments induced by sulphated glycosaminoglycans," *Nature*, vol. 383, no. 6600, pp. 550–553, Oct. 1996, doi: 10.1038/383550a0.
- [96] D. M. Wilson and L. I. Binder, "Free fatty acids stimulate the polymerization of tau and amyloid beta peptides. In vitro evidence for a common effector of pathogenesis in Alzheimer's disease.," *Am. J. Pathol.*, vol. 150, no. 6, pp. 2181–2195, Jun. 1997, Accessed: May 23, 2017. [Online]. Available: <http://www.ncbi.nlm.nih.gov/pmc/articles/PMC1858305/>.
- [97] P. D. Dinkel, M. R. Holden, N. Matin, and M. Margittai, "RNA Binds to Tau Fibrils and Sustains Template-Assisted Growth," *Biochemistry*, vol. 54, no. 30, pp. 4731–4740, Aug. 2015, doi: 10.1021/acs.biochem.5b00453.
- [98] G. Ramachandran and J. B. Udgaonkar, "Understanding the Kinetic Roles of the Inducer Heparin and of Rod-like Protofibrils during Amyloid Fibril Formation by Tau Protein," *J. Biol. Chem.*, vol. 286, no. 45, pp. 38948–38959, Nov. 2011, doi: 10.1074/jbc.M111.271874.
- [99] S. W. Carlson, M. Branden, K. Voss, Q. Sun, C. A. Rankin, and T. C. Gamblin, "A Complex Mechanism for Inducer Mediated Tau Polymerization†," *Biochemistry*, vol. 46, no. 30, pp. 8838–8849, Jul. 2007, doi: 10.1021/bi700403a.
- [100] N. Sibille *et al.*, "Structural Impact of Heparin Binding to Full-Length Tau As Studied by NMR Spectroscopy†," *Biochemistry*, vol. 45, no. 41, pp. 12560–12572, Oct. 2006, doi: 10.1021/bi060964o.
- [101] M. von Bergen *et al.*, "The Core of Tau-Paired Helical Filaments Studied by Scanning Transmission Electron Microscopy and Limited Proteolysis†," *Biochemistry*, vol. 45, no. 20, pp. 6446–6457, May 2006, doi: 10.1021/bi052530j.
- [102] A. L. Woerman *et al.*, "Tau prions from Alzheimer's disease and chronic traumatic encephalopathy patients propagate in cultured cells," *Proc. Natl. Acad. Sci.*, vol. 113, no. 50, pp. E8187–E8196, Dec. 2016, doi: 10.1073/pnas.1616344113.
- [103] A. Pavlova, C.-Y. Cheng, M. Kinnebrew, J. Lew, F. W. Dahlquist, and S. Han, "Protein structural and surface water rearrangement constitute major events in the earliest aggregation stages of tau," *Proc. Natl. Acad. Sci.*, vol. 113, no. 2, pp. E127–E136, Jan. 2016, doi: 10.1073/pnas.1504415113.
- [104] W. L. Hubbell and C. Altenbach, "Investigation of structure and dynamics in membrane proteins using site-directed spin labeling," *Curr. Opin. Struct. Biol.*, vol. 4, no. 4, pp. 566–573, Jan. 1994, doi: 10.1016/S0959-440X(94)90219-4.
- [105] S. S. Mirra *et al.*, "Tau pathology in a family with dementia and a P301L mutation in tau," *J. Neuropathol. Exp. Neurol.*, vol. 58, no. 4, pp. 335–345, Apr. 1999.

- [106] D. Xia, J. M. Gutmann, and J. Götz, “Mobility and subcellular localization of endogenous, gene-edited Tau differs from that of over-expressed human wild-type and P301L mutant Tau,” *Sci. Rep.*, vol. 6, p. 29074, Jul. 2016, doi: 10.1038/srep29074.
- [107] A. Sultan *et al.*, “Nuclear Tau, a Key Player in Neuronal DNA Protection,” *J. Biol. Chem.*, vol. 286, no. 6, pp. 4566–4575, Feb. 2011, doi: 10.1074/jbc.M110.199976.
- [108] K. Yamada, “Extracellular Tau and Its Potential Role in the Propagation of Tau Pathology,” *Front. Neurosci.*, vol. 11, Nov. 2017, doi: 10.3389/fnins.2017.00667.
- [109] Maïza Auriane *et al.*, “The role of heparan sulfates in protein aggregation and their potential impact on neurodegeneration,” *FEBS Lett.*, vol. 0, no. ja, May 2018, doi: 10.1002/1873-3468.13082.
- [110] J. N. Rauch *et al.*, “Tau Internalization is Regulated by 6-O Sulfation on Heparan Sulfate Proteoglycans (HSPGs),” *Sci. Rep.*, vol. 8, no. 1, p. 6382, Apr. 2018, doi: 10.1038/s41598-018-24904-z.
- [111] X. Zhang *et al.*, “RNA stores tau reversibly in complex coacervates,” *PLOS Biol.*, vol. 15, no. 7, p. e2002183, Jul. 2017, doi: 10.1371/journal.pbio.2002183.
- [112] S. D. Ginsberg, J. E. Galvin, T. S. Chiu, V. M. Lee, E. Masliah, and J. Q. Trojanowski, “RNA sequestration to pathological lesions of neurodegenerative diseases,” *Acta Neuropathol. (Berl.)*, vol. 96, no. 5, pp. 487–494, Nov. 1998.
- [113] A. W. P. Fitzpatrick *et al.*, “Cryo-EM structures of tau filaments from Alzheimer’s disease,” *Nature*, vol. 547, no. 7662, pp. 185–190, Jul. 2017, doi: 10.1038/nature23002.
- [114] B. Falcon *et al.*, “Structures of filaments from Pick’s disease reveal a novel tau protein fold,” *bioRxiv*, p. 302216, Apr. 2018, doi: 10.1101/302216.
- [115] J. P. Brady *et al.*, “Structural and hydrodynamic properties of an intrinsically disordered region of a germ cell-specific protein on phase separation,” *Proc. Natl. Acad. Sci.*, vol. 114, no. 39, pp. E8194–E8203, Sep. 2017, doi: 10.1073/pnas.1706197114.
- [116] F. Wippich, B. Bodenmiller, M. G. Trajkovska, S. Wanka, R. Aebersold, and L. Pelkmans, “Dual specificity kinase DYRK3 couples stress granule condensation/dissolution to mTORC1 signaling,” *Cell*, vol. 152, no. 4, pp. 791–805, Feb. 2013, doi: 10.1016/j.cell.2013.01.033.
- [117] A. Veis and C. Aranyi, “Phase separation in polyelectrolyte systems. I. Complex coacervates of gelatin,” *J. Phys. Chem.*, vol. 64, no. 9, pp. 1203–1210, 1960, Accessed: Oct. 17, 2016. [Online]. Available: <http://pubs.acs.org/doi/abs/10.1021/j100838a022>.
- [118] C. Arneodo, A. Baszkin, J. Benoit, and C. Thies, “Interfacial-Tension Behavior of Citrus Oils Against Phases Formed by Complex Coacervation of Gelatin,” *Acs Symp. Ser.*, vol. 370, pp. 132–147, 1988.
- [119] J. J. Water, M. M. Schack, A. Velazquez-Campoy, M. J. Maltesen, M. van de Weert, and L. Jorgensen, “Complex coacervates of hyaluronic acid and lysozyme: Effect on protein structure and physical stability,” *Eur. J. Pharm. Biopharm.*, vol. 88, no. 2, pp. 325–331, Oct. 2014, doi: 10.1016/j.ejpb.2014.09.001.
- [120] V. N. Uversky, I. M. Kuznetsova, K. K. Turoverov, and B. Zaslavsky, “Intrinsically disordered proteins as crucial constituents of cellular aqueous two phase systems and

- coacervates,” *FEBS Lett.*, vol. 589, no. 1, pp. 15–22, Jan. 2015, doi: 10.1016/j.febslet.2014.11.028.
- [121] S. Ambadipudi, J. Biernat, D. Riedel, E. Mandelkow, and M. Zweckstetter, “Liquid–liquid phase separation of the microtubule-binding repeats of the Alzheimer-related protein Tau,” *Nat. Commun.*, vol. 8, no. 1, p. 275, Aug. 2017, doi: 10.1038/s41467-017-00480-0.
- [122] A. Hernández-Vega *et al.*, “Local Nucleation of Microtubule Bundles through Tubulin Concentration into a Condensed Tau Phase,” *Cell Rep.*, vol. 20, no. 10, pp. 2304–2312, Sep. 2017, doi: 10.1016/j.celrep.2017.08.042.
- [123] J. C. Ferreón *et al.*, “Acetylation Disfavors Tau Phase Separation,” *Int. J. Mol. Sci.*, vol. 19, no. 5, May 2018, doi: 10.3390/ijms19051360.
- [124] S. Wegmann *et al.*, “Tau protein liquid-liquid phase separation can initiate tau aggregation,” *EMBO J.*, vol. 37, no. 7, Apr. 2018, doi: 10.15252/embj.201798049.
- [125] H. Bungenberg de Jong, “Crystallisation–coacervation–flocculation,” *Colloid Sci.*, vol. 2, pp. 232–258, 1949.
- [126] C. E. Sing, “Development of the modern theory of polymeric complex coacervation,” *Adv. Colloid Interface Sci.*, vol. 239, pp. 2–16, Jan. 2017, doi: 10.1016/j.cis.2016.04.004.
- [127] P. J. Flory, *Principles of Polymer Chemistry*. 1953.
- [128] E. Spruijt, A. H. Westphal, J. W. Borst, M. A. Cohen Stuart, and J. van der Gucht, “Binodal Compositions of Polyelectrolyte Complexes,” *Macromolecules*, vol. 43, no. 15, pp. 6476–6484, Aug. 2010, doi: 10.1021/ma101031t.
- [129] J. T. G. Overbeek and M. J. Voorn, “Phase separation in polyelectrolyte solutions. Theory of complex coacervation,” *J. Cell. Comp. Physiol.*, vol. 49, no. S1, pp. 7–26, May 1957, doi: 10.1002/jcp.1030490404.
- [130] K. Tainaka, “Study of Complex Coacervation in Low Concentration by Virial Expansion Method. I. Salt Free Systems,” *J. Phys. Soc. Jpn.*, vol. 46, no. 6, pp. 1899–1906, Jun. 1979, doi: 10.1143/JPSJ.46.1899.
- [131] A. Veis, “PHASE SEPARATION IN POLYELECTROLYTE SYSTEMS. III. EFFECT OF AGGREGATION AND MOLECULAR WEIGHT HETEROGENEITY,” *J. Phys. Chem.*, vol. 67, no. 10, pp. 1960–1964, Oct. 1963, doi: 10.1021/j100804a004.
- [132] K.-I. Tainaka, “Effect of counterions on complex coacervation,” *Biopolymers*, vol. 19, no. 7, pp. 1289–1298, Jul. 1980, doi: 10.1002/bip.1980.360190705.
- [133] A. Nakajima and H. Sato, “Phase relationships of an equivalent mixture of sulfated polyvinyl alcohol and aminoacetylated polyvinyl alcohol in microsalt aqueous solution,” *Biopolymers*, vol. 11, no. 7, pp. 1345–1355, doi: 10.1002/bip.1972.360110704.
- [134] V. Yu. Borue and I. Ya. Erukhimovich, “A statistical theory of weakly charged polyelectrolytes: fluctuations, equation of state and microphase separation,” *Macromolecules*, vol. 21, no. 11, pp. 3240–3249, Nov. 1988, doi: 10.1021/ma00189a019.

- [135] V. Yu. Borue and I. Ya. Erukhimovich, "A statistical theory of globular polyelectrolyte complexes," *Macromolecules*, vol. 23, no. 15, pp. 3625–3632, Jul. 1990, doi: 10.1021/ma00217a015.
- [136] M. Castelnovo and J.-F. Joanny, "Complexation between oppositely charged polyelectrolytes: Beyond the Random Phase Approximation," *Eur. Phys. J. E*, vol. 6, no. 1, pp. 377–386, Dec. 2001, doi: 10.1007/s10189-001-8051-7.
- [137] P. M. Biesheuvel and M. A. Cohen Stuart, "Electrostatic Free Energy of Weakly Charged Macromolecules in Solution and Intermacromolecular Complexes Consisting of Oppositely Charged Polymers," *Langmuir*, vol. 20, no. 7, pp. 2785–2791, Mar. 2004, doi: 10.1021/la036204l.
- [138] P. M. Biesheuvel and M. A. Cohen Stuart, "Cylindrical Cell Model for the Electrostatic Free Energy of Polyelectrolyte Complexes," *Langmuir*, vol. 20, no. 11, pp. 4764–4770, May 2004, doi: 10.1021/la0496789.
- [139] T. K. Lytle and C. E. Sing, "Transfer matrix theory of polymer complex coacervation," *Soft Matter*, vol. 13, no. 39, pp. 7001–7012, Oct. 2017, doi: 10.1039/C7SM01080J.
- [140] K. Shen and Z.-G. Wang, "Polyelectrolyte Chain Structure and Solution Phase Behavior," *Macromolecules*, vol. 51, no. 5, pp. 1706–1717, Mar. 2018, doi: 10.1021/acs.macromol.7b02685.
- [141] K. Shen and Z.-G. Wang, "Electrostatic correlations and the polyelectrolyte self energy," *J. Chem. Phys.*, vol. 146, no. 8, p. 084901, Feb. 2017, doi: 10.1063/1.4975777.
- [142] R. Chollakup, W. Smitthipong, C. D. Eisenbach, and M. Tirrell, "Phase Behavior and Coacervation of Aqueous Poly(acrylic acid)–Poly(allylamine) Solutions," *Macromolecules*, vol. 43, no. 5, pp. 2518–2528, Mar. 2010, doi: 10.1021/ma902144k.
- [143] A. S. Zalusky, R. Olayo-Valles, J. H. Wolf, and M. A. Hillmyer, "Ordered Nanoporous Polymers from Polystyrene–Polylactide Block Copolymers," *J. Am. Chem. Soc.*, vol. 124, no. 43, pp. 12761–12773, Oct. 2002, doi: 10.1021/ja0278584.
- [144] L. Li, S. Srivastava, M. Andreev, A. B. Marciel, J. J. de Pablo, and M. V. Tirrell, "Phase Behavior and Salt Partitioning in Polyelectrolyte Complex Coacervates," *Macromolecules*, vol. 51, no. 8, pp. 2988–2995, Apr. 2018, doi: 10.1021/acs.macromol.8b00238.
- [145] M. O. de la Cruz, L. Belloni, M. Delsanti, J. P. Dalbiez, O. Spalla, and M. Drifford, "Precipitation of highly charged polyelectrolyte solutions in the presence of multivalent salts," *J. Chem. Phys.*, vol. 103, no. 13, pp. 5781–5791, Oct. 1995, doi: 10.1063/1.470459.
- [146] S. Banjade and M. K. Rosen, "Phase transitions of multivalent proteins can promote clustering of membrane receptors," *eLife*, vol. 3, p. e04123, Oct. 2014, doi: 10.7554/eLife.04123.
- [147] S. Banjade, Q. Wu, A. Mittal, W. B. Peeples, R. V. Pappu, and M. K. Rosen, "Conserved interdomain linker promotes phase separation of the multivalent adaptor protein Nck," *Proc. Natl. Acad. Sci.*, vol. 112, no. 47, pp. E6426–E6435, Nov. 2015, doi: 10.1073/pnas.1508778112.

- [148] J. Qin and J. J. de Pablo, “Criticality and Connectivity in Macromolecular Charge Complexation,” *Macromolecules*, vol. 49, no. 22, pp. 8789–8800, Nov. 2016, doi: 10.1021/acs.macromol.6b02113.
- [149] A. Kudlay and M. Olvera de la Cruz, “Precipitation of oppositely charged polyelectrolytes in salt solutions,” *J. Chem. Phys.*, vol. 120, no. 1, pp. 404–412, Dec. 2003, doi: 10.1063/1.1629271.
- [150] A. Kudlay, A. V. Ermoshkin, and M. Olvera de la Cruz, “Complexation of Oppositely Charged Polyelectrolytes: Effect of Ion Pair Formation,” *Macromolecules*, vol. 37, no. 24, pp. 9231–9241, Nov. 2004, doi: 10.1021/ma048519t.
- [151] M. Castelnovo and J.-F. Joanny, “Formation of Polyelectrolyte Multilayers,” *Langmuir*, vol. 16, no. 19, pp. 7524–7532, Sep. 2000, doi: 10.1021/la000211h.
- [152] Y.-H. Lin, J. Song, J. D. Forman-Kay, and H. S. Chan, “Random-phase-approximation theory for sequence-dependent, biologically functional liquid-liquid phase separation of intrinsically disordered proteins,” *J. Mol. Liq.*, vol. 228, pp. 176–193, Feb. 2017, doi: 10.1016/j.molliq.2016.09.090.
- [153] Y.-H. Lin, J. D. Forman-Kay, and H. S. Chan, “Sequence-Specific Polyampholyte Phase Separation in Membraneless Organelles,” *Phys. Rev. Lett.*, vol. 117, no. 17, p. 178101, Oct. 2016, doi: 10.1103/PhysRevLett.117.178101.
- [154] K. T. Delaney and G. H. Fredrickson, “Theory of polyelectrolyte complexation—Complex coacervates are self-coacervates,” *J. Chem. Phys.*, vol. 146, no. 22, p. 224902, Jun. 2017, doi: 10.1063/1.4985568.
- [155] S. Das, A. Eisen, Y.-H. Lin, and H. S. Chan, “A Lattice Model of Charge-Pattern-Dependent Polyampholyte Phase Separation,” *J. Phys. Chem. B*, vol. 122, no. 21, pp. 5418–5431, May 2018, doi: 10.1021/acs.jpcb.7b11723.
- [156] D. W. Peterson, H. Zhou, F. W. Dahlquist, and J. Lew, “A soluble oligomer of tau associated with fiber formation analyzed by NMR,” *Biochemistry*, vol. 47, no. 28, pp. 7393–7404, Jul. 2008, doi: 10.1021/bi702466a.
- [157] N. Gustke, B. Trinczek, J. Biernat, E.-M. Mandelkow, and E. Mandelkow, “Domains of tau Protein and Interactions with Microtubules,” *Biochemistry*, vol. 33, no. 32, pp. 9511–9522, Oct. 1994, doi: 10.1021/bi00198a017.
- [158] K. S. Siow, G. Delmas, and D. Patterson, “Cloud-point curves in polymer solutions with adjacent upper and lower critical solution temperatures,” *Macromolecules*, vol. 5, no. 1, pp. 29–34, 1972, Accessed: Jun. 27, 2017. [Online]. Available: <http://pubs.acs.org/doi/pdf/10.1021/ma60025a008>.
- [159] J. Berry, S. C. Weber, N. Vaidya, M. Haataja, and C. P. Brangwynne, “RNA transcription modulates phase transition-driven nuclear body assembly,” *Proc. Natl. Acad. Sci.*, vol. 112, no. 38, pp. E5237–E5245, Sep. 2015, doi: 10.1073/pnas.1509317112.
- [160] Y.-H. Lin, J. D. Forman-Kay, and H. S. Chan, “Theories for Sequence-Dependent Phase Behaviors of Biomolecular Condensates,” *Biochemistry*, vol. 57, no. 17, pp. 2499–2508, May 2018, doi: 10.1021/acs.biochem.8b00058.

- [161] C. L. Dias and H. S. Chan, "Pressure-Dependent Properties of Elementary Hydrophobic Interactions: Ramifications for Activation Properties of Protein Folding," *J. Phys. Chem. B*, vol. 118, no. 27, pp. 7488–7509, Jul. 2014, doi: 10.1021/jp501935f.
- [162] K. A. Dill, D. O. V. Alonso, and K. Hutchinson, "Thermal stabilities of globular proteins," *Biochemistry*, vol. 28, no. 13, pp. 5439–5449, Jun. 1989, doi: 10.1021/bi00439a019.
- [163] C. Jeon, Y. Jung, and B.-Y. Ha, "Effects of molecular crowding and confinement on the spatial organization of a biopolymer," *Soft Matter*, vol. 12, no. 47, pp. 9436–9450, Nov. 2016, doi: 10.1039/C6SM01184E.
- [164] P.-G. de Gennes and P. P.-G. Gennes, *Scaling Concepts in Polymer Physics*. Cornell University Press, 1979.
- [165] K. A. T. Silverstein, A. D. J. Haymet, and K. A. Dill, "The Strength of Hydrogen Bonds in Liquid Water and Around Nonpolar Solutes," *J. Am. Chem. Soc.*, vol. 122, no. 33, pp. 8037–8041, Aug. 2000, doi: 10.1021/ja000459t.
- [166] G. I. Makhatadze and P. L. Privalov, "Contribution of Hydration to Protein Folding Thermodynamics: I. The Enthalpy of Hydration," *J. Mol. Biol.*, vol. 232, no. 2, pp. 639–659, Jul. 1993, doi: 10.1006/jmbi.1993.1416.
- [167] N. Matubayasi, "Free-energy analysis of protein solvation with all-atom molecular dynamics simulation combined with a theory of solutions," *Curr. Opin. Struct. Biol.*, vol. 43, pp. 45–54, Apr. 2017, doi: 10.1016/j.sbi.2016.10.005.
- [168] D. Thirumalai, G. Reddy, and J. E. Straub, "Role of Water in Protein Aggregation and Amyloid Polymorphism," *Acc. Chem. Res.*, vol. 45, no. 1, pp. 83–92, Jan. 2012, doi: 10.1021/ar2000869.
- [169] H. Feil, Y. H. Bae, J. Feijen, and S. W. Kim, "Effect of comonomer hydrophilicity and ionization on the lower critical solution temperature of N-isopropylacrylamide copolymers," *Macromolecules*, vol. 26, no. 10, pp. 2496–2500, May 1993, doi: 10.1021/ma00062a016.
- [170] E. Choi and A. Yethiraj, "Entropic Mechanism for the Lower Critical Solution Temperature of Poly(ethylene oxide) in a Room Temperature Ionic Liquid," *ACS Macro Lett.*, vol. 4, no. 7, pp. 799–803, Jul. 2015, doi: 10.1021/acsmacrolett.5b00355.
- [171] E. W. Martin and T. Mittag, "Relationship of Sequence and Phase Separation in Protein Low-Complexity Regions," *Biochemistry*, vol. 57, no. 17, pp. 2478–2487, 01 2018, doi: 10.1021/acs.biochem.8b00008.
- [172] A. V. Dobrynin and M. Rubinstein, "Counterion Condensation and Phase Separation in Solutions of Hydrophobic Polyelectrolytes," *Macromolecules*, vol. 34, no. 6, pp. 1964–1972, Mar. 2001, doi: 10.1021/ma001619o.
- [173] J. Gummel, F. Cousin, and F. Boué, "Counterions Release from Electrostatic Complexes of Polyelectrolytes and Proteins of Opposite Charge: A Direct Measurement," *J. Am. Chem. Soc.*, vol. 129, no. 18, pp. 5806–5807, May 2007, doi: 10.1021/ja070414t.

- [174] M. Muthukumar, “Theory of counter-ion condensation on flexible polyelectrolytes: Adsorption mechanism,” *J. Chem. Phys.*, vol. 120, no. 19, pp. 9343–9350, Apr. 2004, doi: 10.1063/1.1701839.
- [175] J. H. E. Hone, A. M. Howe, and T. Cosgrove, “A Small-Angle Neutron Scattering Study of the Structure of Gelatin/Polyelectrolyte Complexes,” *Macromolecules*, vol. 33, no. 4, pp. 1206–1212, Feb. 2000, doi: 10.1021/ma9911750.
- [176] R. H. Lacombe and I. C. Sanchez, “Statistical thermodynamics of fluid mixtures,” *J. Phys. Chem.*, vol. 80, no. 23, pp. 2568–2580, Nov. 1976, doi: 10.1021/j100564a009.
- [177] I. C. Sanchez and R. H. Lacombe, “Statistical Thermodynamics of Polymer Solutions,” *Macromolecules*, vol. 11, no. 6, pp. 1145–1156, Nov. 1978, doi: 10.1021/ma60066a017.
- [178] L.-W. Chang *et al.*, “Sequence and entropy-based control of complex coacervates,” *Nat. Commun.*, vol. 8, no. 1, p. 1273, Nov. 2017, doi: 10.1038/s41467-017-01249-1.
- [179] A. Pavlova, C.-Y. Cheng, M. Kinnebrew, J. Lew, F. W. Dahlquist, and S. Han, “Protein structural and surface water rearrangement constitute major events in the earliest aggregation stages of tau,” *Proc. Natl. Acad. Sci.*, vol. 113, no. 2, pp. E127–E136, 2016, Accessed: Mar. 23, 2016. [Online]. Available: <http://www.pnas.org/content/113/2/E127.short>.
- [180] A. Finka and P. Goloubinoff, “Proteomic data from human cell cultures refine mechanisms of chaperone-mediated protein homeostasis,” *Cell Stress Chaperones*, vol. 18, no. 5, pp. 591–605, Sep. 2013, doi: 10.1007/s12192-013-0413-3.
- [181] Y. Shin and C. P. Brangwynne, “Liquid phase condensation in cell physiology and disease,” *Science*, vol. 357, no. 6357, 22 2017, doi: 10.1126/science.aaf4382.
- [182] S. F. Banani *et al.*, “Compositional Control of Phase-Separated Cellular Bodies,” *Cell*, vol. 166, no. 3, pp. 651–663, Jul. 2016, doi: 10.1016/j.cell.2016.06.010.
- [183] J. A. Ditlev, L. B. Case, and M. K. Rosen, “Who’s In and Who’s Out—Compositional Control of Biomolecular Condensates,” *J. Mol. Biol.*, vol. 430, no. 23, pp. 4666–4684, Nov. 2018, doi: 10.1016/j.jmb.2018.08.003.
- [184] N. B. Nedelsky and J. P. Taylor, “Bridging biophysics and neurology: aberrant phase transitions in neurodegenerative disease,” *Nat. Rev. Neurol.*, vol. 15, no. 5, pp. 272–286, May 2019, doi: 10.1038/s41582-019-0157-5.
- [185] Y. Chen and T. J. Cohen, “Aggregation of the nucleic acid-binding protein TDP-43 occurs via distinct routes that are coordinated with stress granule formation,” *J. Biol. Chem.*, vol. 294, no. 10, pp. 3696–3706, 08 2019, doi: 10.1074/jbc.RA118.006351.
- [186] Y. Lin *et al.*, “Narrow equilibrium window for complex coacervation of tau and RNA under cellular conditions,” *eLife*, vol. 8, p. e42571, Apr. 2019, doi: 10.7554/eLife.42571.
- [187] A. Majumdar, P. Dogra, S. Maity, and S. Mukhopadhyay, “Liquid-Liquid Phase Separation is Driven by Large-Scale Conformational Unwinding and Fluctuations of Intrinsically Disordered Protein Molecules,” *bioRxiv*, Apr. 2019, doi: 10.1101/621714.

- [188] T. P. J. Knowles *et al.*, “An analytical solution to the kinetics of breakable filament assembly,” *Science*, vol. 326, no. 5959, pp. 1533–1537, Dec. 2009, doi: 10.1126/science.1178250.
- [189] G. Meisl *et al.*, “Differences in nucleation behavior underlie the contrasting aggregation kinetics of the A β 40 and A β 42 peptides,” *Proc. Natl. Acad. Sci. U. S. A.*, vol. 111, no. 26, pp. 9384–9389, Jul. 2014, doi: 10.1073/pnas.1401564111.
- [190] S. Barghorn and E. Mandelkow, “Toward a unified scheme for the aggregation of tau into Alzheimer paired helical filaments,” *Biochemistry*, vol. 41, no. 50, pp. 14885–14896, Dec. 2002.
- [191] S. L. Shammass *et al.*, “A mechanistic model of tau amyloid aggregation based on direct observation of oligomers,” *Nat. Commun.*, vol. 6, p. 7025, Apr. 2015, doi: 10.1038/ncomms8025.
- [192] M. Kjaergaard *et al.*, “Oligomer Diversity during the Aggregation of the Repeat Region of Tau,” *ACS Chem. Neurosci.*, vol. 9, no. 12, pp. 3060–3071, Dec. 2018, doi: 10.1021/acscchemneuro.8b00250.
- [193] F. Oosawa and S. Asakura, *Thermodynamics of the polymerization of protein*. London ; New York: Academic Press, 1975.
- [194] G. Meisl *et al.*, “Molecular mechanisms of protein aggregation from global fitting of kinetic models,” *Nat. Protoc.*, vol. 11, no. 2, p. 252, Feb. 2016, doi: 10.1038/nprot.2016.010.
- [195] K. Eden, R. Morris, J. Gillam, C. E. MacPhee, and R. J. Allen, “Competition between Primary Nucleation and Autocatalysis in Amyloid Fibril Self-Assembly,” *Biophys. J.*, vol. 108, no. 3, pp. 632–643, Feb. 2015, doi: 10.1016/j.bpj.2014.11.3465.
- [196] R. J. Morris, K. Eden, R. Yarwood, L. Jourdain, R. J. Allen, and C. E. Macphee, “Mechanistic and environmental control of the prevalence and lifetime of amyloid oligomers,” *Nat. Commun.*, vol. 4, p. 1891, 2013, doi: 10.1038/ncomms2909.
- [197] G. Jeschke, “Distance measurements in the nanometer range by pulse EPR,” *Chemphyschem Eur. J. Chem. Phys. Phys. Chem.*, vol. 3, no. 11, pp. 927–932, Nov. 2002, doi: 10.1002/1439-7641(20021115)3:11<927::AID-CPHC927>3.0.CO;2-Q.
- [198] G. Jeschke and Y. Polyhach, “Distance measurements on spin-labelled biomacromolecules by pulsed electron paramagnetic resonance,” *Phys. Chem. Chem. Phys. PCCP*, vol. 9, no. 16, pp. 1895–1910, Apr. 2007, doi: 10.1039/b614920k.
- [199] J. N. Rauch *et al.*, “Tau Internalization is Regulated by 6-O Sulfation on Heparan Sulfate Proteoglycans (HSPGs),” *Sci. Rep.*, vol. 8, no. 1, p. 6382, Apr. 2018, doi: 10.1038/s41598-018-24904-z.
- [200] J. Lewis *et al.*, “Neurofibrillary tangles, amyotrophy and progressive motor disturbance in mice expressing mutant (P301L) tau protein,” *Nat. Genet.*, vol. 25, no. 4, p. 402, Aug. 2000, doi: 10.1038/78078.
- [201] S. Kim *et al.*, “Salt Triggers the Simple Coacervation of an Underwater Adhesive When Cations Meet Aromatic π Electrons in Seawater,” *ACS Nano*, vol. 11, no. 7, pp. 6764–6772, Jul. 2017, doi: 10.1021/acsnano.7b01370.

- [202] S. Kim *et al.*, “Complexation and coacervation of like-charged polyelectrolytes inspired by mussels,” *Proc. Natl. Acad. Sci.*, vol. 113, no. 7, pp. E847–E853, Feb. 2016, doi: 10.1073/pnas.1521521113.
- [203] A. E. Conicella, G. H. Zerze, J. Mittal, and N. L. Fawzi, “ALS Mutations Disrupt Phase Separation Mediated by α -Helical Structure in the TDP-43 Low-Complexity C-Terminal Domain,” *Structure*, vol. 24, no. 9, pp. 1537–1549, Sep. 2016, doi: 10.1016/j.str.2016.07.007.
- [204] K. Ribbeck and D. Görlich, “The permeability barrier of nuclear pore complexes appears to operate via hydrophobic exclusion,” *EMBO J.*, vol. 21, no. 11, pp. 2664–2671, Jun. 2002, doi: 10.1093/emboj/21.11.2664.
- [205] S. Kroschwald *et al.*, “Promiscuous interactions and protein disaggregases determine the material state of stress-inducible RNP granules,” *eLife*, vol. 4, p. e06807, Aug. 2015, doi: 10.7554/eLife.06807.
- [206] T. R. Peskett, F. Rau, J. O’Driscoll, R. Patani, A. R. Lowe, and H. R. Saibil, “A Liquid to Solid Phase Transition Underlying Pathological Huntingtin Exon1 Aggregation,” *Mol. Cell*, vol. 70, no. 4, pp. 588–601.e6, May 2018, doi: 10.1016/j.molcel.2018.04.007.
- [207] P. Friedhoff, A. Schneider, E. M. Mandelkow, and E. Mandelkow, “Rapid assembly of Alzheimer-like paired helical filaments from microtubule-associated protein tau monitored by fluorescence in solution,” *Biochemistry*, vol. 37, no. 28, pp. 10223–10230, Jul. 1998, doi: 10.1021/bi980537d.
- [208] H.-L. Zhu *et al.*, “Quantitative Characterization of Heparin Binding to Tau Protein IMPLICATION FOR INDUCER-MEDIATED TAU FILAMENT FORMATION,” *J. Biol. Chem.*, vol. 285, no. 6, pp. 3592–3599, Feb. 2010, doi: 10.1074/jbc.M109.035691.
- [209] J. N. Israelachvili, *Intermolecular and Surface Forces*. Academic Press, 2011.
- [210] S. R. K. Ainavarapu *et al.*, “Contour Length and Refolding Rate of a Small Protein Controlled by Engineered Disulfide Bonds,” *Biophys. J.*, vol. 92, no. 1, pp. 225–233, Jan. 2007, doi: 10.1529/biophysj.106.091561.
- [211] T. P. Knowles *et al.*, “Role of Intermolecular Forces in Defining Material Properties of Protein Nanofibrils,” *Science*, vol. 318, no. 5858, pp. 1900–1903, Dec. 2007, doi: 10.1126/science.1150057.
- [212] M. R. Sawaya *et al.*, “Atomic structures of amyloid cross-beta spines reveal varied steric zippers,” *Nature*, vol. 447, no. 7143, pp. 453–457, May 2007, doi: 10.1038/nature05695.
- [213] O. S. Makin, E. Atkins, P. Sikorski, J. Johansson, and L. C. Serpell, “Molecular basis for amyloid fibril formation and stability,” *Proc. Natl. Acad. Sci.*, vol. 102, no. 2, pp. 315–320, Jan. 2005, doi: 10.1073/pnas.0406847102.
- [214] E. Gazit, “A possible role for π -stacking in the self-assembly of amyloid fibrils,” *FASEB J.*, vol. 16, no. 1, pp. 77–83, Jan. 2002, doi: 10.1096/fj.01-0442hyp.
- [215] A. B. Marciel, S. Srivastava, and M. V. Tirrell, “Structure and rheology of polyelectrolyte complex coacervates,” *Soft Matter*, vol. 14, no. 13, pp. 2454–2464, Mar. 2018, doi: 10.1039/C7SM02041D.

- [216] S. W. Carlson, M. Branden, K. Voss, Q. Sun, C. A. Rankin, and T. C. Gamblin, “A Complex Mechanism for Inducer Mediated Tau Polymerization[†],” *Biochemistry*, vol. 46, no. 30, pp. 8838–8849, Jul. 2007, doi: 10.1021/bi700403a.
- [217] Y. Fichou *et al.*, “Tau-Cofactor Complexes as Building Blocks of Tau Fibrils,” *Front. Neurosci.*, vol. 13, 2019, doi: 10.3389/fnins.2019.01339.
- [218] M. Goedert, R. Jakes, M. G. Spillantini, M. Hasegawa, M. J. Smith, and R. A. Crowther, “Assembly of microtubule-associated protein tau into Alzheimer-like filaments induced by sulphated glycosaminoglycans,” *Nature*, vol. 383, no. 6600, pp. 550–553, Oct. 1996, doi: 10.1038/383550a0.
- [219] Y. Fichou *et al.*, “Cofactors are essential constituents of stable and seeding-active tau fibrils,” *Proc. Natl. Acad. Sci.*, vol. 115, no. 52, pp. 13234–13239, Dec. 2018, doi: 10.1073/pnas.1810058115.
- [220] B. A. Gibson, L. K. Doolittle, L. E. Jensen, N. Gamarra, S. Redding, and M. K. Rosen, “Organization and Regulation of Chromatin by Liquid-Liquid Phase Separation,” *bioRxiv*, p. 523662, Jan. 2019, doi: 10.1101/523662.
- [221] J. Avila, J. J. Lucas, M. Perez, and F. Hernandez, “Role of tau protein in both physiological and pathological conditions,” *Physiol. Rev.*, vol. 84, no. 2, pp. 361–384, Apr. 2004, doi: 10.1152/physrev.00024.2003.
- [222] M. Ackmann, H. Wiech, and E. Mandelkow, “Nonsaturable Binding Indicates Clustering of Tau on the Microtubule Surface in a Paired Helical Filament-like Conformation,” *J. Biol. Chem.*, vol. 275, no. 39, pp. 30335–30343, Sep. 2000, doi: 10.1074/jbc.M002590200.
- [223] G. Hiller and K. Weber, “Radioimmunoassay for tubulin: a quantitative comparison of the tubulin content of different established tissue culture cells and tissues,” *Cell*, vol. 14, no. 4, pp. 795–804, Aug. 1978, doi: 10.1016/0092-8674(78)90335-5.
- [224] H. Ksiazek-Reding, L. I. Binder, and S. H. Yen, “Immunochemical and biochemical characterization of tau proteins in normal and Alzheimer’s disease brains with Alz 50 and Tau-1,” *J. Biol. Chem.*, vol. 263, no. 17, pp. 7948–7953, Jun. 1988, Accessed: May 31, 2019. [Online]. Available: <http://www.jbc.org/content/263/17/7948>.
- [225] T. Arendt, J. T. Stieler, and M. Holzer, “Tau and tauopathies,” *Brain Res. Bull.*, vol. 126, pp. 238–292, Sep. 2016, doi: 10.1016/j.brainresbull.2016.08.018.
- [226] S. Alberti and S. Carra, “Quality Control of Membraneless Organelles,” *J. Mol. Biol.*, vol. 430, no. 23, pp. 4711–4729, Nov. 2018, doi: 10.1016/j.jmb.2018.05.013.
- [227] J. A. Toretsky and P. E. Wright, “Assemblages: Functional units formed by cellular phase separation,” *J Cell Biol*, vol. 206, no. 5, pp. 579–588, Sep. 2014, doi: 10.1083/jcb.201404124.
- [228] S. Ray *et al.*, “Liquid-liquid phase separation and liquid-to-solid transition mediate α -synuclein amyloid fibril containing hydrogel formation,” *bioRxiv*, p. 619858, Apr. 2019, doi: 10.1101/619858.
- [229] A. Majumdar, P. Dogra, S. Maity, and S. Mukhopadhyay, “Liquid–Liquid Phase Separation Is Driven by Large-Scale Conformational Unwinding and Fluctuations of

- Intrinsically Disordered Protein Molecules,” *J. Phys. Chem. Lett.*, vol. 10, no. 14, pp. 3929–3936, Jul. 2019, doi: 10.1021/acs.jpclett.9b01731.
- [230] S. F. Banani, H. O. Lee, A. A. Hyman, and M. K. Rosen, “Biomolecular condensates: organizers of cellular biochemistry,” *Nat. Rev. Mol. Cell Biol.*, vol. 18, no. 5, pp. 285–298, May 2017, doi: 10.1038/nrm.2017.7.
- [231] H. J. Dyson, P. E. Wright, and H. A. Scheraga, “The role of hydrophobic interactions in initiation and propagation of protein folding,” *Proc. Natl. Acad. Sci.*, vol. 103, no. 35, pp. 13057–13061, Aug. 2006, doi: 10.1073/pnas.0605504103.
- [232] B. Gabryelczyk *et al.*, “Hydrogen bond guidance and aromatic stacking drive liquid-liquid phase separation of intrinsically disordered histidine-rich peptides,” *Nat. Commun.*, vol. 10, no. 1, pp. 1–12, Nov. 2019, doi: 10.1038/s41467-019-13469-8.
- [233] S. Park *et al.*, “Dehydration entropy drives liquid-liquid phase separation by molecular crowding,” *Commun. Chem.*, vol. 3, no. 1, pp. 1–12, Jun. 2020, doi: 10.1038/s42004-020-0328-8.
- [234] W. Kunz, J. Henle, and B. W. Ninham, “‘Zur Lehre von der Wirkung der Salze’ (About the science of the effect of salts): Franz Hofmeister’s historical papers,” *Curr. Opin. Colloid Interface Sci.*, vol. 9, no. 1–2, pp. 19–37, 2004, Accessed: Jul. 03, 2020. [Online]. Available: <https://epub.uni-regensburg.de/24565/>.
- [235] Y. Zhang and P. S. Cremer, “Interactions between macromolecules and ions: the Hofmeister series,” *Curr. Opin. Chem. Biol.*, vol. 10, no. 6, pp. 658–663, Dec. 2006, doi: 10.1016/j.cbpa.2006.09.020.
- [236] R. A. Curtis, C. Steinbrecher, M. Heinemann, H. W. Blanch, and J. M. Prausnitz, “Hydrophobic forces between protein molecules in aqueous solutions of concentrated electrolyte,” *Biophys. Chem.*, vol. 98, no. 3, pp. 249–265, Aug. 2002, doi: 10.1016/S0301-4622(02)00071-6.
- [237] T. Ghosh, A. Kalra, and S. Garde, “On the Salt-Induced Stabilization of Pair and Many-body Hydrophobic Interactions,” *J. Phys. Chem. B*, vol. 109, no. 1, pp. 642–651, Jan. 2005, doi: 10.1021/jp0475638.
- [238] M. K. Braun *et al.*, “Reentrant Phase Behavior in Protein Solutions Induced by Multivalent Salts: Strong Effect of Anions Cl[−] Versus NO₃[−],” *J. Phys. Chem. B*, vol. 122, no. 50, pp. 11978–11985, Dec. 2018, doi: 10.1021/acs.jpcb.8b10268.
- [239] Y. Zhang and P. S. Cremer, “The inverse and direct Hofmeister series for lysozyme,” *Proc. Natl. Acad. Sci.*, vol. 106, no. 36, pp. 15249–15253, Sep. 2009, doi: 10.1073/pnas.0907616106.
- [240] G. Krainer *et al.*, “Reentrant liquid condensate phase of proteins is stabilized by hydrophobic and non-ionic interactions,” *bioRxiv*, p. 2020.05.04.076299, May 2020, doi: 10.1101/2020.05.04.076299.
- [241] S. H. Scheres, W. Zhang, B. Falcon, and M. Goedert, “Cryo-EM structures of tau filaments,” *Curr. Opin. Struct. Biol.*, vol. 64, pp. 17–25, Oct. 2020, doi: 10.1016/j.sbi.2020.05.011.

- [242] S. Kroschwald, S. Maharana, and A. Simon, “Hexanediol: a chemical probe to investigate the material properties of membrane-less compartments,” *Matters*, vol. 3, no. 5, p. e201702000010, May 2017, doi: 10.19185/matters.201702000010.
- [243] S. S. Patel, B. J. Belmont, J. M. Sante, and M. F. Rexach, “Natively Unfolded Nucleoporins Gate Protein Diffusion across the Nuclear Pore Complex,” *Cell*, vol. 129, no. 1, pp. 83–96, Apr. 2007, doi: 10.1016/j.cell.2007.01.044.
- [244] A. D. Gitler, J. Shorter, T. Ha, and S. Myong, “Just Took a DNA Test, Turns Out 100% Not That Phase,” *Mol. Cell*, vol. 78, no. 2, pp. 193–194, Apr. 2020, doi: 10.1016/j.molcel.2020.03.029.
- [245] S. Ambadipudi, J. G. Reddy, J. Biernat, E. Mandelkow, and M. Zweckstetter, “Residue-specific identification of phase separation hot spots of Alzheimer’s-related protein tau,” *Chem. Sci.*, vol. 10, no. 26, pp. 6503–6507, Jul. 2019, doi: 10.1039/C9SC00531E.
- [246] J. S. D’Arrigo, “Screening of membrane surface charges by divalent cations: an atomic representation,” *Am. J. Physiol.*, vol. 235, no. 3, pp. C109–117, Sep. 1978, doi: 10.1152/ajpcell.1978.235.3.C109.
- [247] Y. Lin, D. S. W. Protter, M. K. Rosen, and R. Parker, “Formation and Maturation of Phase-Separated Liquid Droplets by RNA-Binding Proteins,” *Mol. Cell*, vol. 60, no. 2, pp. 208–219, Oct. 2015, doi: 10.1016/j.molcel.2015.08.018.
- [248] M. Kubánková *et al.*, “Probing supramolecular protein assembly using covalently attached fluorescent molecular rotors,” *Biomaterials*, vol. 139, pp. 195–201, Sep. 2017, doi: 10.1016/j.biomaterials.2017.06.009.
- [249] J. E. Chambers *et al.*, “An Optical Technique for Mapping Microviscosity Dynamics in Cellular Organelles,” *ACS Nano*, vol. 12, no. 5, pp. 4398–4407, May 2018, doi: 10.1021/acsnano.8b00177.
- [250] S.-C. Lee *et al.*, “Fluorescent Molecular Rotors for Viscosity Sensors,” *Chem. – Eur. J.*, vol. 24, no. 52, pp. 13706–13718, Sep. 2018, doi: 10.1002/chem.201801389.
- [251] M. K. Kuimova, G. Yahiolu, J. A. Levitt, and K. Suhling, “Molecular Rotor Measures Viscosity of Live Cells via Fluorescence Lifetime Imaging,” *J. Am. Chem. Soc.*, vol. 130, no. 21, pp. 6672–6673, May 2008, doi: 10.1021/ja800570d.
- [252] S. C. Warren *et al.*, “Rapid Global Fitting of Large Fluorescence Lifetime Imaging Microscopy Datasets,” *PLOS ONE*, vol. 8, no. 8, p. e70687, Aug. 2013, doi: 10.1371/journal.pone.0070687.
- [253] D. R. Robinson and W. P. Jencks, “The Effect of Concentrated Salt Solutions on the Activity Coefficient of Acetyltetraglycine Ethyl Ester,” *J. Am. Chem. Soc.*, vol. 87, no. 11, pp. 2470–2479, Jun. 1965, doi: 10.1021/ja01089a029.
- [254] A. Volkov, C. Dockter, T. Bund, H. Paulsen, and G. Jeschke, “Pulsed EPR determination of water accessibility to spin-labeled amino acid residues in LHCIIB,” *Biophys. J.*, vol. 96, no. 3, pp. 1124–1141, Feb. 2009, doi: 10.1016/j.bpj.2008.09.047.
- [255] J. M. Franck *et al.*, “Probing Water Density and Dynamics in the Chaperonin GroEL Cavity,” *J. Am. Chem. Soc.*, vol. 136, no. 26, pp. 9396–9403, Jul. 2014, doi: 10.1021/ja503501x.

- [256] A. Doll, E. Bordignon, B. Joseph, R. Tschaggelar, and G. Jeschke, “Liquid state DNP for water accessibility measurements on spin-labeled membrane proteins at physiological temperatures,” *J. Magn. Reson. San Diego Calif 1997*, vol. 222, pp. 34–43, Sep. 2012, doi: 10.1016/j.jmr.2012.06.003.
- [257] B. D. Armstrong and S. Han, “Overhauser Dynamic Nuclear Polarization To Study Local Water Dynamics,” *J. Am. Chem. Soc.*, vol. 131, no. 13, pp. 4641–4647, Apr. 2009, doi: 10.1021/ja809259q.
- [258] J. M. Franck, Y. Ding, K. Stone, P. Z. Qin, and S. Han, “Anomalously Rapid Hydration Water Diffusion Dynamics Near DNA Surfaces,” *J. Am. Chem. Soc.*, vol. 137, no. 37, pp. 12013–12023, Sep. 2015, doi: 10.1021/jacs.5b05813.
- [259] T. F. Segawa, M. Doppelbauer, L. Garbuio, A. Doll, Y. O. Polyhach, and G. Jeschke, “Water accessibility in a membrane-inserting peptide comparing Overhauser DNP and pulse EPR methods,” *J. Chem. Phys.*, vol. 144, no. 19, p. 194201, May 2016, doi: 10.1063/1.4948988.
- [260] D. E. Budil, S. Lee, S. Saxena, and J. H. Freed, “Nonlinear-Least-Squares Analysis of Slow-Motion EPR Spectra in One and Two Dimensions Using a Modified Levenberg–Marquardt Algorithm,” *J. Magn. Reson. A*, vol. 120, no. 2, pp. 155–189, Jun. 1996, doi: 10.1006/jmra.1996.0113.
- [261] J. S. Hwang, R. P. Mason, L. P. Hwang, and J. H. Freed, “Electron spin resonance studies of anisotropic rotational reorientation and slow tumbling in liquid and frozen media. III. Perdeuterated 2,2,6,6-tetramethyl-4-piperidone N-oxide and an analysis of fluctuating torques,” *J. Phys. Chem.*, vol. 79, no. 5, pp. 489–511, Feb. 1975, doi: 10.1021/j100572a017.
- [262] D. Chen *et al.*, “Tau local structure shields an amyloid-forming motif and controls aggregation propensity,” *Nat. Commun.*, vol. 10, no. 1, pp. 1–14, Jun. 2019, doi: 10.1038/s41467-019-10355-1.
- [263] G. C. Ruben, T. L. Ciardelli, I. Grundke-Iqbal, and K. Iqbal, “Alzheimer disease hyperphosphorylated tau aggregates hydrophobically,” *Synapse*, vol. 27, no. 3, pp. 208–229, 1997, doi: 10.1002/(SICI)1098-2396(199711)27:3<208::AID-SYN7>3.0.CO;2-H.
- [264] A. Pavlova, E. R. McCarney, D. W. Peterson, F. W. Dahlquist, J. Lew, and S. Han, “Site-specific dynamic nuclear polarization of hydration water as a generally applicable approach to monitor protein aggregation,” *Phys. Chem. Chem. Phys. PCCP*, vol. 11, no. 31, pp. 6833–6839, Aug. 2009, doi: 10.1039/b906101k.
- [265] E. Hückel and P. Debye, “The theory of electrolytes: I. lowering of freezing point and related phenomena,” *Phys Z*, vol. 24, pp. 185–206, 1923.
- [266] J. Fu and J. B. Schlenoff, “Driving Forces for Oppositely Charged Polyion Association in Aqueous Solutions: Enthalpic, Entropic, but Not Electrostatic,” *J. Am. Chem. Soc.*, vol. 138, no. 3, pp. 980–990, Jan. 2016, doi: 10.1021/jacs.5b11878.
- [267] A. S. Holehouse, K. Garai, N. Lyle, A. Vitalis, and R. V. Pappu, “Quantitative Assessments of the Distinct Contributions of Polypeptide Backbone Amides versus Side Chain Groups to Chain Expansion via Chemical Denaturation,” *J. Am. Chem. Soc.*, vol. 137, no. 8, pp. 2984–2995, Mar. 2015, doi: 10.1021/ja512062h.

- [268] H.-K. Kwon, J. W. Zwanikken, K. R. Shull, and M. Olvera de la Cruz, “Theoretical Analysis of Multiple Phase Coexistence in Polyelectrolyte Blends,” *Macromolecules*, vol. 48, no. 16, pp. 6008–6015, Aug. 2015, doi: 10.1021/acs.macromol.5b00901.
- [269] M. Rubinstein and R. H. Colby, *Polymer Physics*. OUP Oxford, 2003.

Materials and Methods

Protein expression and purification

Unless stated, a 20 mM ammonium acetate buffer at pH 7.0 was used and referred to here as final buffer. Tau, RNA, NaCl, PEG and other stocks were prepared using final buffer. Measurements were taken in final buffer at room temperature unless stated.

N-terminal truncated, microtubule binding domain containing tau187 (residues 255-441 with a His-tag at the N-terminus) were used for *in vitro* studies. The cloning, expression, and purification have been previously described [156], [264]. The single cysteine variant of tau187 (tau187C291S) were generated via site-direct mutagenesis. *E. coli* BL21 (DE3) cells previously transfected were cultured from frozen glycerol stock overnight in 10 mL luria broth (LB) which was used to inoculate 1 L of fresh LB. Culturing and inoculation were performed at 37 °C with shaking of 200 rpm. At OD₆₀₀ of 0.6–0.8, tau187 variant expression was induced by incubation with 1 mM isopropylβ-D-thiogalactoside (Sigma Aldrich) for 2–3 h. Cells were harvested by centrifugation for 30 min at 5000 × g (Beckman J-10; Beckman Instruments, Inc.), and the pellets were stored at –20 °C until further use.

Cell pellets were resuspended in lysis buffer (Tris-HCl pH 7.4, 100 mM NaCl, 0.5 mM DTT, 0.1 mM EDTA, 1mM PMSF) with 1 Pierce protease inhibitor tablet (Thermo Fisher). Lysis was initiated by the addition of lysozyme (2 mg/ml), DNase (20 µg/ml), and MgCl₂ (10 mM) and incubated for 30 min on ice. Lysate was then heated to 65 °C for 13 min, cooled on ice for 20 min and then centrifuged to remove the precipitant. The supernatant was loaded onto

a Ni-NTA agarose column pre-equilibrated with wash buffer A (20 mM sodium phosphate pH 7.0, 500 mM NaCl, 10 mM imidazole, 100 μ M EDTA). The column was then washed with 20 ml of buffer A, 15 ml buffer B (20 mM sodium phosphate pH 7.0, 1 M NaCl, 20 mM imidazole, 0.5 mM DTT, 100 μ M EDTA). Purified tau187 was eluted with buffer C (20 mM sodium phosphate pH 7.0, 0.5 mM DTT, 100 mM NaCl) supplemented with varying amounts of imidazole increasing from 100 mM to 300 mM. The protein was then concentrated via centrifugal filters (MWCO 10 kDa; Millipore Sigma) and the buffer was exchanged into final buffer by PD-10 desalting column (GE Healthcare). The final protein concentration was determined by UV-Vis absorption at 274 nm using an extinction coefficient of 2.8 $\text{cm}^{-1}\text{mM}^{-1}$, calculated from absorption of Tyrosine [3].

Preparation of tau-polyanion droplets and microscope imaging.

We used the following polyanions in this work for studying LLPS and amyloid aggregation: Poly(A) RNA (MW 66 ~ 660 kDa, Sigma, P9403); Poly(U) RNA (MW 800~1000 kDa, Sigma, P9528); Poly(dA) single strand DNA (MW 83~165 kDa, Sigma, 10223581001); Hyaluronic acid (MW 8~15 kDa, Sigma, 40583). Besides, heparin, 6-O-desulfated heparin, 2-O-desulfated heparin and N-desulfated reN-acetylated heparin are all polydisperse, with average MW ~15 kDa and from Galen laboratory supplies under the reference number, HEP001, DSH002/6, DSH001/2 and DSH004/NAc, respectively. The primary chemical structure and charge properties were listed in (Table 2 of Chapter 3).

We followed the previously reported method for preparing tau-polyanion droplets for microscope imaging [22], [186]. The charge per mass at neutral pH of all tau variants was

estimated using Innovagen's Peptide Property Calculator (<http://pepcalc.com/>). The charge per mass for polyanions were estimated assuming all charged groups are fully ionized and negatively charged. For microscope imaging, polyanions were mixed with tau in certain mass ratio, as stated. Images were taken within 10 minutes after mixing. Bright-field images were acquired using an inverted compound microscope (Olympus IX70). Confocal images were acquired using a spectral confocal microscope (Olympus Fluoview 1000). Images of ThT fluorescence were taken using $\lambda_{\text{emission}}=485$ nm.

Spin labeling and cw EPR

Freshly eluted tau187C291S (with one cysteine at site 322) was replaced in final buffer using a PD-10 desalting column (GE Healthcare). Protein after PD-10 was labeled overnight at 4°C by immediately mixing with a 10-fold molar excess of the spin label (1-oxy1-2,2,5,5-tetramethylpyrroline-3-methyl) methanethiosulfonate (MTSL; Toronto Research Chemicals), resulting in spin labelled tau (tau187C291S-SL). Excess label was removed using PD-10. The protein was concentrated using centrifugal filter (MWCO 10 kDa; Amicon) and the final protein concentration was determined by UV-Vis absorption at 274 nm as mentioned above. Non-labeled tau187C291S was used in order to achieve spin dilution.

Cw EPR measurements were carried out using a X-band spectrometer operating at 9.8 GHz (EMX; Bruker Biospin, Billerica, MA) and a dielectric cavity (ER 4123D; Bruker Biospin, Billerica, MA). 100 μ M tau187C291S-SL was mixed with 400 μ M tau187C291S to reach 20% spin labeling. Samples under droplet forming condition were prepared by adding 1.5 mg/ml RNA, and tau samples under aggregation-inducing conditions prepared by adding 125 μ M

heparin (15 kDa average MW; Sigma-Aldrich). A sample of 4.0 μ l volume was loaded into a quartz capillary (CV6084; VitroCom) and sealed at both ends with critoseal, and then placed in the dielectric cavity for measurements. Cw EPR spectra were acquired by using 6 mW of microwave power, 0.5 gauss modulation amplitude, 100 gauss sweep width, and 8-64 scans for signal averaging.

Cw EPR spectra analysis

The recorded cw EPR spectra were subjected to single- or double-component simulation. EPR simulation and fitting were performed using MultiComponent, a program developed by Christian Altenbach (University of California, Los Angeles). For all spectra fitting, the magnetic tensors A and g were fixed and used as constraints as previously reported [179]. These values are $A_{xx} = 6.2$ G, $A_{yy} = 5.9$ G, $A_{zz} = 37.0$ G, and $g_{xx} = 2.0078$, $g_{yy} = 2.0058$, and $g_{zz} = 2.0022$.

For soluble tau, the cw EPR spectra were best fitted with a single-component simulation and the rotational diffusion constant (R) can be extracted. The rotation correlation time τ_R was calculated using $\tau_R = 1/(6R)$. For tau-heparin aggregates, the cw EPR were subjected to double-component simulation, where the parameters of the fitted single-component were used as a mobile-component. The immobile-component were set to be identical to the mobile-component, except the diffusion tensor tilt angle $\beta_D = 36^\circ$ and the order parameter S . The fitting parameters were limited at a minimum, which includes the population, p , rotational diffusion constants of mobile- and immobile-component, R_1 and R_2 , and the order parameter, S of the immobile-component. The fitted immobile-component were used to represent the rotational

correlation time for tau-heparin fibrils. For tau-RNA CC, the cw EPR spectra were subjected to both single- and double-component fitting. Comparing the two fitting schemes showed that single-component fitting has almost overlapped the cw EPR spectra, while double-component fitting results in a immobile-component population of ~10% (data not shown). This showed that tau-RNA CC cw EPR spectra can be sufficiently fit with single-component. The fitted rotational correlation time was calculated and plotted against tau-heparin samples.

Double Electron Electron Resonance (DEER).

Tau187V300CV313C was expressed as other tau187 mutants and spin labeled as follow. Tau was freshly purified and treated with 5 mM TCEP. TCEP was removed using a PD-10 desalting column. Immediately after PD-10, 10× to 15× molar excess of MTSL ((1-Acetoxy-2,2,5,5-tetramethyl- δ -3-pyrroline-3-methyl) Methanethiosulfonate, Toronto Research Chemicals, O875000) to free cysteine was incubated with the protein at 4 °C overnight. After incubation, excess MTSL was removed using a PD-10 desalting column. Labelling efficiency, defined as the molar ratio of tethered spin labels over the cysteines, was measured to be 50-60%. Spin-labeled tau187V300CV313C is referred to as tau-SL₂. Both tau-SL₂ and tauSS (cysteine-less tau187) were concentrated, and buffer exchanged against D₂O-based buffer (20 mM HEPES in D₂O) using Amicon centrifugal concentrators (10 kDa cutoff). A 1:22 molar ratio of tau-SL₂:tauSS sample of 10 μ M tau-SL₂ and 2.1 mM tauSS was mixed with polyanions at designated concentrations and incubated for designated time. 28 μ L samples were mixed with 12 μ L D₈-glycerol (Sigma-Aldrich) before transferring to a quartz tube (2 mm i.d.) and frozen using liquid nitrogen.

Four-pulse DEER experiments were carried out at 85 K using the Q-band Bruker E580 Eleksys pulse EPR spectrometer operating at ~34 GHz and equipped with a 300 W TWT amplifier. The following DEER pulse sequence was used: $\pi_{\text{obs}}/2 - \tau_1 - \pi_{\text{obs}} - (t - \pi_{\text{pump}}) - (\tau_2 - t) - \pi_{\text{obs}} - \tau_2 - \text{echo}$. Rectangular observe pulses were used with lengths set to $\pi_{\text{obs}}/2 = 10\text{-}12$ ns and $\pi_{\text{obs}} = 20\text{-}24$ ns. A chirp π_{pump} pulse was applied with a length of 20-24 ns and a frequency width of 60 MHz. The observe frequency was 90 MHz higher than the center of the pump frequency range. τ_1 was 180 ns and τ_2 was set to 2.4 ms. The DEER experiment was accumulated for ~12 h. The background-subtracted data were fitted assuming a Gaussian distribution of the inter-spin distances. The analysis was done using the LongDistance software (<http://www.chemistry.ucla.edu/directory/hubbell-wayne-l>).

Overhauser Dynamic Nuclear Polarization

Overhauser dynamic nuclear polarization (ODNP) of peptide samples were carried out at 0.35 T corresponding to a proton Larmor frequency of 14.8 MHz and an electron Larmor frequency of 9.8 GHz. A 3.5 μL sample was loaded into a 0.6 mm i.d., 0.84 mm o.d. quartz capillary tube (VitroCom) which is then sealed at one end with critoseal and the other end with beeswax. This capillary is then attached to a home-built NMR probe which sits inside the dielectric EPR cavity. The probe was connected to a Bruker Avance spectrometer for the detection of ^1H NMR. The sample was cooled by blowing room-temperature air over it to avoid heating caused by the application of microwaves. ODNP was then performed by continuously pumping 9.8 GHz microwave irradiation to the sample in order to saturate the EPR transitions while simultaneously

recording proton NMR signal at 14.8 MHz. Proton spin-lattice relaxation times (T_1) were acquired using an inversion-recovery pulse sequence.

Turbidimetry and brightfield microscopy

Turbidity of samples at room temperature were represented by optical density at a 500-nm wavelength (OD_{500}), using a Shimadzu UV-1601 spectrophotometer (Shimadzu Inc.). The amount of coacervates in a sample were approximated to be proportional to its OD_{500} .

Turbidity of samples at ramping temperatures were represented by OD_{500} measured using Jasco J-1500 CD Spectrometer (JASCO Inc.) equipped with temperature controller and spectrophotometer. 120 μ L of 20 μ M tau187C291S, 60 μ g/mL polyU RNA and 30 mM NaCl in working buffer were prepared in a 100 μ L cuvette (Starna Scientific Ltd) and kept at 4 $^{\circ}$ C for 5 min before cycling. Heating and cooling temperatures were ramped at 1 $^{\circ}$ C/min while OD_{500} was monitored.

Bright field images were examined to confirm the presence of tau-RNA CC. 100 μ M tau187C291S and 300 μ g/mL polyU RNA was mixed in presence of 20 mM ammonium acetate and 30 mM NaCl. 10 μ L of the mixture was pipetted onto a microscope slide with a cover slide gapped by two layers of double-sided sticky tape. Temperatures were controlled using an incubator. Bright field images were acquired using a spectral confocal microscope (Olympus Fluoview 1000; Olympus, Center Valley, PA).

ThT assays

Tau, polyanions and NaCl were mixed and pipetted onto a micro plate (Corning, 3844). Absorbance at 500 nm and fluorescence intensity (excitation 440 nm, emission 485 nm) were both monitored using a Bio-Tek Synergy 2 microplate reader, with temperature maintained at 26.0 °C.

To minimize the inference of ThT fluorescence and tau fibril scattering, averaged absorbance of the initial 1 hour where ThT fluorescence is below 10% was used as turbidity reading.

Along with each run of microplate reader, an equal volume of buffer with same concentration of ThT was added to the plate and used as control. Turbidity reading of the control were subtracted from the turbidity reading of each sample. ThT fluorescence reading from each sample were corrected by the control reading, in order to reduce the artifact from lamp drift/fluctuation, following the two equations below.

$$ThT_{fluc} = \frac{ThT_{control} - \overline{ThT_{control}}}{\overline{ThT_{control}}}, \quad ThT_{sample}^* = \frac{ThT_{sample}}{1 + ThT_{fluc}}$$

where $ThT_{control}$ is the fluorescence reading of the control samples; $\overline{ThT_{control}}$ is the averaged value throughout the entire course of measurement; ThT_{fluc} is the drift/fluctuation of the lamp; ThT_{sample} and ThT_{sample}^* are fluorescence reading of the sample before and after correction, respectively.

We applied the following steps to extract the half time and maximum ThT fluorescence. First, for each well of the microplate, the first 10 minutes of the above lamp-corrected readings

were averaged and used as a baseline, assuming no amyloid aggregates formed during this time. Next the baselines of each well were subtracted from the ThT readings. Third, the maximal ThT readings of the entire microplate during the entire incubation was used to divide all the readings, scaling to 0-1. Fourth, the following sigmoid function was used to fit all the readings, using Levenberg-Marquardt algorithm, provided by nls.lm function in minpack.lm package, with initial guess ($A = 1, t_{1/2} = 5, k = 1$)

$$y = \frac{A}{1 + \exp(-k(t - t_{1/2}))}$$

where the fitted A and $t_{1/2}$ were used as maximum ThT fluorescence and half time, respectively. The fitted results were visually examined to ensure a good fit.

Determining tau-RNA CC composition

It was shown by fluorescence microscopy in protein-RNA LLPS that protein is concentrated inside the droplet [15], [67, p. 1]. For representing tau inside the droplets with measurement taken from droplet suspension, we quantified the percentage of tau present as droplets. After mixing and centrifuging 60 μ L droplet suspension of 400 μ M tau187/322C and 1500 μ g/mL polyU, \sim 1 μ L dense phase was generated with clear boundary against dilute phase. Dissolving dense phase in high concentration of NaCl resulted in transparent solution thus UV absorption can be measured.

Due to the difficulty of preparing large volume of pure dense phase, we can only underestimate the tau and polyU concentration in dense phase. Since tau and RNA have different UV absorbance spectra, fitting spectra of the tau-RNA mixed sample with those of

pure tau and polyU generated the concentration of both. Fitting results showed that over 99% of the tau and over 99.9% of polyU were condensed inside the dense phase. This partitioning guaranteed that the property of tau in the droplet suspension represents those in the droplets.

Flory-Huggins based Voorn-Overbeek (FH-VO) modeling

FH-VO is based on a Flory-Huggins (FH) treatment, where the polymer system is mapped onto a lattice. Voorn and Overbeek extended the FH formalism to polyelectrolytes by including long-ranged electrostatic interactions with a Debye–Hückel term. The resulting expression for the free energy of mixing (ΔG_{mix}) per lattice site is

$$\frac{\Delta G_m}{Mk_B T} = \sum \frac{\phi_i}{N_i} \ln \phi_i - \alpha [\sum \sigma_i \phi_i]^{\frac{3}{2}} + \sum \chi_{ij} \phi_i \phi_j \quad (\text{S1})$$

Where $M = V/(l_w)^3$ is the total number of lattice sites. In Equation S1, the index i refers to one of the five species. N_i is the degree of polymerization for species i . For tau187 and tau114, N_i equals to the length of the polypeptides; while for RNA, N_i is estimated by the average MW 900 kDa for polyU RNA and the MW of condensed uridine monophosphate, 306 Da. For monovalent ions and water, $N_i = 1$.

σ_i is the average charge per monomer, which is determined by (net charge) / N_i . The net charges of tau at experimental pH conditions (pH = 7) were estimated based on primary sequences, using pepcalc.com. σ_i for other species were listed in Figure 4-2-source data 1. In FH-VO model, σ_i is fixed. We also consider a modified version, a FH-VO-CR model, where σ_i of RNA is set to a function of temperature as discussed further below.

In Equation S1, ϕ_i is the volume fraction of species (tau, RNA, Na^+ , Cl^- , H_2O). ϕ_i was computed by $\phi_i = c_i \times N_i \times \frac{1}{c_w}$ where c_i is the molar concentration and c_w the molar concentration of pure water computed from water volume molarity: $c_w = 55.56 \text{ mol/L}$. In experiments, c_{tau} and c_{RNA} were designed to reach a 1:1 charge ratio, therefore, we have $N_{\text{RNA}} \times c_{\text{RNA}} = 11 \times c_{\text{tau}} = 11 \times [\text{tau}]$. In addition to NaCl, there is 20 mM ammonium acetate in the buffer. The total monovalent salt concentration is $c_{\text{salt}} = c_{\text{NaCl}} + 20 \text{ mM} = [\text{NaCl}] + 20 \text{ mM}$. Therefore, ϕ_i were calculated from experimental $[\text{tau}]$ and $[\text{NaCl}]$ as,

$$\begin{aligned}
\phi_{\text{tau}} &= [\text{tau}] \times 207 \times \frac{1}{c_w} \\
\phi_{\text{RNA}} &= [\text{tau}] \times 11 \times \frac{1}{c_w} \\
\phi_{\text{salt}} &= ([\text{NaCl}] + 20 \text{ mM}) \times \frac{1}{c_w} \\
\phi_{\text{polymer}} &= \phi_{\text{tau}} + \phi_{\text{RNA}} = [\text{tau}] \times 218 \times \frac{1}{c_w} \\
\phi_{\text{water}} &= 1 - \phi_{\text{polymer}} - \phi_{\text{salt}}
\end{aligned} \tag{S2}$$

α is the strength of the electrostatic interactions defined as

$$\alpha = \frac{2}{3} \sqrt{\frac{\pi}{l_w^3}} \left(\frac{e^2}{4\pi\epsilon_r\epsilon_0 k_B T} \right)^{3/2} \tag{S3}$$

where l_w is the length of a lattice, computed from c_w , $l_w = \sqrt[3]{\frac{1 \times 10^{-3} \text{ m}^3}{c_w N_A}}$, $\epsilon_r\epsilon_0$ the water permittivity, $\epsilon_r\epsilon_0 = 80 \times 8.85 \times 10^{-12} \text{ F/m}$, k_B the Boltzmann constant and T the absolute temperature.

χ_{ij} is the Flory-Huggins interaction parameter between species i and j, which will be defined and discussed below.

The three terms on the right-hand side of Equation S1 are respectively: 1) the ideal Flory-Huggins mixing entropy, 2) the mixing enthalpy due to Coulombic interactions based on Debye-Hückel approximation [265] and 3) the excess free energy to account for the non-Coulombic interactions, which can include contributions from water perturbation [266], cation- π interaction [202] and dipole-dipole interactions [267]. Equation S1 has been successfully applied in PDMAEMA-PAA complex coacervate [128]. In this work we refer to Equation S1 as FH-VO model, which is a minimal model for complex coacervation.

Determining phase separation temperature

A phase separation temperature, T_{cp} , was assigned to the cloud point of the sample. T_{cp} was determined by fitting normalized turbidity-temperature curves to a sigmoid function as follows

$$normalized\ turbidity = \frac{1}{1 + \exp(-k \times (T - T_{cp}))},$$

to find

$$T = T_{cp}.$$

FH-VO binodal curve computation

ϕ_i and T can be converted from/to experimental conditions as described, where tau and RNA are added at a fixed charge neutrality ratio. Therefore, ΔG_{mix} depends on four variables: total polymer volume fraction $\phi_{polymer} = \phi_p + \phi_q$, total salt volume fraction $\phi_{salt} = \phi_{s+} +$

ϕ_{s-} , temperature T and X , a matrix of $\chi_{pp}, \chi_{pq}, \chi_{ps+}, \dots, \chi_{qp}, \chi_{qq}, \dots$. A two-phase equilibrium exists where the sum of mixing free energy of two coexisting phases are lower than that of the homogeneous mixture. For simplicity, we adopt the assumption that the salt concentration in both two phases are identical [128], leaving the system a binary mixture of polymer and buffer. Binodal compositions are defined by pairs of points on the curve of ΔG_{mixing} vs. $\phi_{polymer}$ that have common tangents, corresponding to compositions of equal chemical potentials of both buffer and polymer in dense and dilute phases.

A binodal composition curve (binodal curve) was computed by finding the bi-tangent points of ΔG_{mixing} vs. $\phi_{polymer}$ at a series of ϕ_{salt} at given temperature T and given parameters. Given ϕ_{salt}, T and X , the mixing free energy is solely dependent on $\phi = \phi_{polymer}$:

$$f(\phi) = \Delta G_{mixing}(\phi_{polymer})$$

A bi-tangent pair $(\phi_1, f_1), (\phi_2, f_2)$ was calculated by solving the set of nonlinear equations [268], [269],

$$\begin{cases} \left. \frac{\partial f}{\partial \phi} \right|_{\phi=\phi_1} - \left. \frac{\partial f}{\partial \phi} \right|_{\phi=\phi_2} = 0 \\ \left(f - \phi \frac{\partial f}{\partial \phi} \right) \Big|_{\phi=\phi_1} - \left(f - \phi \frac{\partial f}{\partial \phi} \right) \Big|_{\phi=\phi_2} = 0 \end{cases}$$

which was solved by R function *nleqslv* using Newton-Ralphson algorithm at given initial guess. Finally, the $\phi_{polymer}$ and ϕ_{salt} were converted into $[\tau]$ and $[\text{NaCl}]$ as described.

Calculation of non-ionic entropy and enthalpy of coacervation

As discussed in the main text the interaction parameter is decomposed into an entropic and enthalpic contribution $\chi = \epsilon_s + \epsilon_H/T$. According to the Flory-Huggins treatment the non-combinatoric contribution to the Gibbs free energy of mixing is

$$\Delta G_{mix} = RTn_p\chi\phi_w$$

where R is the ideal gas constant, T is the temperature, n_p is the total number of moles of monomer units, and ϕ_w is the volume fraction of water. From the relation $\Delta S_{mix} = -\frac{\partial \Delta G_{mix}}{\partial T}$, the non-ideal entropy of mixing is

$$\Delta S_{mix} = -Rn_p\phi_w\epsilon_s.$$

From the relation $\Delta H_{mix} = \Delta G_{mix} + T\Delta S_{mix}$, the enthalpy of mixing arising from non-ionic interactions is

$$\Delta H_{mix} = Rn_p\phi_w\epsilon_H.$$

Values in the main text are computed using a water volume fraction of $\phi_w = 0.722$.